64 color figures from T. L. Szabo, Diagnostic Ultrasound Imaging: Inside Out, © 2014 Elsevier Inc.,

SECOND EDITION
DIAGNOSTIC ULTRASOUND IMAGING: INSIDE OUT

THOMAS L. SZABO
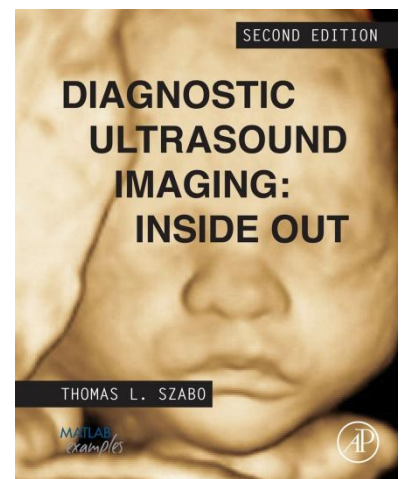
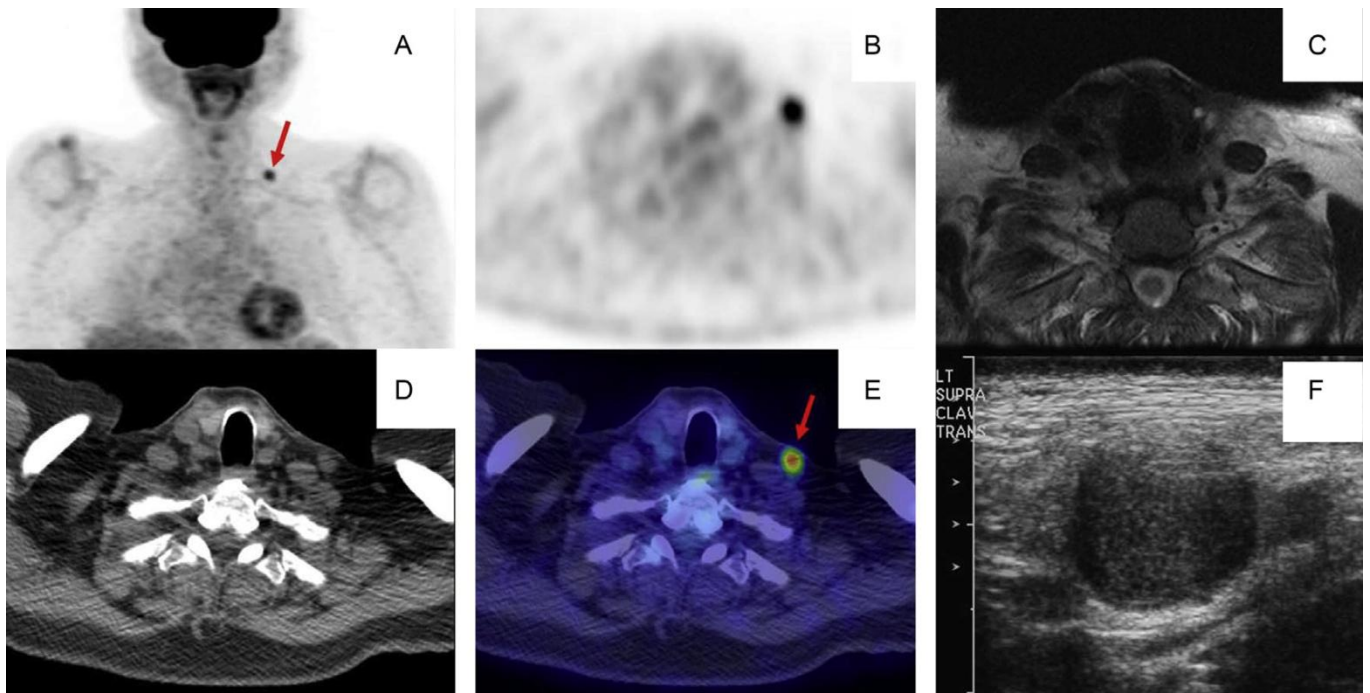|		
1.17	11.21	14.27
9.7	11.22	14.31
9.8	11.23	15.6
9.10	11.24	16.11
9.16	11.30	16.14
9.18	11.34	16.15
9.20	11.35	16.16
9.27	11.36	16.19
9.30	11.37	16.22
9.33	11.38	16.24
9.38	11.39	16.25
9.40	11.41	17.3
10.2	11.42	17.4
10.5	12.29	17.7
10.6	12.30	17.8
10.8	12.32	17.11
10.26	13.10	17.12
10.30	13.23	17.13
10.31	13.24	17.14
10.33	14.19	17.16
11.13	14.24	
11.15	14.25	

Figure 1.17. Images of different imaging modalities. (A) PET frontal; (B) PET transverse; (C) MRI transverse; (D) CT transverse; (E) PET/CT transverse fused image; and (F) ultrasound. Images of a 74-yearold male patient with nasal cavity esthesioneuroblastoma (a form of nasal cancer) who was restaged on a routine follow-up. PET identified a left supraclavicular hypermetabolic nodal metastasis (A, B, D, and E) that was not identified in the MRI (C). An ultrasound-guided biopsy of the node was positive for esthesioneuroblastoma and then surgically resected (F) Courtesy of Dr Rathan Subramaniam, 2010. *T. L. Szabo, Diagnostic Ultrasound Imaging: Inside Out, © 2014 Elsevier Inc., All rights reserved.*
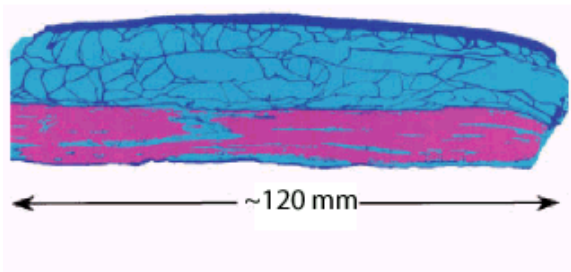
Figure 9.7 Cross-sectional tissue map of an abdominal wall with assigned acoustic properties.From Mast, Hinkelman, Orr, Sparrow, and Waag (1997), Acoustical Society of America. *T. L. Szabo, Diagnostic Ultrasound Imaging: Inside Out, © 2014 Elsevier Inc., All rights reserved.*
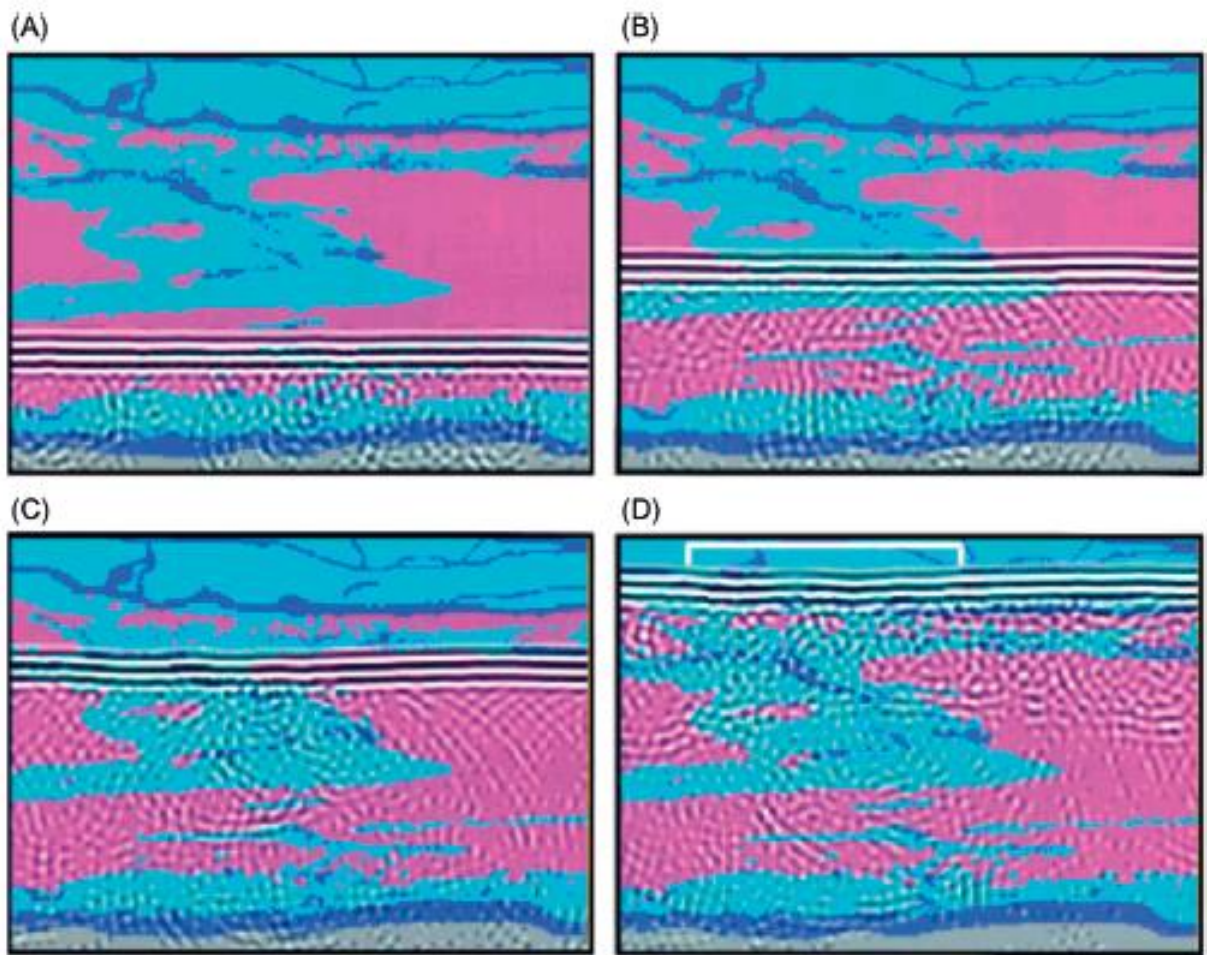
Figure 9.8. Propagation of a plane wave through a section of the abdominal wall sample depicted in Figure 9.7. (AD) Upward progression of the main wavefront through the muscle layer, including an aponeurosis comprised of fat and connective tissue, resulting in time-shift aberration across the wavefront. The area shown in each frame is 16.0 mm in height and 18.7 mm in width. The temporal interval between frames is 1.7 ms. Tissue is color coded according to the scheme of Figure 9.7, while gray background represents water. Wavefronts are shown on a bipolar logarithmic scale with a 30-dB dynamic range. The wavefront represents a 3.75-MHz tone burst with white representing maximum positive pressure and black representing maximum negative pressure. A cumulative delay of about 0.2 ms, associated with propagation through the aponeurosis, is indicated by the square bracket in panel (D). From Mast et al (1997), Acoustical Society of America. *T. L. Szabo, Diagnostic Ultrasound Imaging: Inside Out, © 2014 Elsevier Inc., All rights Reserved.*
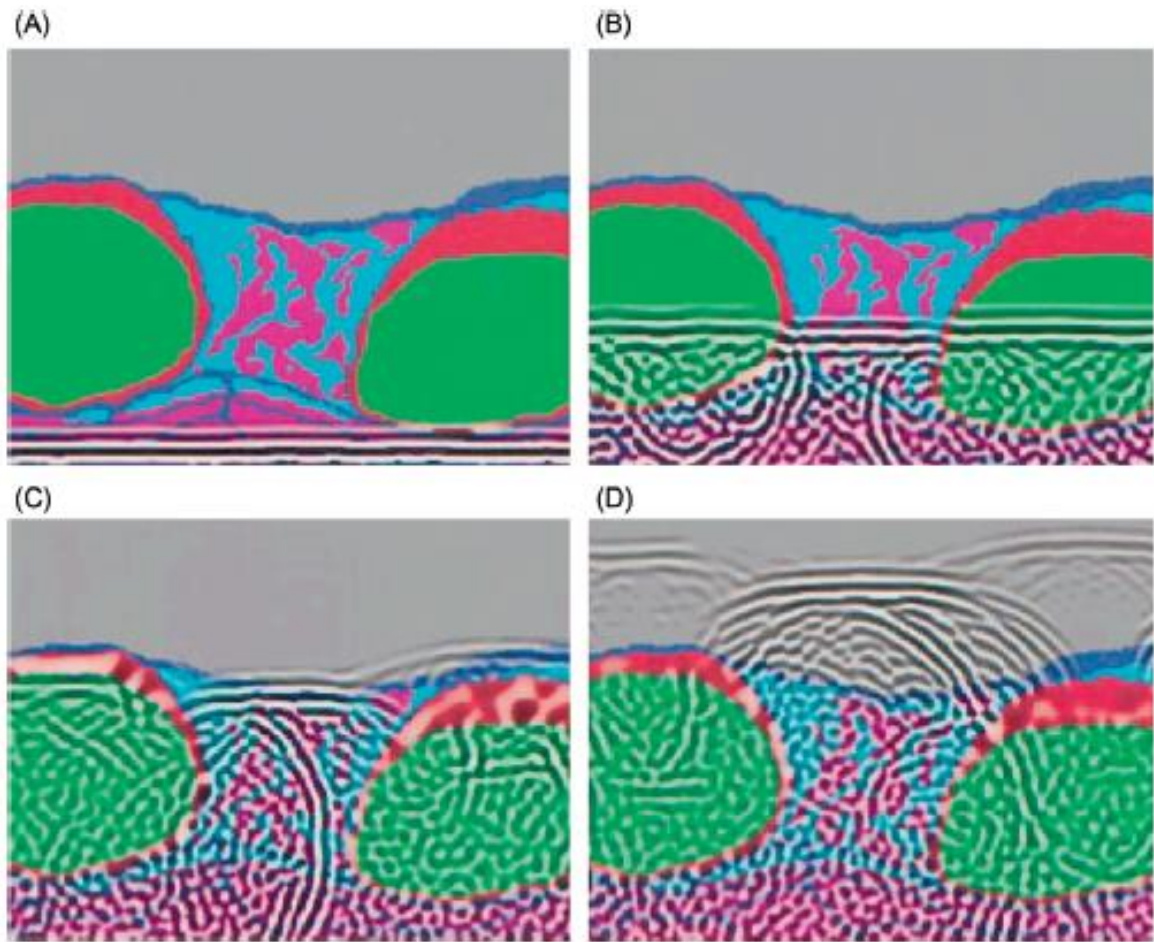
Figure 9.10. Simulation of 2.3-MHz plane wave tone burst wavefront propagating through a chest tissue map.In each map, blue denotes skin and connective tissue, cyan denotes fat, purple denotes muscle, orange denotes bone, and green denotes cartilage. Blood vessels appear as small water-filled (white) regions. Logarithmically compressed wavefronts are shown on a b ipolar scale with black representing minimum pressure, white representing maximum pressure, and a dynamic range of 57 dB. Each panel shows an area that spans 28.27 mm horizontally and 21.20 mm vertically. From Mast et al. (1999), Acoustical Society of America. *T. L. Szabo, Diagnostic Ultrasound Imaging: Inside Out, © 2014 Elsevier Inc., All rights reserved. .*
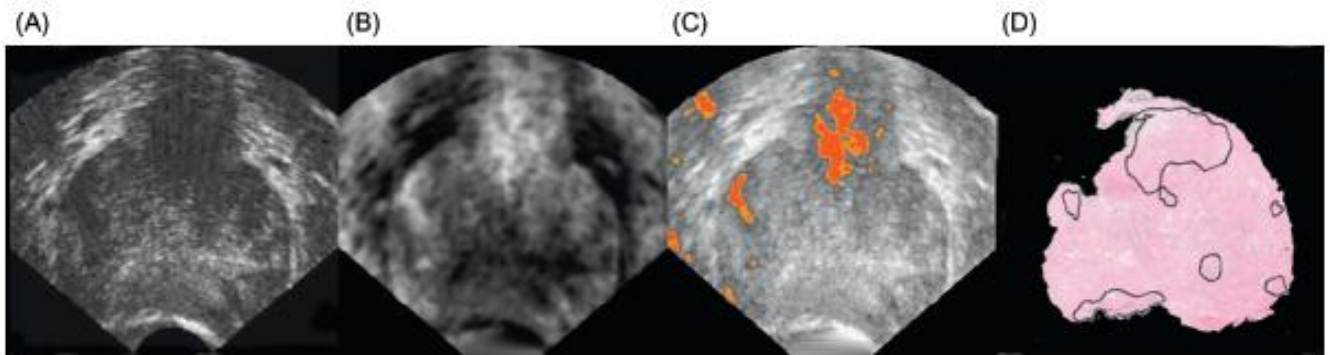
Figure 9.16 Images of the central plane of a prostate gland having an ultrasonically-occult anterior tumor as viewed from the Apex of the prostate. Computer-generated envelope-detected B-mode image; (B) gray-scale cancer-likelihood image (white5maximum likelihood); (C) color-encoded overlay on a midband parameter image depicting the two highest levels of likelihood in red and orange (red areas appear black in the gray-scale image reproduced in the print version of the book, and orange areas are gray (mostly in areas immediately surrounding the red)); (D) corresponding histological section that shows a 12-mm tumor protruding through the anterior surface and several smaller circular intracapsular foci of cancer and neoplasia, as manually demarcated in ink by the pathologist. From Feleppa et al. (2001), reprinted with permission of Dynamedia, Inc. *T. L. Szabo, Diagnostic Ultrasound Imaging: Inside Out, © 2014 Elsevier Inc., All rights reserved.*
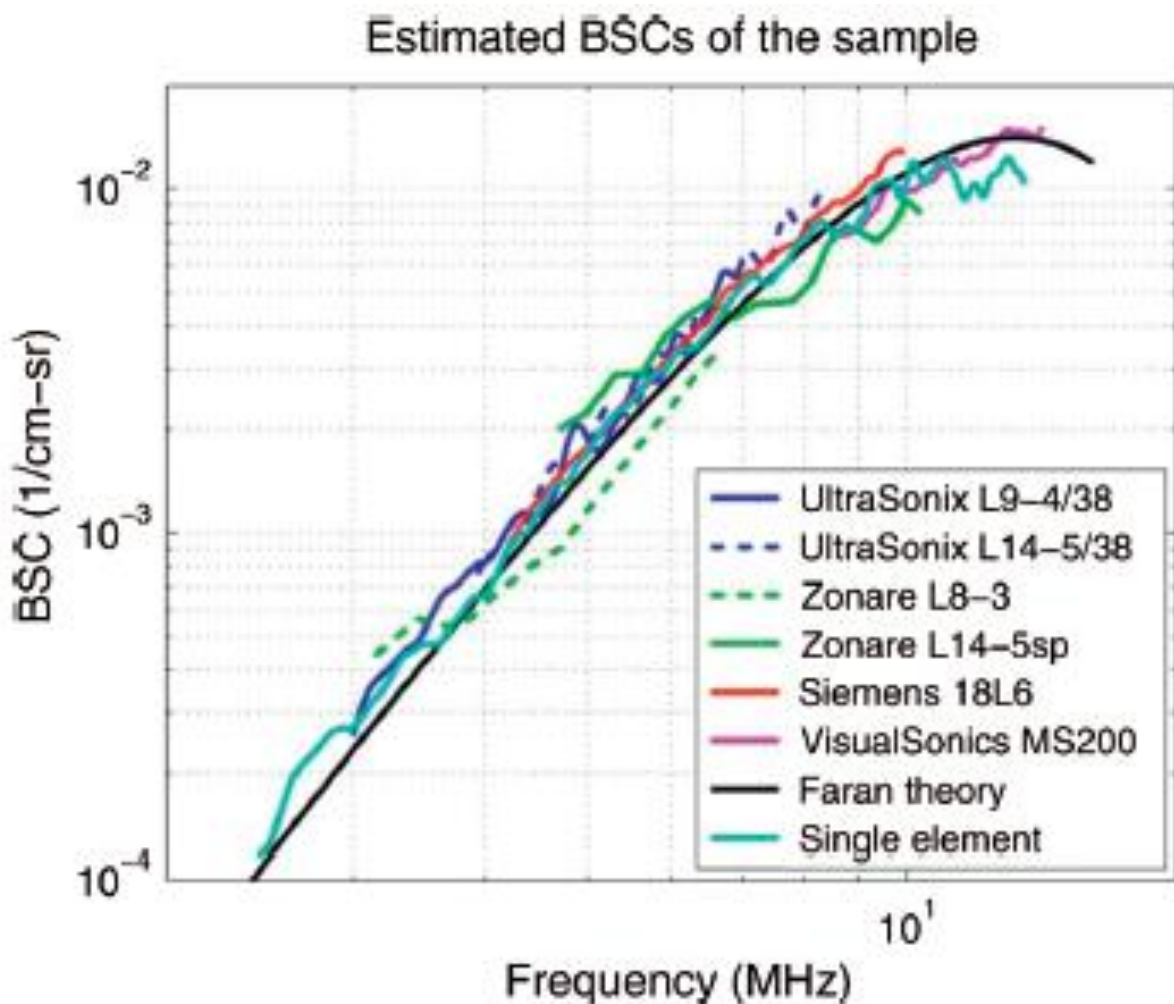
Figure 9.18 Backscatter coefficients vs frequency estimates using each of the clinical ultrasound systems. Each data line represents a different transducer system combination. Results are presented for two transducers for both the UltraSonix and the Zonare scanners. Also shown are lab measurements employing single-element transducers. The solid black curve is computed using the theory of Faran.From Nam et al. (2012), Acoustical Society of America. *T. L. Szabo, Diagnostic Ultrasound Imaging: Inside Out, © 2014 Elsevier Inc., All rights reserved.*
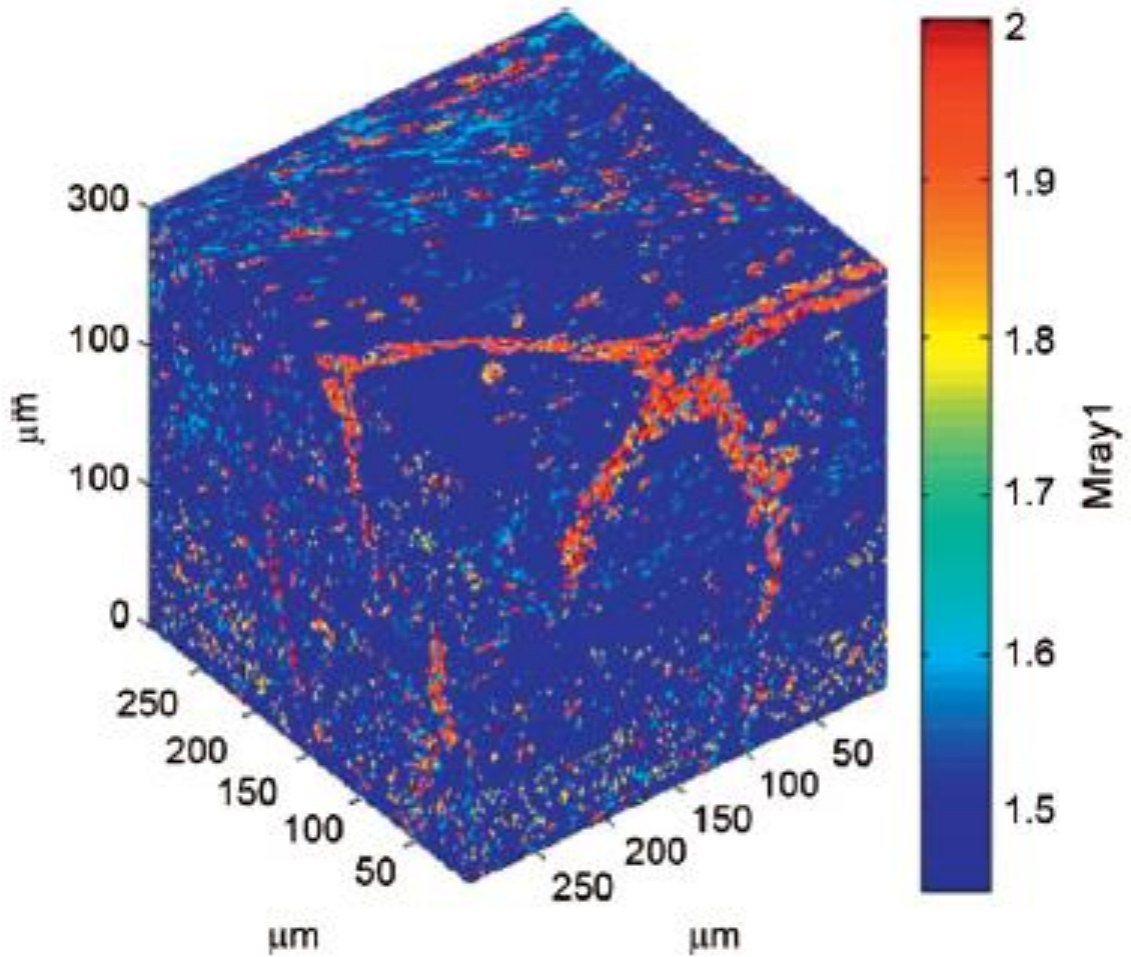
Figure 9.20 Rendering of a Three-dimensional Impedance Map (3DZM) of a Human Fibroadenoma. From Dapore et al. (2011), IEEE. *T. L. Szabo, Diagnostic Ultrasound Imaging: Inside Out, © 2014 Elsevier Inc., All rights Reserved.*
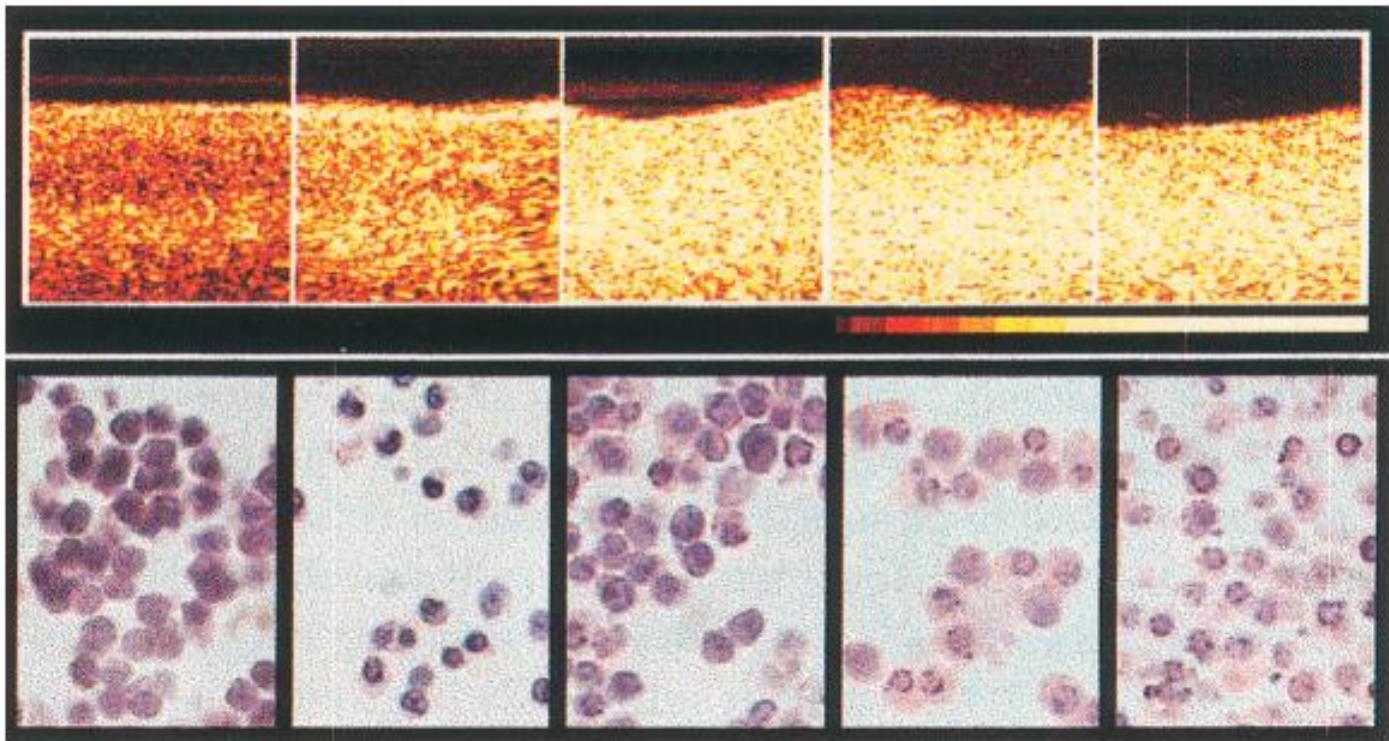
Figure 9.27 Ultrasound imaging of apoptosis and correlative histology. Sequential panels show cells at 0, 6, 12, 24, and 48 hours after treatment with a toxic drug. Each panel is approximately 5 mm wide.(Top row) 40-MHz ultrasound backscatter images of cells. (Bottom row) optical microscopic images of stained cells; field of view is approximately 50 μm. From Czarnota et al. (1999, 2001), reprinted with permission from Nature Publishing Group. *T. L. Szabo, Diagnostic Ultrasound Imaging: Inside Out, © 2014 Elsevier Inc., All rights reserved.*
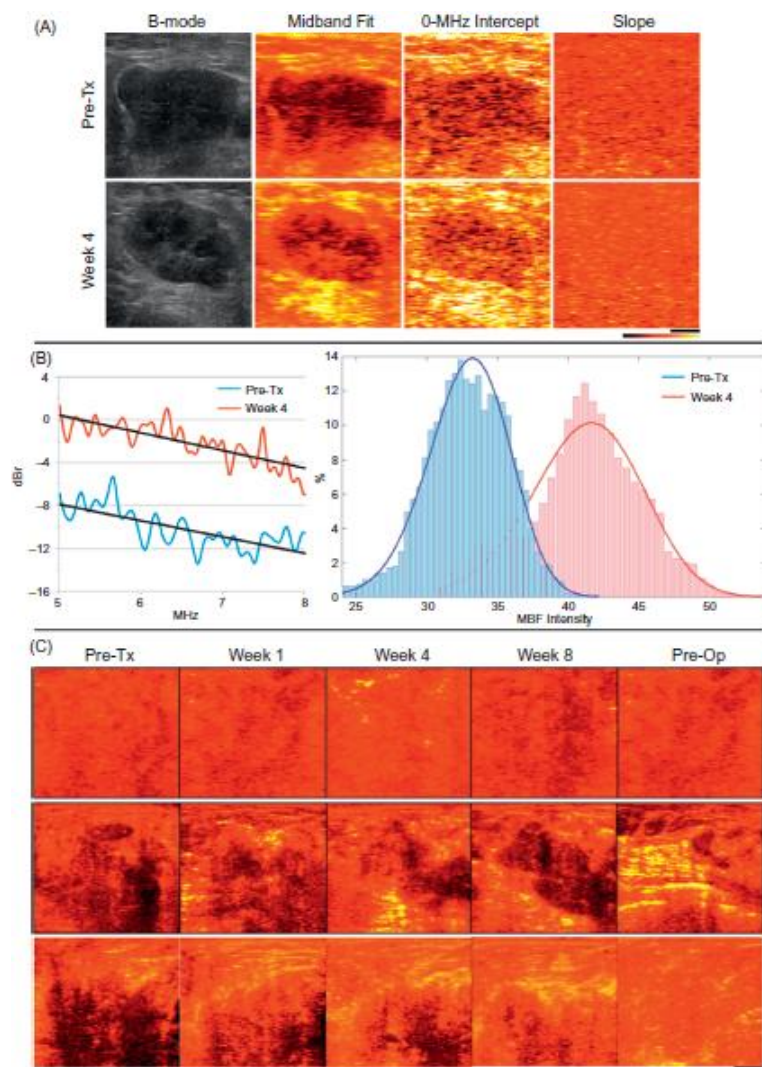
Figure 9.30. Quantitative ultrasound for evaluation of tumor cell-death response.(A) Representative data from a large breast tumor before starting the neo-adjuvant chemotherapy (first row), and after 4 weeks of treatment (second row). The columns from left to right demonstrate ultrasound B-mode, parametric images of midband fit, 0-MHz intercept, and spectral slope, respectively. The scale bar is B1 cm, and the color map represents a scale encompassing B50 dBr for midband fit (MBF) and 0-MHz intercept, and B15 dBr/MHz for the spectral slope. (B) Normalized power spectra (left) and generalized gamma fits on the histograms of the MBF intensity (right) for the tumor region (lower power spectrum line and left-hand histogram correspond to week 4 post-treatment). (C) Representative parametric images of 0-MHz intercept from a non-responding patient (first row), as well as from two patients who responded to the treatment (second and third rows). The data for each patient were acquired from the same nominal regions, prior to treatment as well as at weeks 1, 4, and 8 during treatment, and preoperatively from left to right, respectively. The scale bar represents B1 cm. The color bar represents a scale encompassing B80 dBr. From Sadeghi-Naini et al. (2013b). *T. L. Szabo, Diagnostic Ultrasound Imaging: Inside Out, © 2014 Elsevier Inc., All rights reserved.*
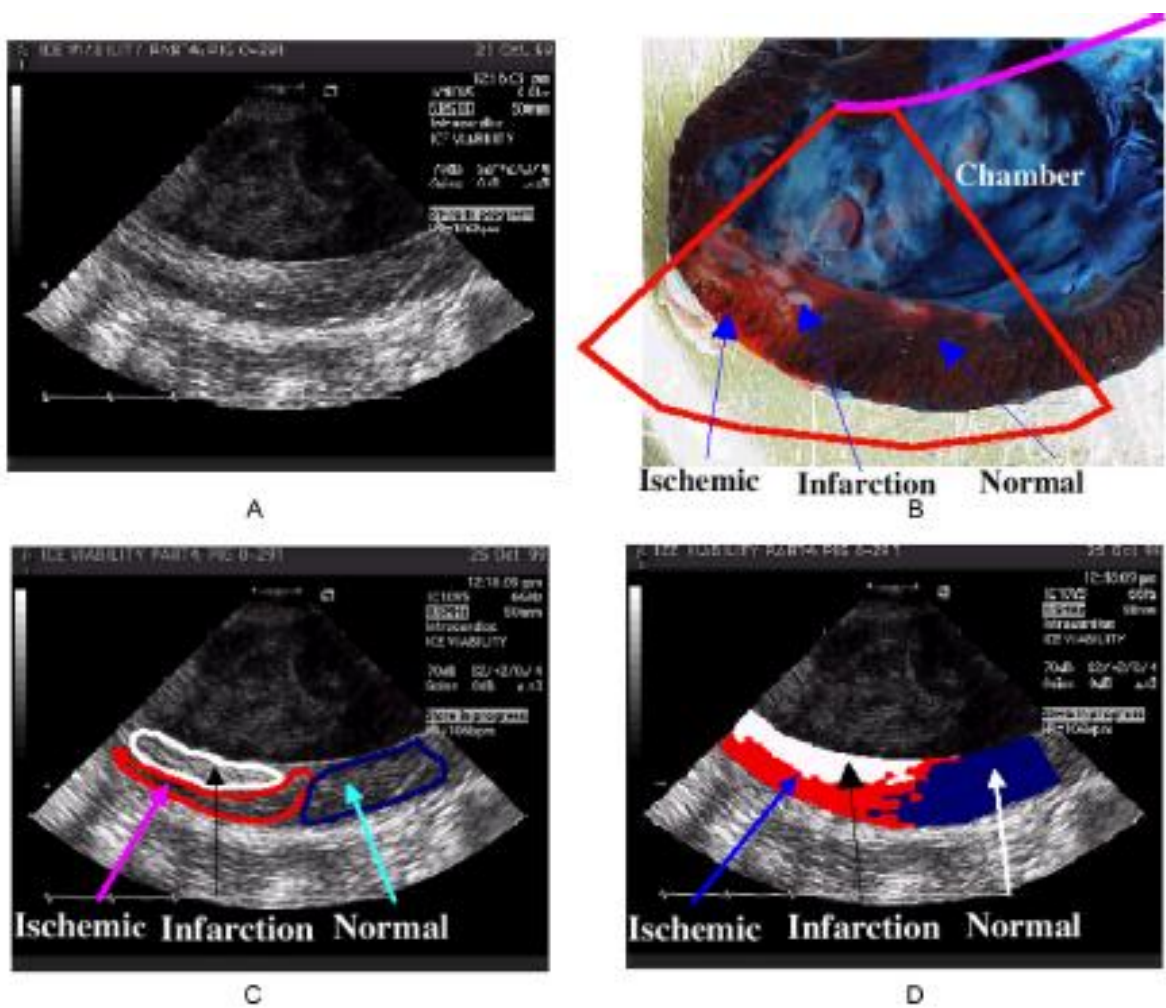
Figure 9.33. Segmentation of the ischemic myocardium (A) Original ultrasound image; (B) the pathology gross image of the heart; (C) three regions predicted by a cardiologist; (D) the segmented classification results. Reprinted with permission from Hao et al. (2000), IEEE. *T. L. Szabo, Diagnostic Ultrasound Imaging: Inside Out, © 2014 Elsevier Inc., All rights reserve*d.
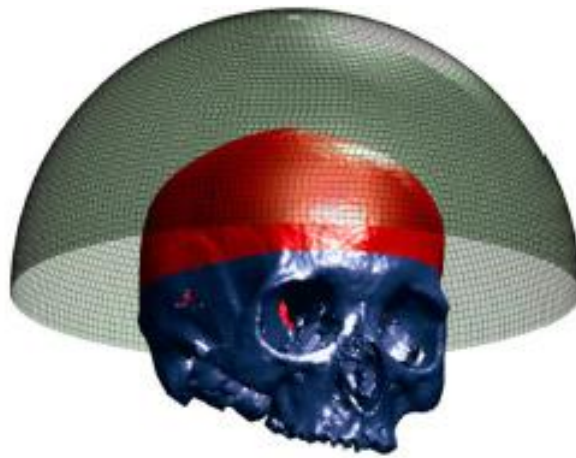
Figure 9.38. Simulated adaptive transducer array with 8907 elements positioned over segmented skull.Region of skull surface accessible by array highlighted From Pajek and Hynynen (2012b), Acoustical Society of America. *T. L. Szabo, Diagnostic Ultrasound Imaging: Inside Out, © 2014 Elsevier Inc., All rights reserved.*
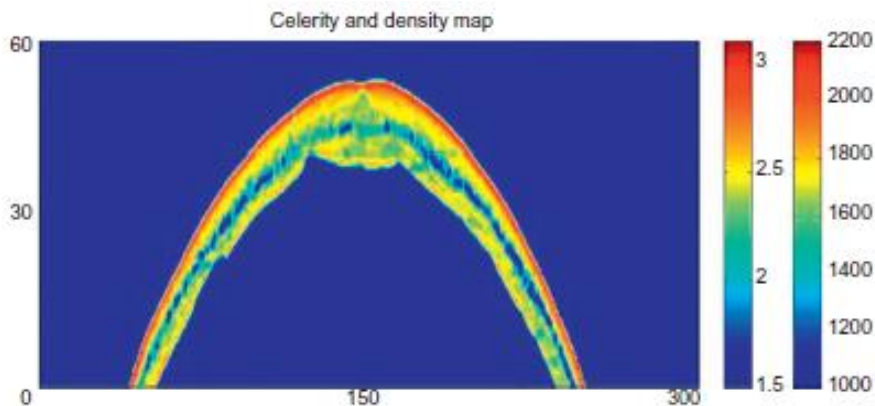

Figure 9.40 . Example of one slice in speed of sound and density map derived from skull microstructure in a CT scan. First color bar indicates speed of sound in mm/μs, second color bar density in kg/m3. The axes are in mm. From Marquet et al. (2009). r IOP Publishing. Reproduced by permission of IOP Publishing. All rights reserved. *T. L. Szabo, Diagnostic Ultrasound Imaging: Inside Out, © 2014 Elsevier Inc., All rights reserved.*
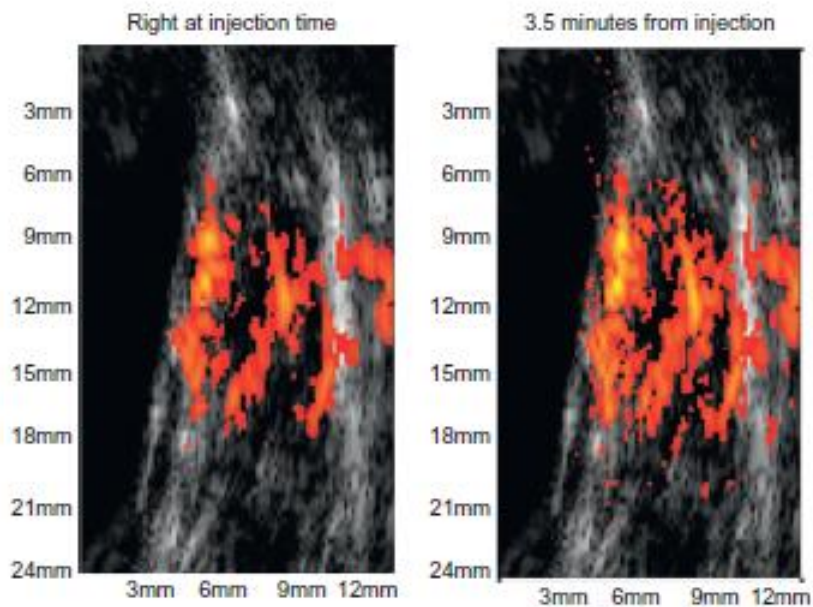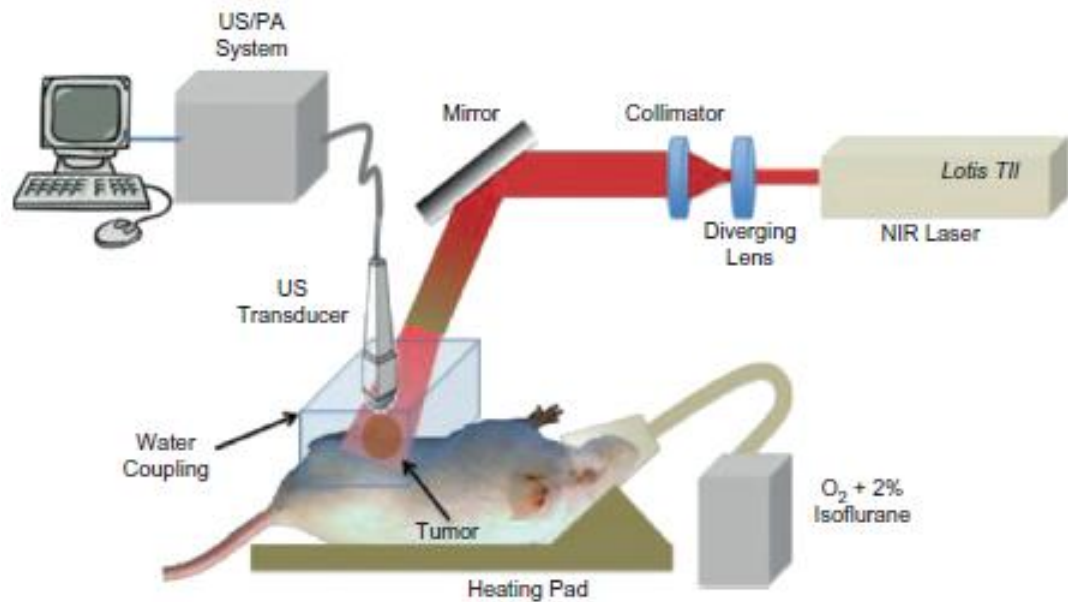
Figure 10.2. Photoacoustic mouse experiment setup. From Alqasemi et al. (2012), IEEE. *T. L. Szabo, Diagnostic Ultrasound Imaging: Inside Out,* *© 2014 Elsevier Inc., All rights re*served.
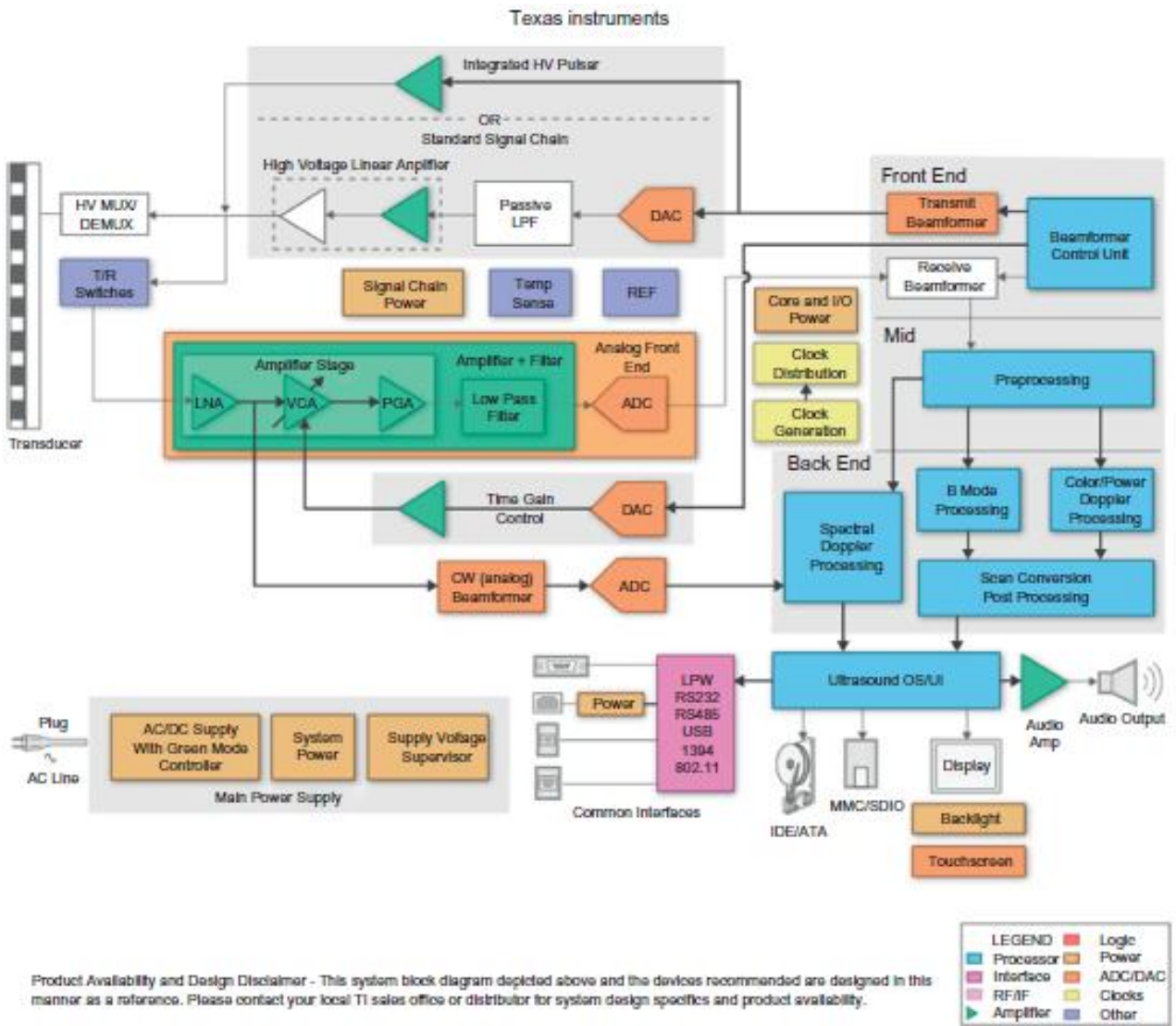
Figure 10.5. Block diagram of diagnostic ultrasound imaging system showing modular chips. ADC, analog-to-digital converter; DAC, digital-to analog converter; OS, operating system. Courtesy of Texas Instruments. *T. L. Szabo, Diagnostic Ultrasound Imaging: Inside Out, © 2014 Elsevier Inc., All rights reserved*
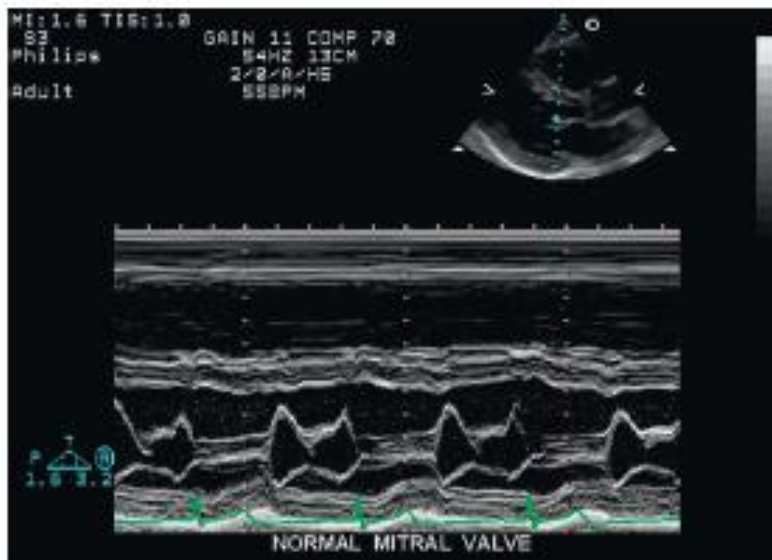
Figure 10.6. Duplex M-mode image. The insert (above right of the sector image) shows the orientation of the M-mode. Courtesy of Philips Healthcare.
T. L. Szabo, Diagnostic Ultrasound Imaging: Inside Out, © 2014 Elsevier Inc., All rights reserved
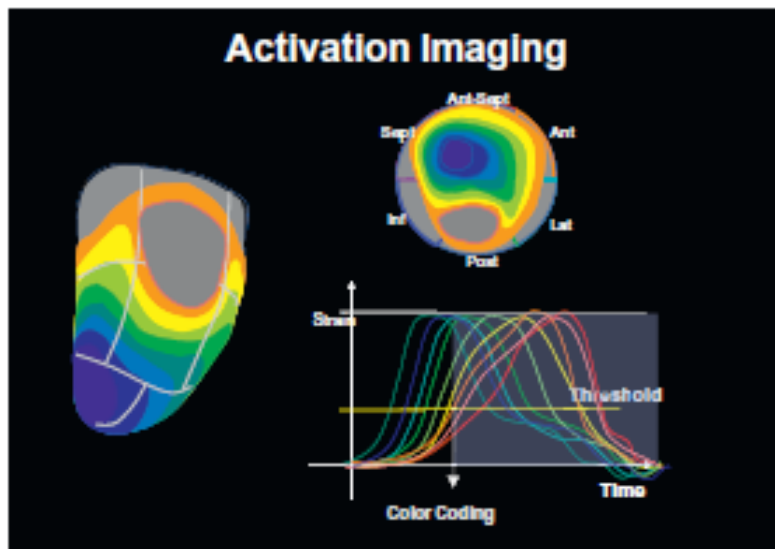

Figure 10.26. Visualization of mechanical activation of the myocardium. Color coded visualization of mechanical activation of left ventricle. Top polar view from base. Graphs indicate strain curves vs time for different segments along with threshold color mapping. Courtesy of Toshiba America Medical Systems.
T. L. Szabo, Diagnostic Ultrasound Imaging: Inside Out, © 2014 Elsevier Inc., All rights reserved

Figure 10.8. Linear arrays with steering. (A) Parallelogram-style color flow image from a linear array with steering; (B) trapezoidal form of a linear array with sector steering on either side of a straight rectangular imaging segment (described as a contiguous imaging format in Chapter 1). Courtesy of Philips Healthcare. *T. L. Szabo, Diagnostic Ultrasound Imaging: Inside Out, © 2014 Elsevier Inc., All rights reserved.*
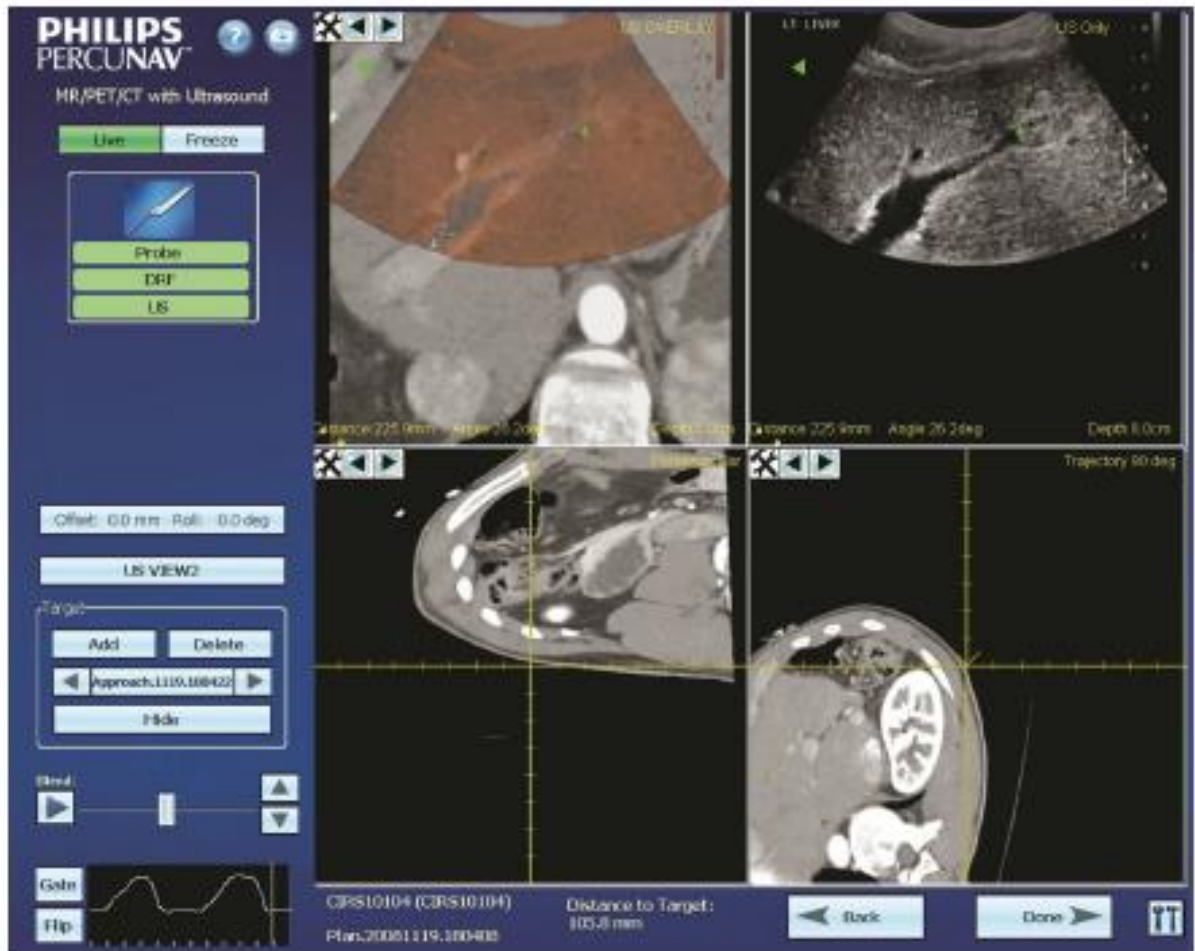
Figure 10.30. Complementary imaging. Illustration of co-registered complementary imaging of ultrasound overlaid on a static 3D CT volume (upper left) and real-time 3D ultrasound on the upper right; orthogonal CT views in panels of the lower half. Courtesy of Philips Healthcare.*T. L. Szabo, Diagnostic Ultrasound Imaging: Inside Out, © 2014 Elsevier Inc., All rights reserved.*
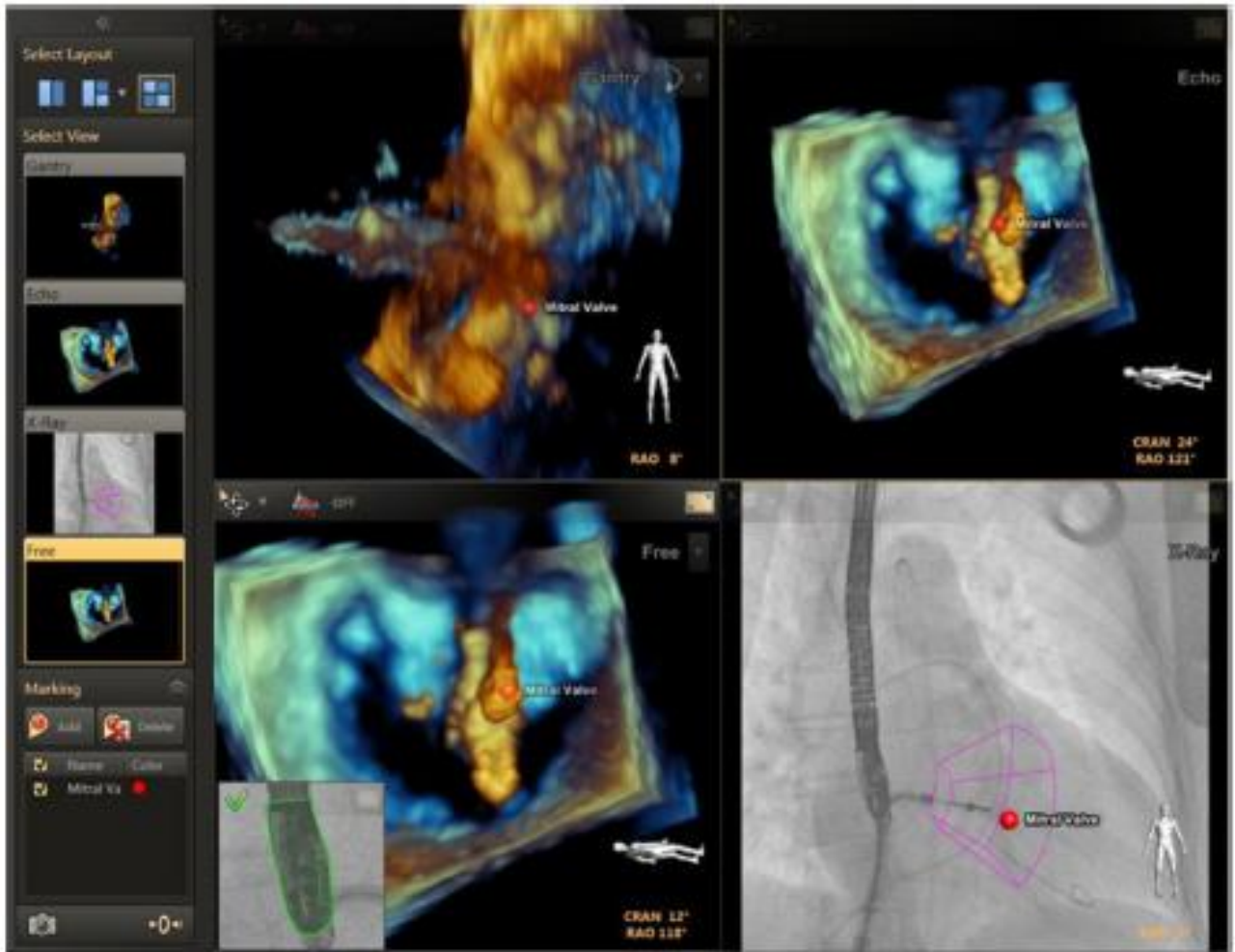
Figure 10.31. Live multimode imaging. The position of the TEE probe is tracked in real time, as shown in the fluoroscopy image and ultrasound scan volume outline (lower right panel). 3D ultrasound images compensated for movement. (Procedure shown (Mitraclip) is not FDA-approved.) Courtesy of Philips Healthcare. *T. L. Szabo, Diagnostic Ultrasound Imaging: Inside Out, © 2014 Elsevier Inc., All rights reserved.*
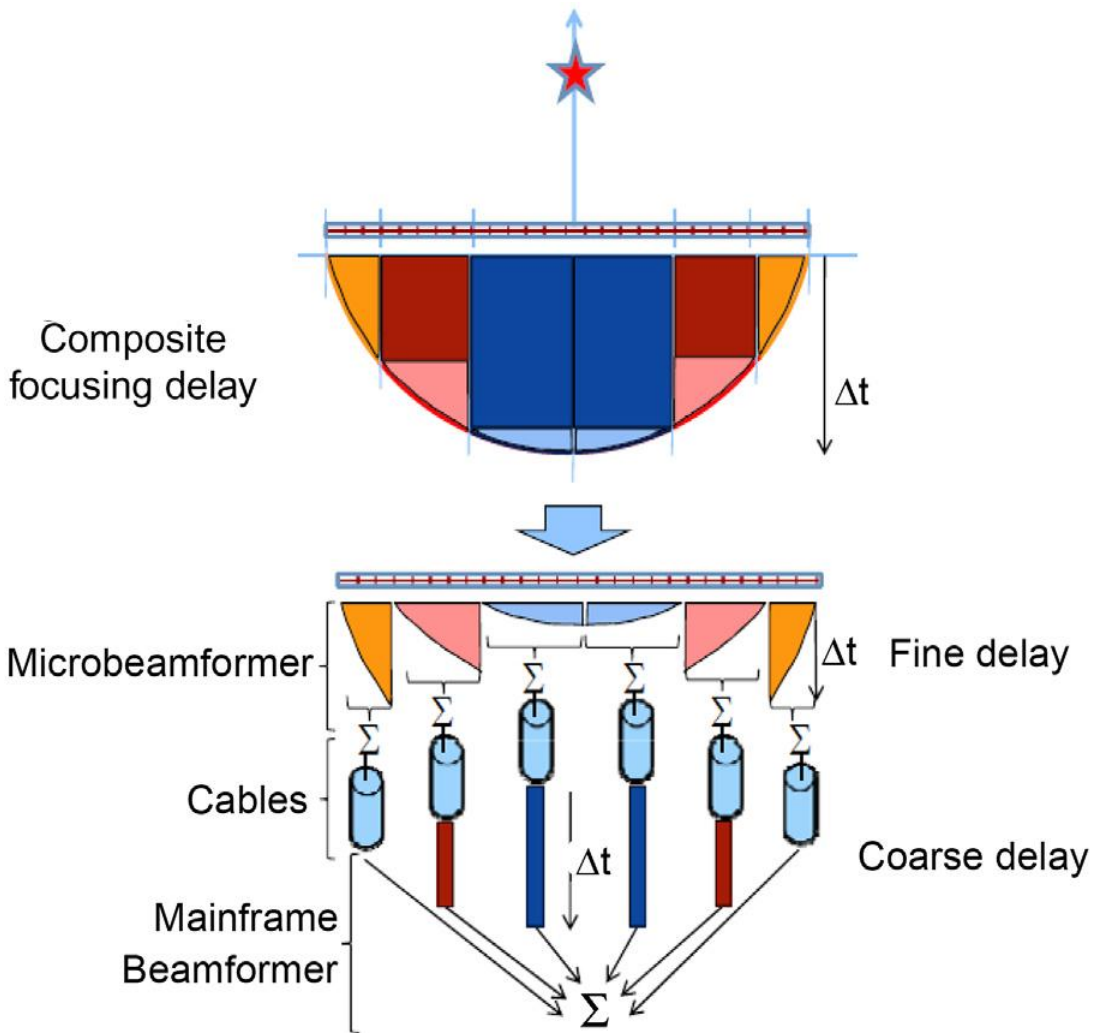
Figure 10.33. Partitioning of focusing delays for a 2D array using the microbeamformer concept.Groups of elements with fine delays are organized into sub-beamformers whose elements are initially summed and routed by cable to the main beamformer, where coarse time delays are added to achieve final focusing delays needed. From Freeman (2011a), courtesy of Philips Healthcare. *T. L. Szabo, Diagnostic Ultrasound Imaging: Inside Out, © 2014 Elsevier Inc., All rights reserved.*.
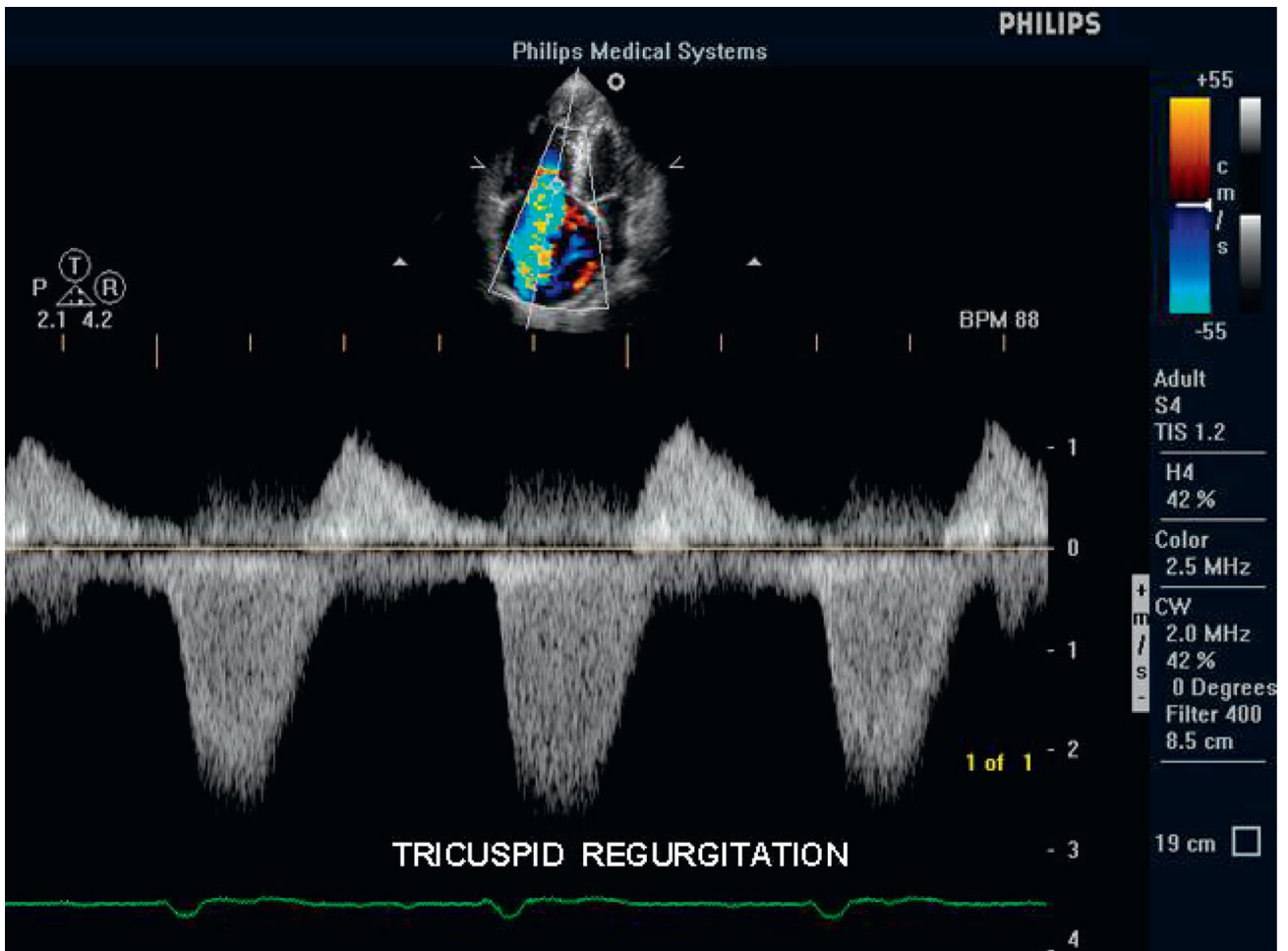
Figure 11.13. Duplex imaging mode of tricuspid regurgitation. CW Doppler velocity display with a color flow image insert (above) with direction of CW line. Courtesy of Philips Healthcare. *T. L. Szabo, Diagnostic Ultrasound Imaging: Inside Out, © 2014 Elsevier Inc., All rights reserved.*
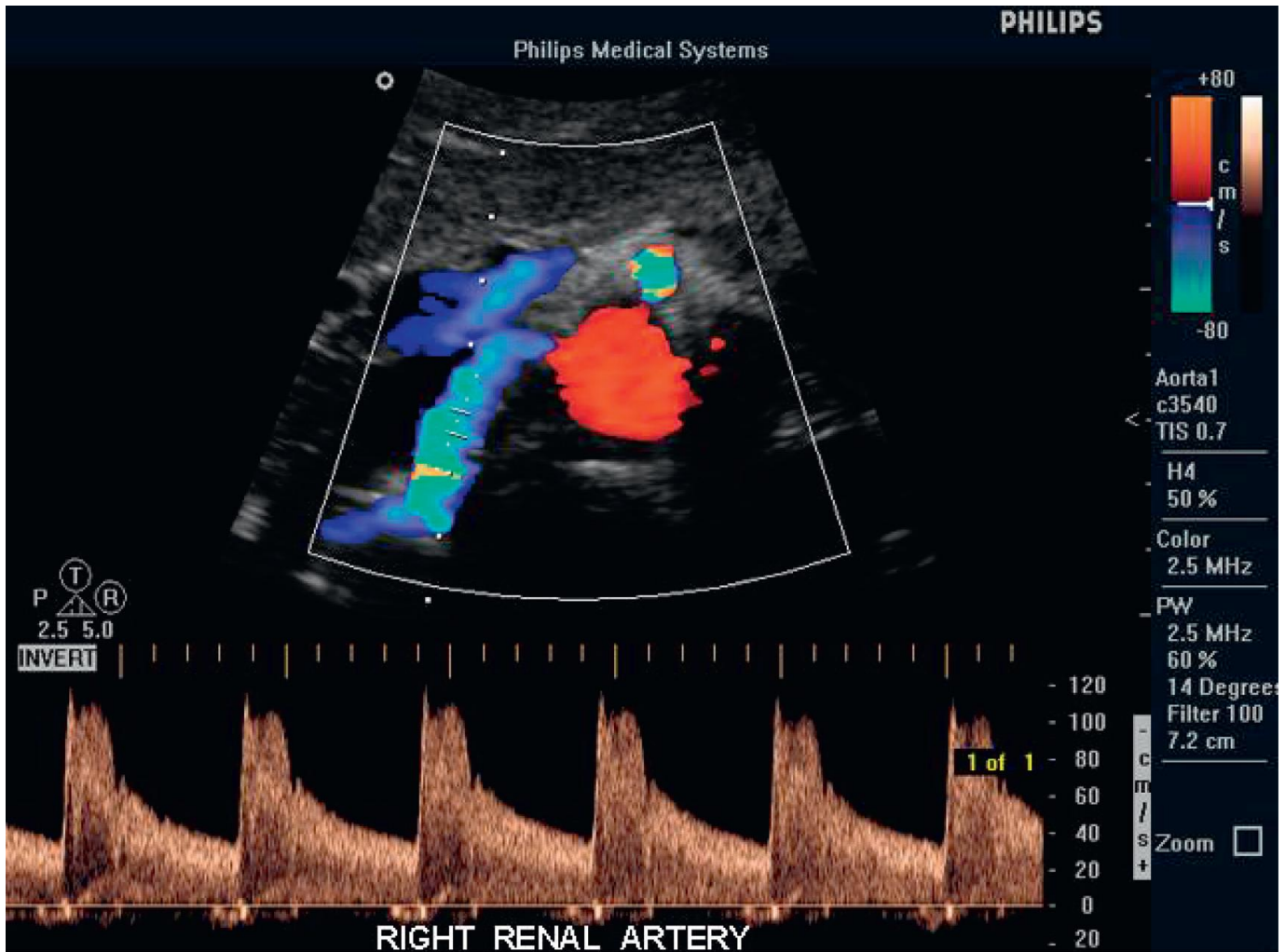
Figure 11.15. Duplex imaging mode of a right renal artery. PW Doppler velocity display, with a color flow image insert (above) with direction of PW line and Doppler gate position. Courtesy of Philips Healthcare. *T. L. Szabo, Diagnostic Ultrasound Imaging: Inside Out, © 2014 Elsevier Inc., All rights reserved.*
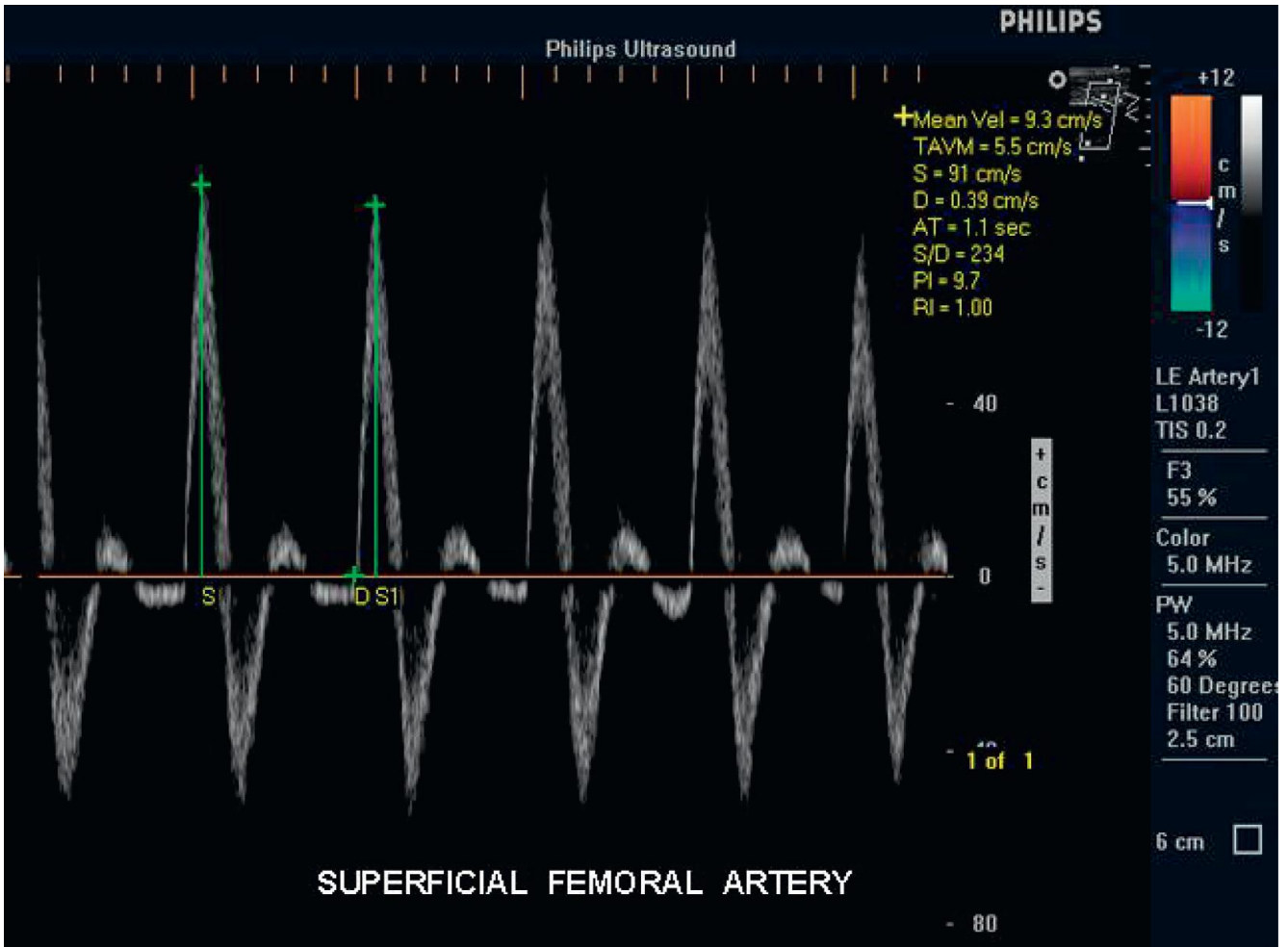
Figure 11.21. Duplex-pulsed Doppler display for a superficial femoral artery with calculations displayed and a small image in the upper-right corner. Courtesy of Philips Healthcare. *T. L. Szabo, Diagnostic Ultrasound Imaging: Inside Out, © 2014 Elsevier Inc., All rights reserved.*
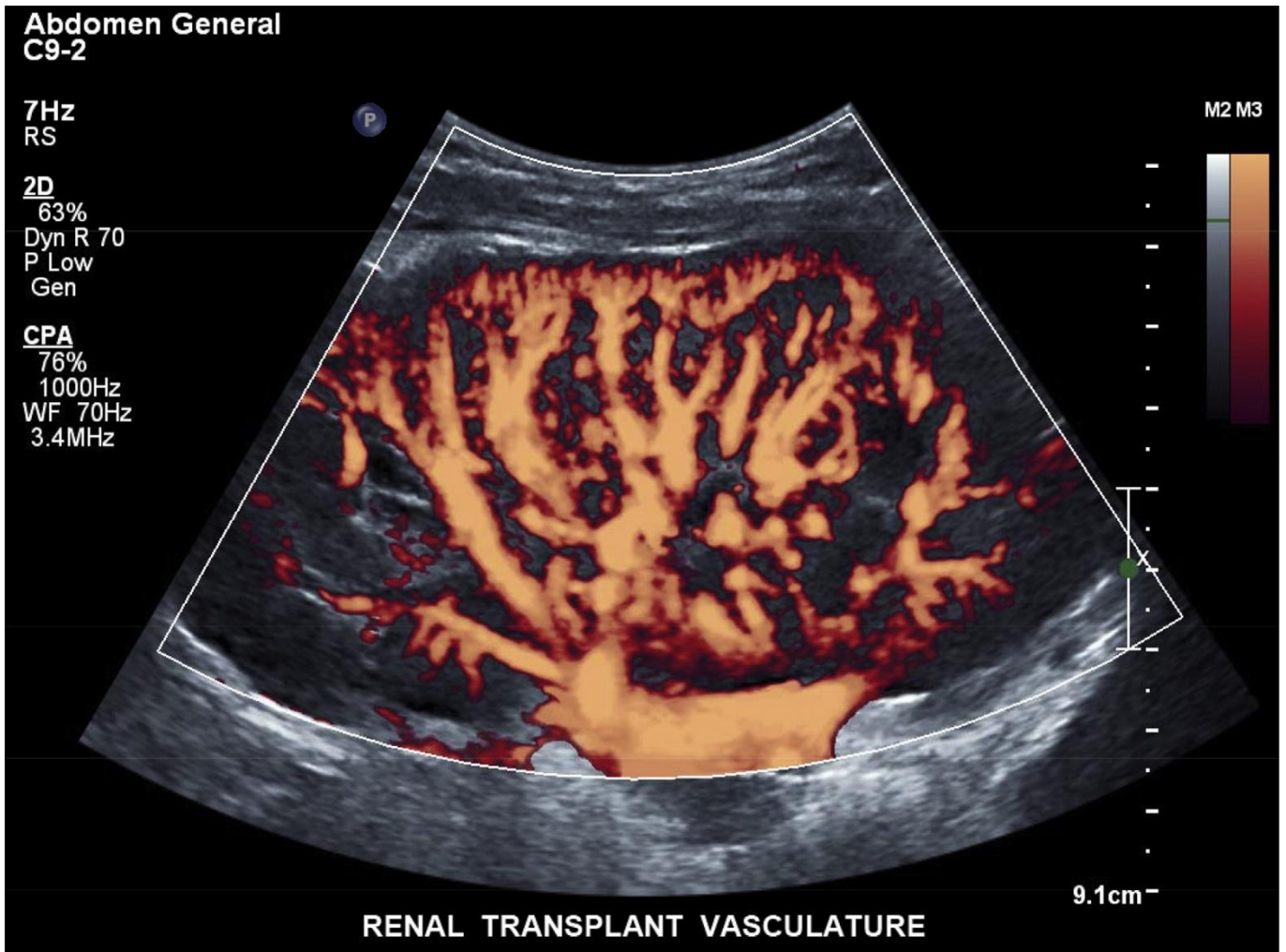
Figure 11.22. Power Doppler image of the arterial tree in a renal transplant. image taken on an EPIQ7 Philips system. Courtesy of Philips Healthcare. *T. L. Szabo, Diagnostic Ultrasound Imaging: Inside Out, © 2014 Elsevier Inc., All rights reserved.*.
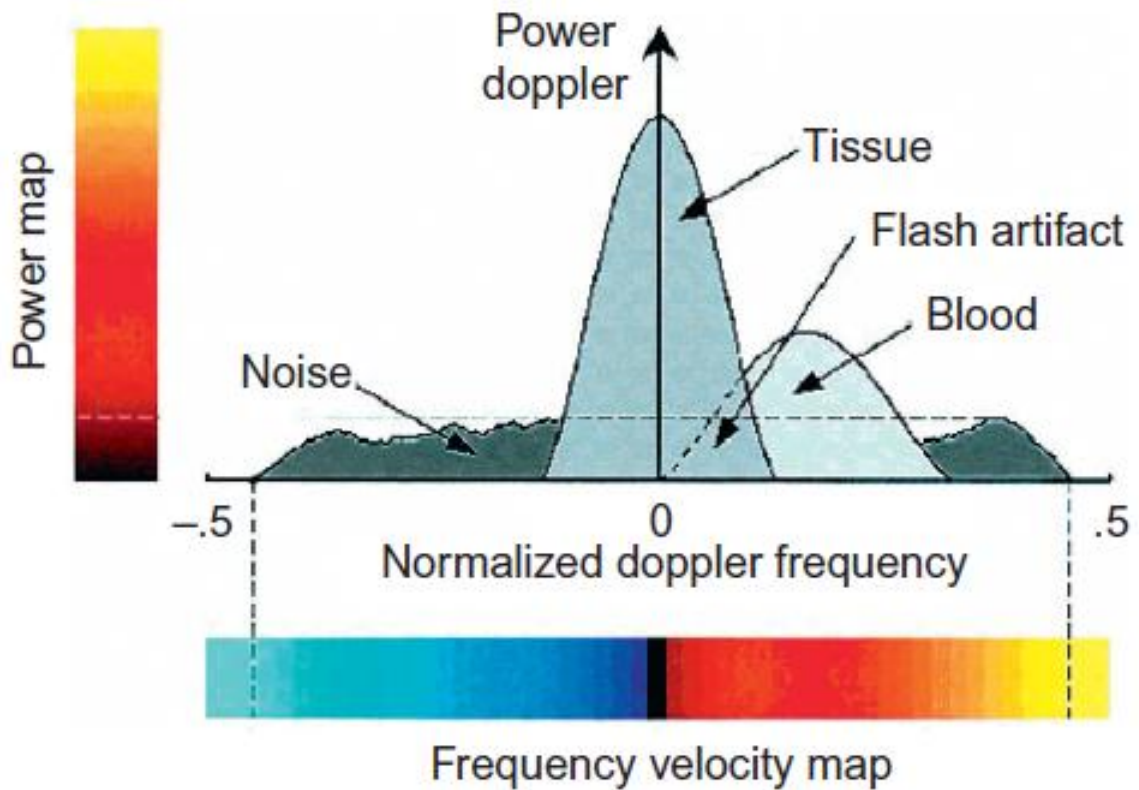
Figure 11.23. Power Doppler, a mapping of power to a continuous color range, is compared to color flow imaging.The direction and Doppler velocity are encoded as a dual display in which colors represent velocities in terms of the Doppler spectrum and also the direction of flow to and from the transducer. From Frinking et al. (2000); reprinted with permission from the World Federation of Ultrasound in Medicine and Biology. *T. L. Szabo, Diagnostic Ultrasound Imaging: Inside Out, © 2014 Elsevier Inc., All rights reserved.*
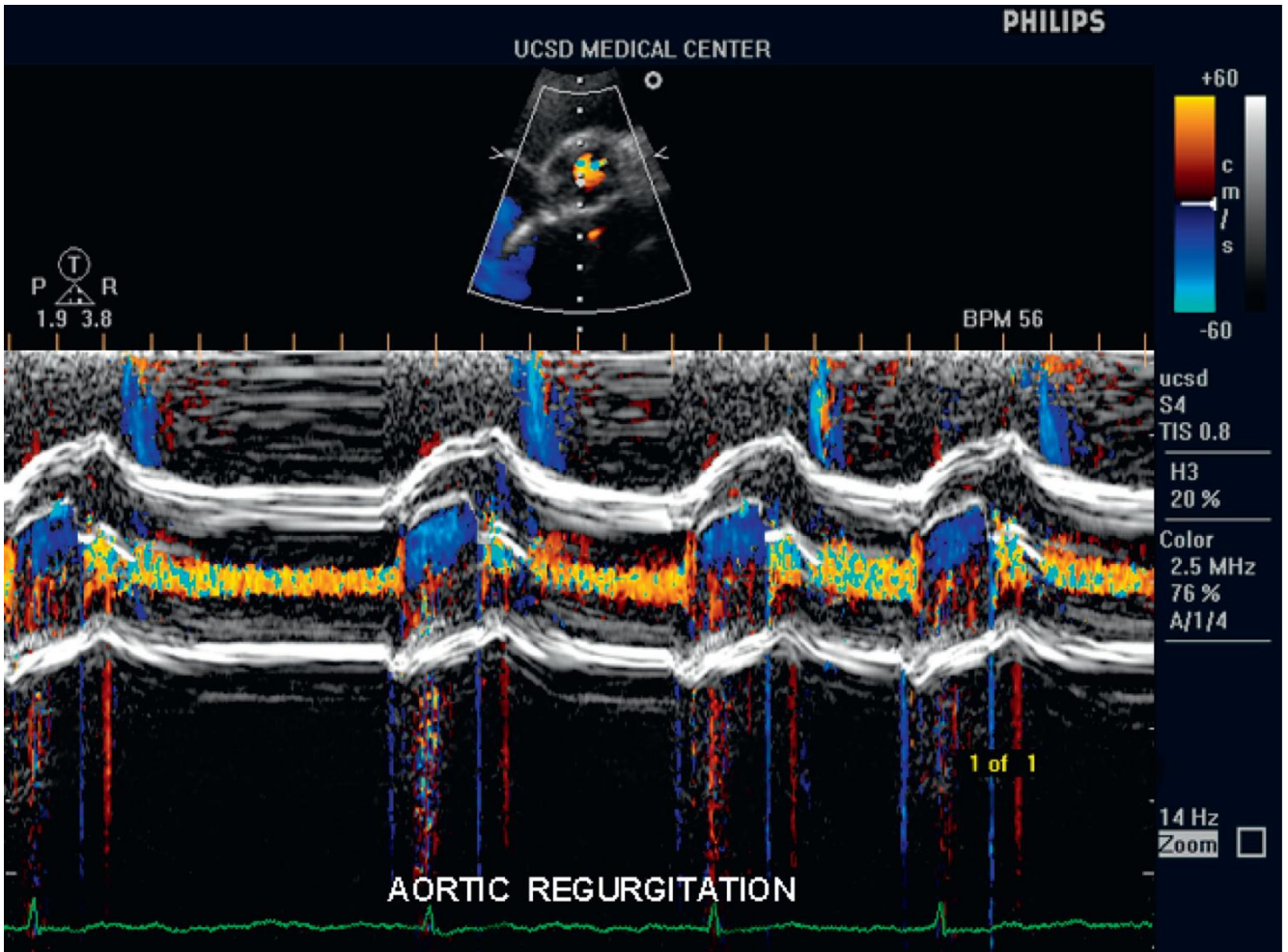
Figure 11.24. Color M-mode depiction of a leaky tricuspid valve. Courtesy of Philips Healthcare. *T. L. Szabo, Diagnostic Ultrasound Imaging: Inside Out, © 2014 Elsevier Inc., All rights reserved.* .
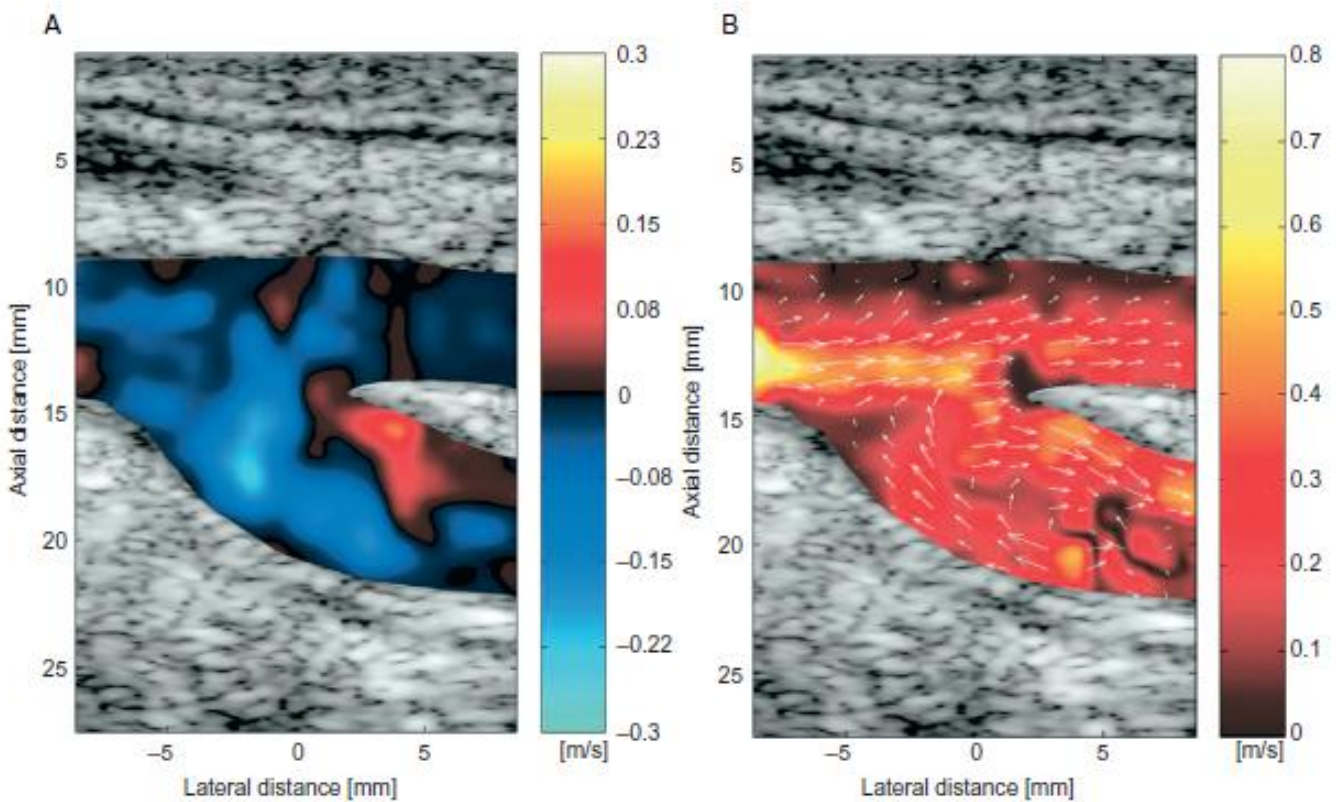
Figure 11.30. Two images depicting flow in the bifurcation of the carotid artery shortly after the peak systole.(A) The one-dimensional axial flow (towards or away from the transducer) velocity. Note, this is somewhat like color flow imaging but here flow at 90 is shown, a view impossible to obtain by conventional CFI techniques. (B) Vector flow image of the same flow at the same time instance produced by the transverse oscillation method. From Udesen, Nielsen, Nielsen, and Jensen (2007); reprinted with permission from the World Federation of Ultrasound in Medicine and Biology. *T. L. Szabo, Diagnostic Ultrasound Imaging: Inside Out, © 2014 Elsevier Inc., All rights reserved.* .
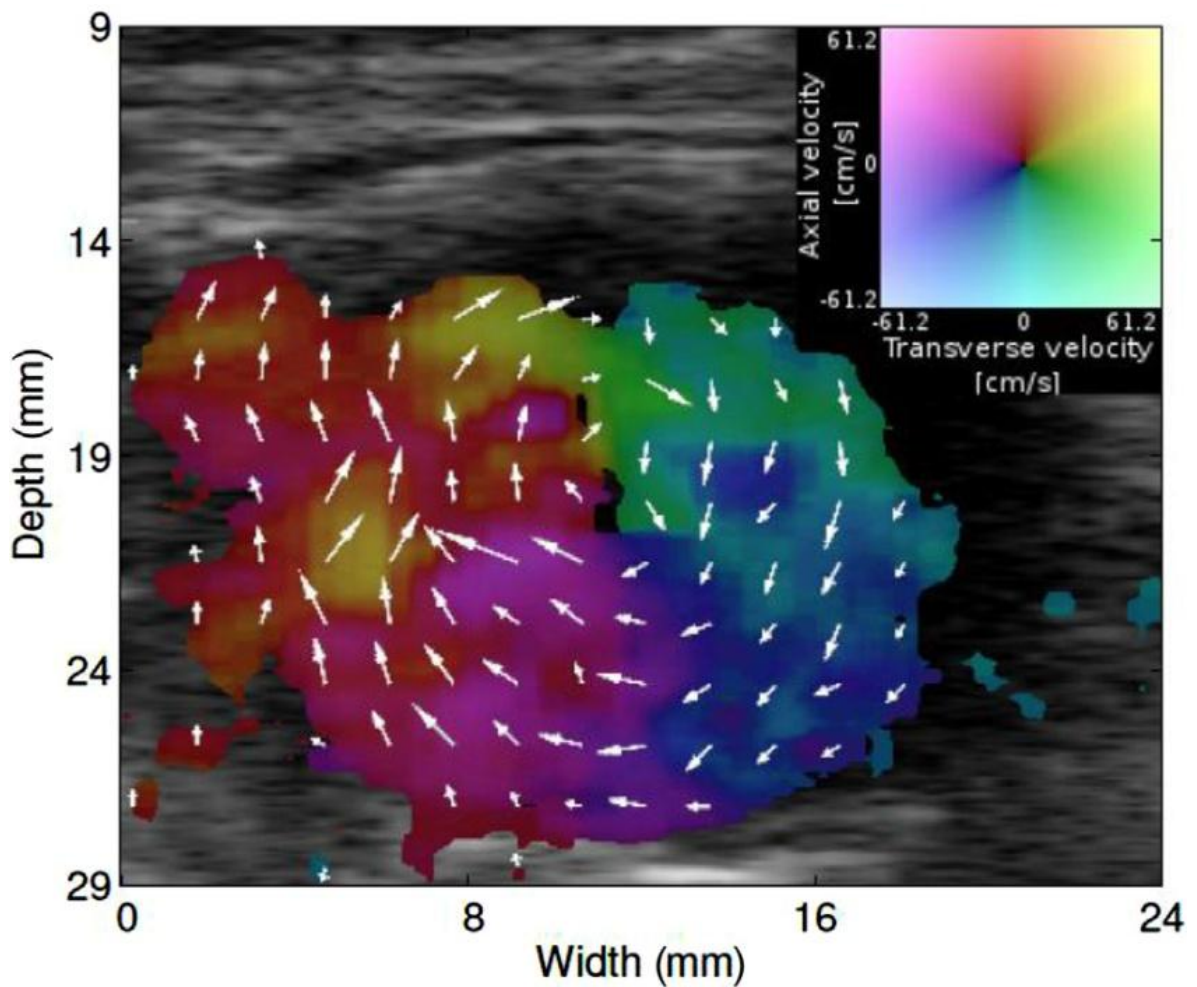
Figure 11.34. Real-time, In vivo vector flow ultrasound image of the abdominal aorta in the transverse plane using the TO method on a commercial system. The vector velocity color map is shown in the upper right corner. From Pedersen et al. (2011), IEEE. *T. L. Szabo, Diagnostic Ultrasound Imaging: Inside Out, © 2014 Elsevier Inc., All rights reserved..*
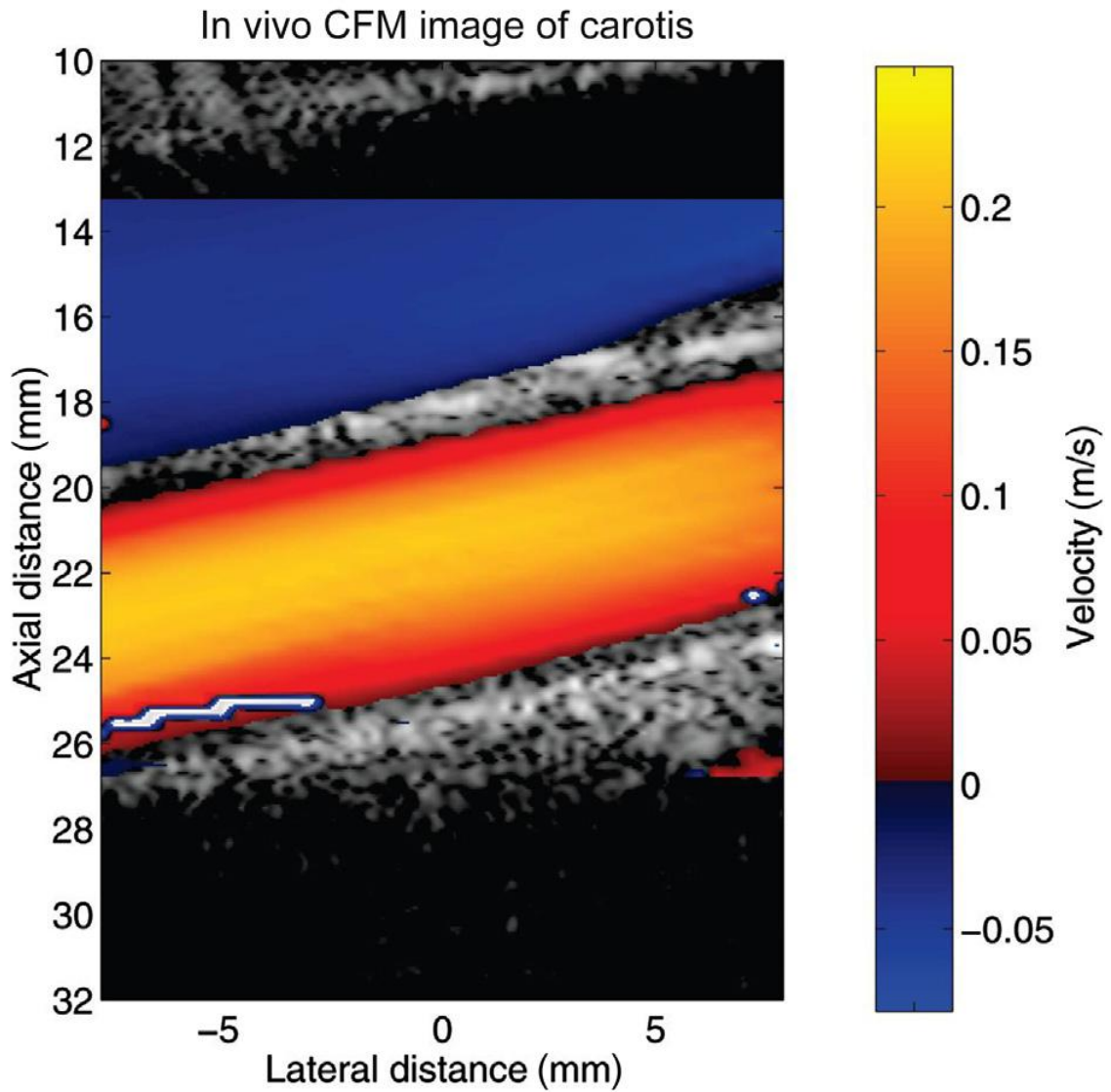
Figure 11.35. In vivo color flow map image at a 77 Flow angle for the jugular vein and carotid artery. The color scale indicates the velocity along the flow direction, where red hues indicate forward flow and blue reverse flow. From Jensen and Nikolov (2004), IEEE. *T. L. Szabo, Diagnostic Ultrasound Imaging: Inside Out, © 2014 Elsevier Inc., All rights reserved..*
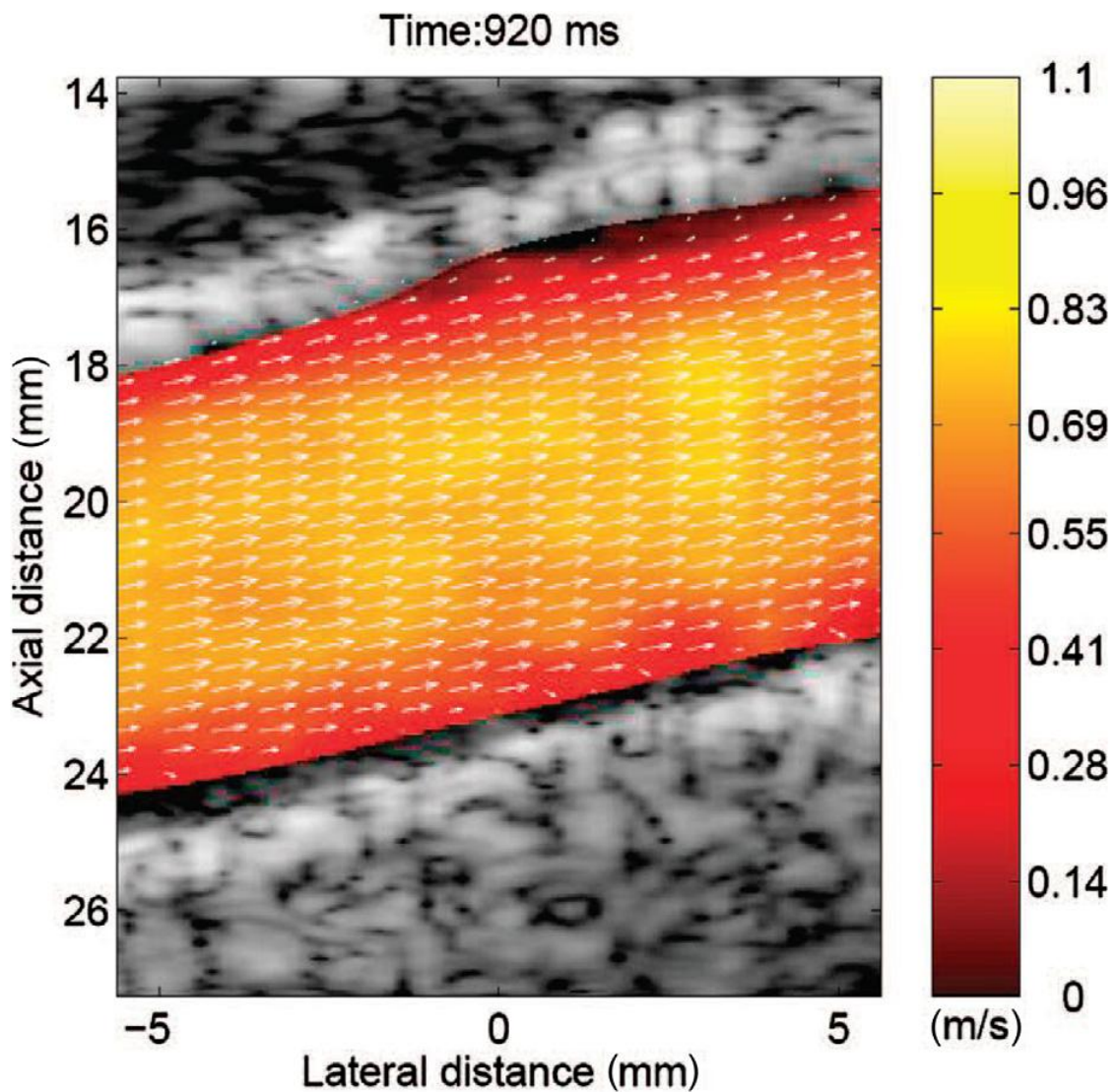
Figure 11.36. Vector velocity image of the common carotid artery shortly after the time of peak systole.The image was obtained from 40 plane-wave emissions, which gave a frame rate of 100 Hz. The vectors show the direction and magnitude of the flow and the colors show the magnitude of The flow. The dynamic range of the B-mode image is 40 dB. From Udesen et al. (2008), IEEE.*T. L. Szabo, Diagnostic Ultrasound Imaging: Inside Out, © 2014 Elsevier Inc., All rights reserved.*.
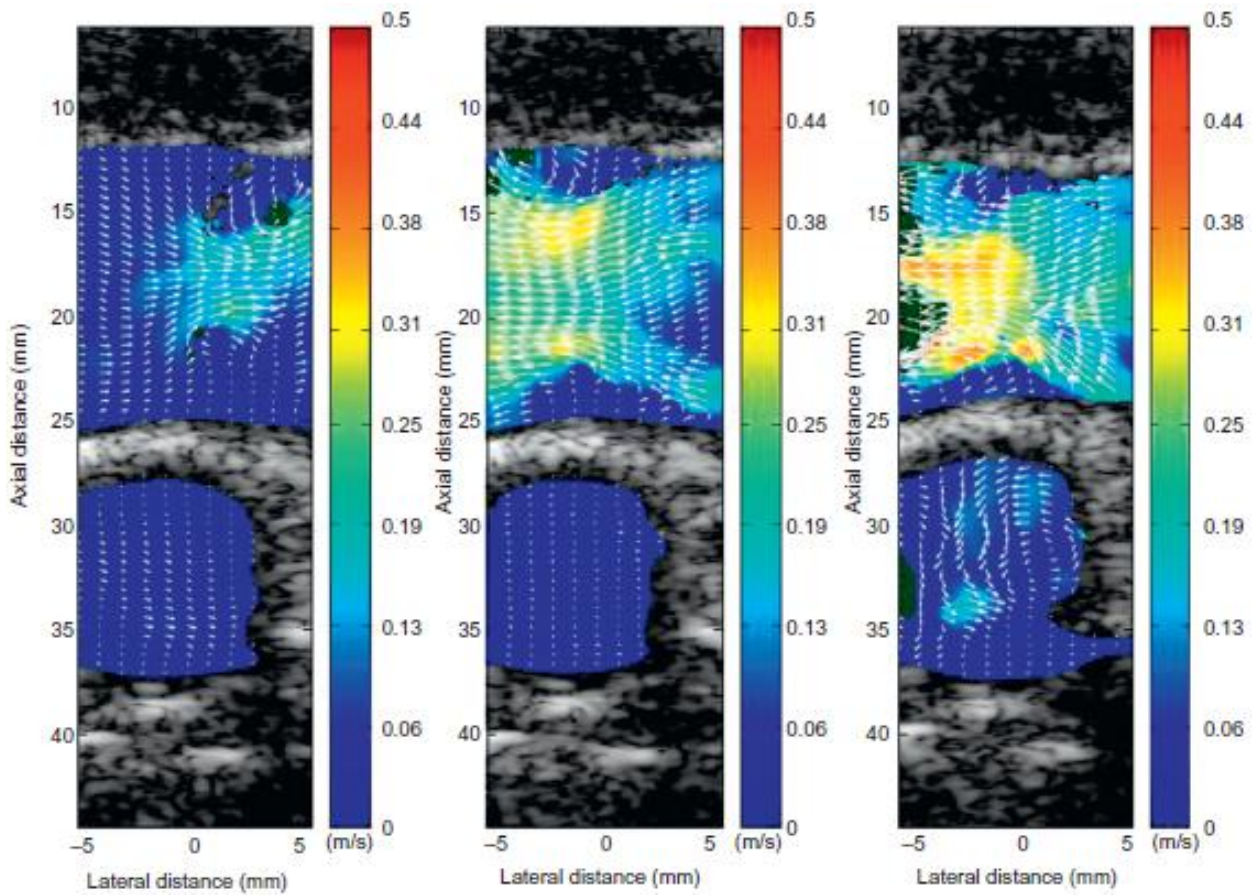
Figure 11.37. Plane-wave vector velocities in the jugular vein (Top) and the Carotid artery at three different times in the cardiac cycle. In the upper right of the top vessel in the left panel, reversed flow and a jet and vortices can be seen upstream from leaky valves. In the right panel, vortices were formed in the sinus pockets of the jugular vein behind the valves, during antegrade flow. In the carotid artery, secondary flow was seen during systole. From Jensen et al. (2011), IEEE, and Hansen et al. (2009). IEEE.*T. L. Szabo, Diagnostic Ultrasound Imaging: Inside Out, © 2014 Elsevier Inc., All rights reserved..*

Figure 11.38. Conceptual diagram of timing and spatial sequences in ultrafast Doppler. (Top) parameters for pulse transmission; (bottom) parameters on reception leading to output display. The constant E depends on processing and is approximately 10. Images from Bercoff et al. (2011). IEEE. *T. L. Szabo, Diagnostic Ultrasound Imaging: Inside Out, © 2014 Elsevier Inc., All rights reserved.*

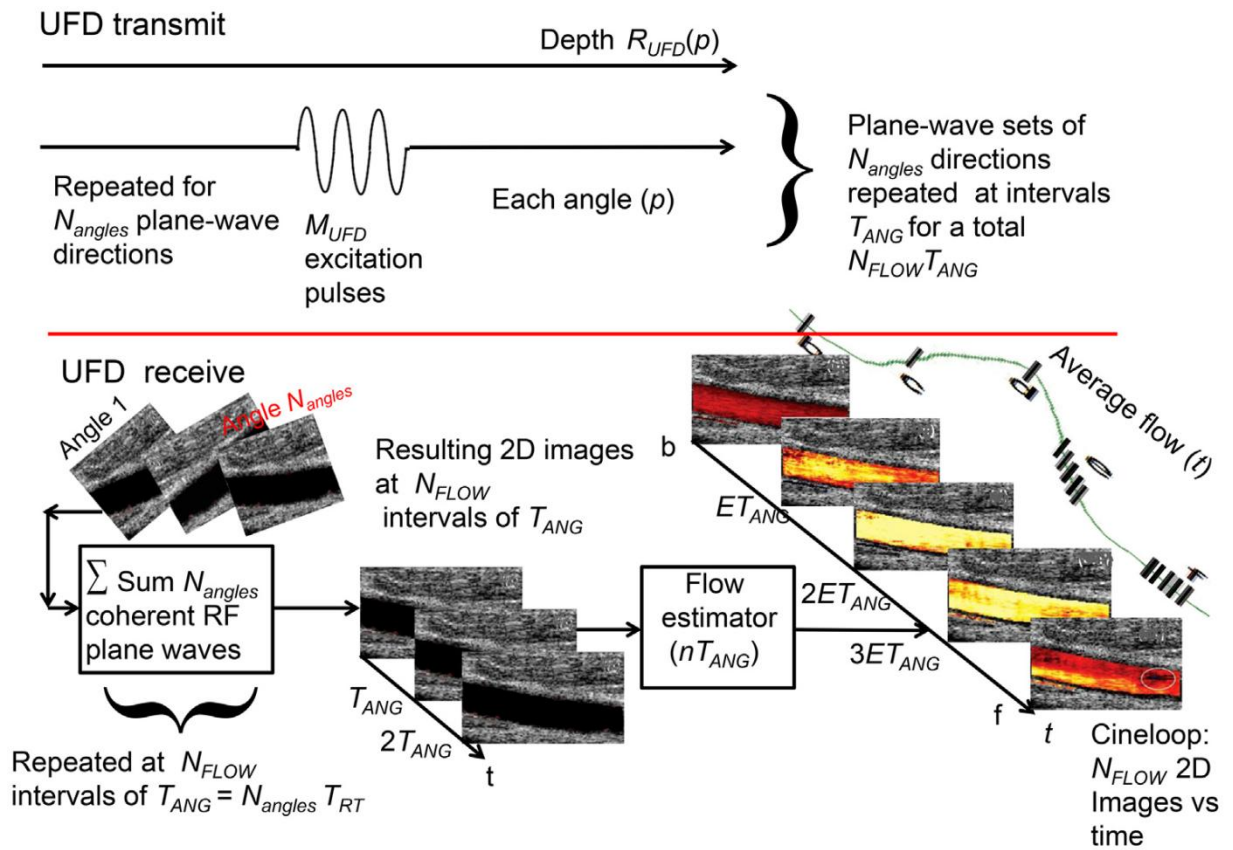Figure 11.39. Some selected frames of a complete cardiac cycle obtained with the ultrafast plane wave compounding. (A) Average flow in the artery indicating the selected frames; (B) before the opening of the aortic valve, there is a minimal laminar flow; (C and D) acceleration of the flow; (E) inversion of the parabolic profile in the deceleration; (F) local turbulence is present and propagates in the artery; (G and H) laminar flows in diastole. From Bercoff et al. (2011), IEEE. *T. L. Szabo, Diagnostic Ultrasound Imaging: Inside Out, © 2014 Elsevier Inc., All rights reserved..*
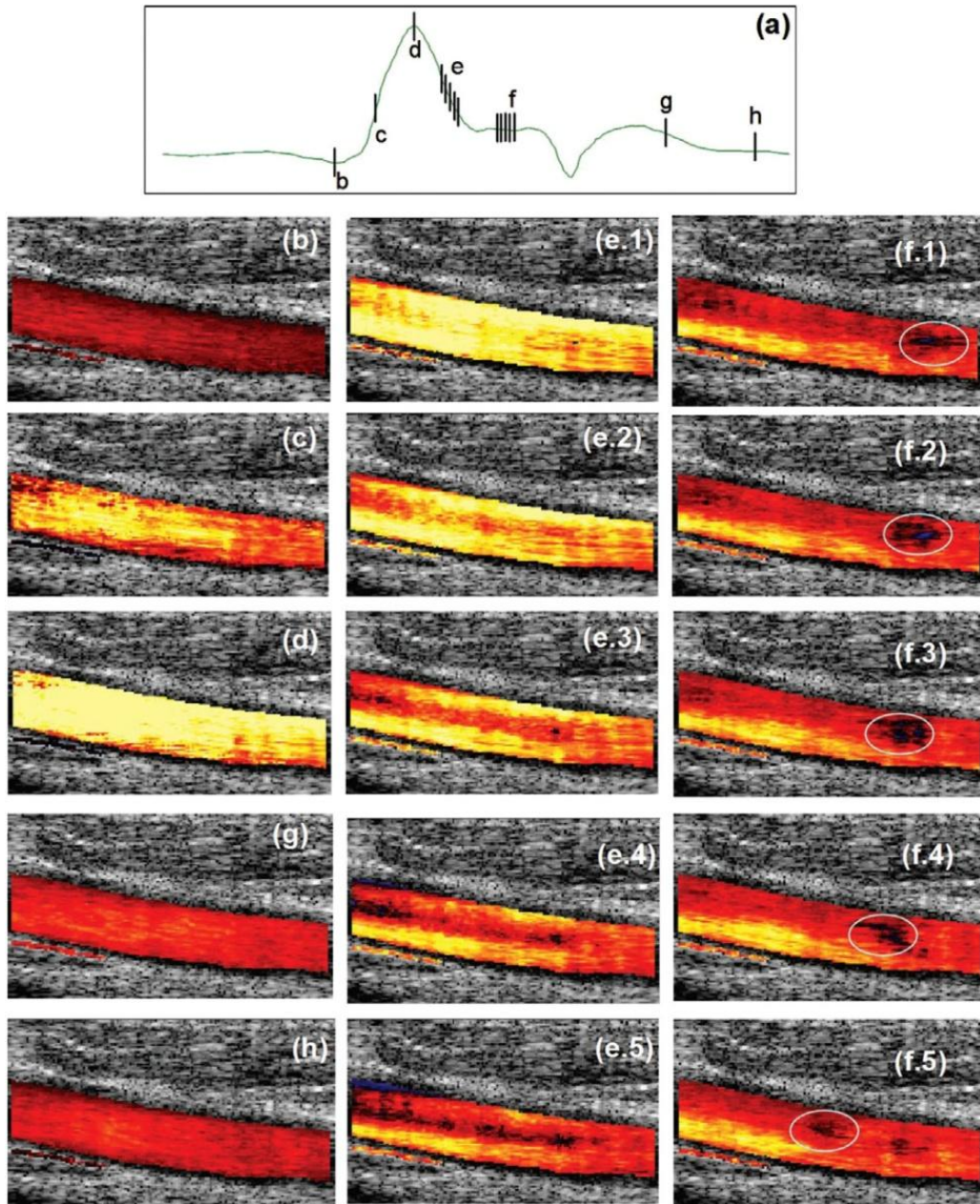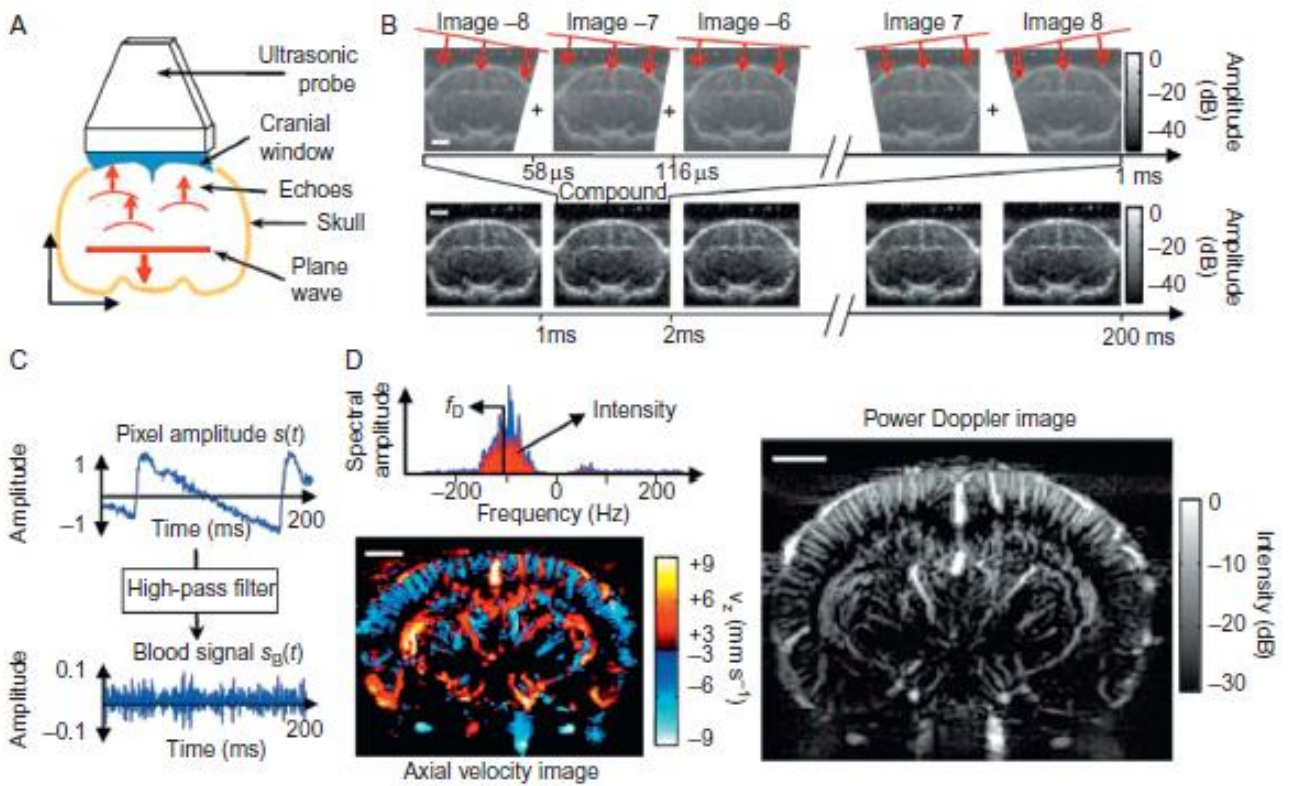
Figure 11.41. Principles for performing fUS in the rat brain. (A) Schematic setup depicting the ultrasonic probe, cranial window, and a schema of a coronal slice from the rat brain. (B) fUS is performed by emitting 17 planar ultrasonic waves tilted with different angles into the rat brain. The ultrasonic echoes produce 17 images of 232 cm. Summing these images results in a compound image acquired in 1 ms. The entire fUS sequence consists of acquiring 200 compound images in 200 ms. (C) Temporal variation s(t) of the backscattered ultrasonic amplitude in one pixel (normalized by the maximum amplitude). The blood signal s_B is extracted by applying a high-pass filter (same scale in the two graphs). (D) Frequency spectrum of s_B (top left). Two parameters are extracted from this spectrum the central frequency f_D, which is proportional to the axial blood velocity with respect to the z axis and gives rise to the axial velocity image (below left); and the intensity (power Doppler), which is proportional to the cerebral blood volume and gives rise to the power Doppler image (right). fUS is based on power Doppler images. Scale bars, 2 mm. From Mace et al. (2011),courtesy of Nature Methods. *T. L. Szabo, Diagnostic Ultrasound Imaging: Inside Out, © 2014 Elsevier Inc., All rights reserved.*.
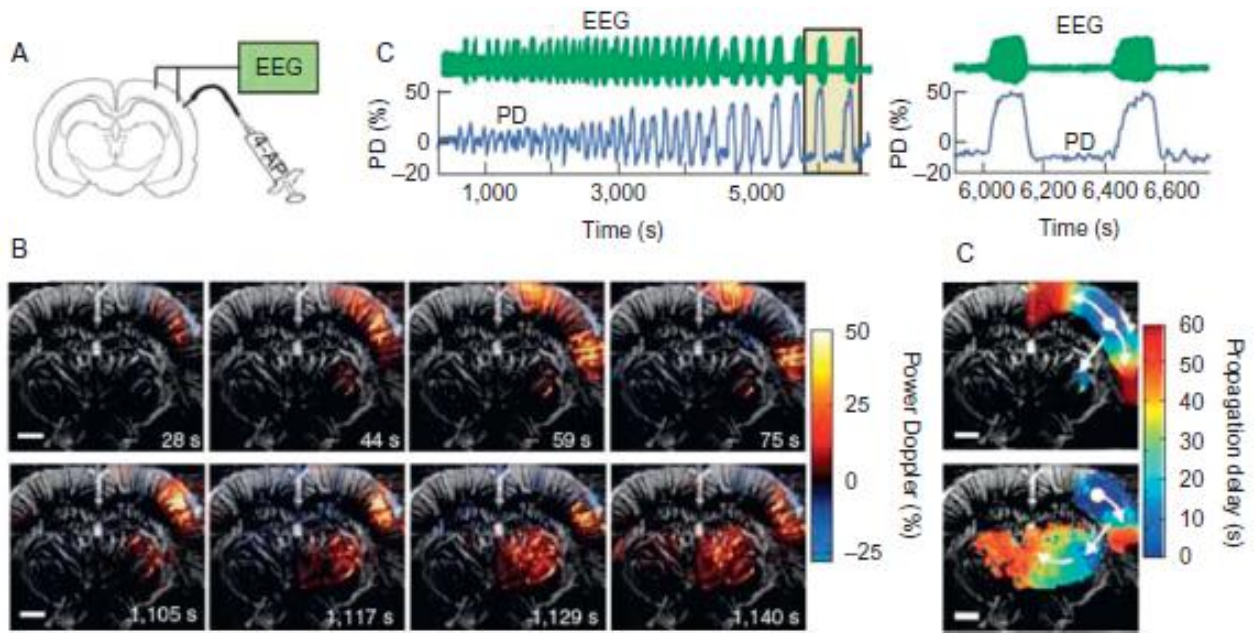
Figure 11.42. fUS Imaging of transient brain activity in a rat model of epilepsy. (A) Schematic setup for the imaging of epileptiform seizures. (B) Spatiotemporal spreading of epileptiform activity for two selected ictal events. The power Doppler signal (in % relative to baseline) is superimposed on a control power Doppler image. (C) Comparison between electrical recordings (EEG) and the power Doppler signal (PD) at the site of 4-AP injection. The two events in the shaded region are zoomed in on the graph at the right. (D) Maps of the propagation delay of blood volume changes from the focus to other regions (propagation delay in seconds is color coded following the legend on the right: onset is indicated in blue, and blue to red indicates delay increases). Arrows represent the direction of propagation. Scale bars, 2 mm. From Mace et al. (2011),courtesy of Nature Methods. *T. L. Szabo, Diagnostic Ultrasound Imaging: Inside Out, © 2014 Elsevier Inc., All rights reserved..*
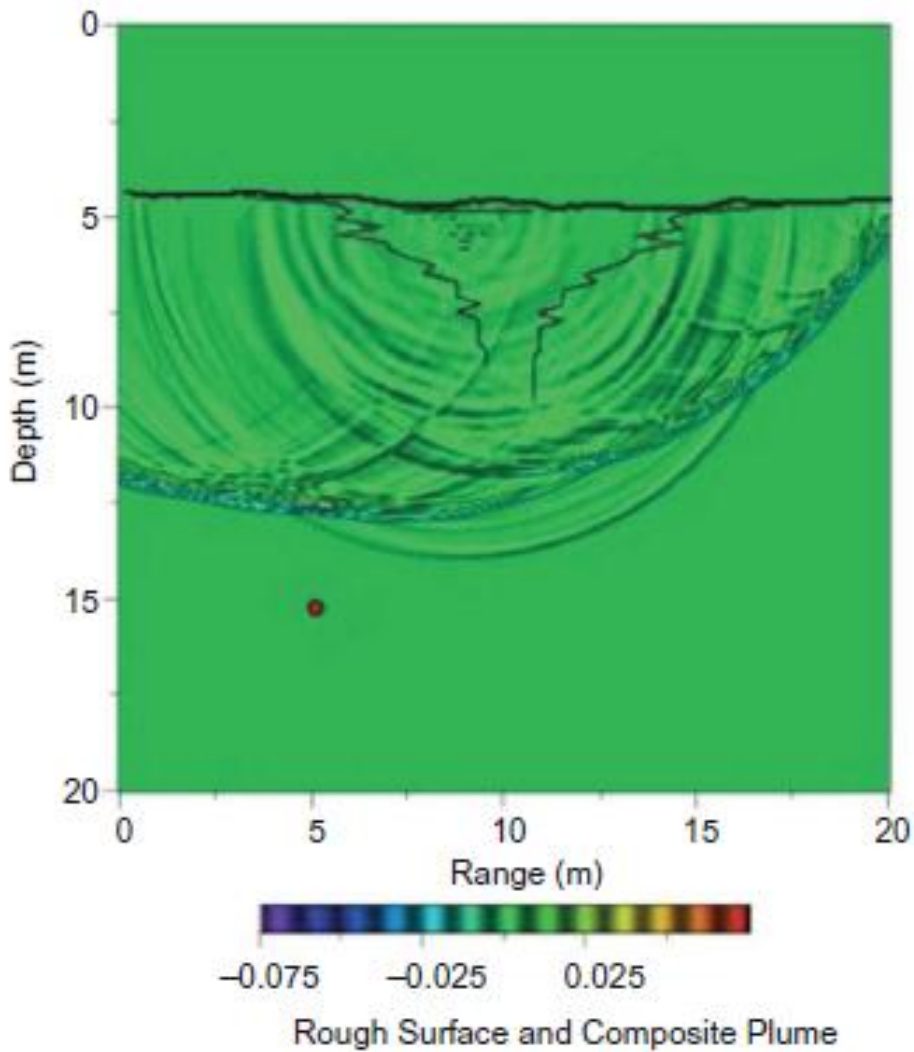
Figure 12.29. Two-dimensional solution for a point source radiating to a rough surface with a composite bubble plume. The bubble density within the plume as well as the horizontal area of the plume (in this case, the equivalent horizontal length) is assumed to decay exponentially with depth. From Norton (2009a), Mathematics and Computers in Simulation. *T. L. Szabo, Diagnostic Ultrasound Imaging: Inside Out, © 2014 Elsevier Inc., All rights reserved.*

Figure 12.30. Emitted ultrasound fields calculated by ASA and abersim. Fundamental and second harmonic fields at the focal depth (40 mm) are shown in the figure with 6 dB between two adjacent color lines. From Du et al. (2011b) IEEE. *T. L. Szabo, Diagnostic Ultrasound Imaging: Inside Out, © 2014 Elsevier Inc., All rights reserved.*

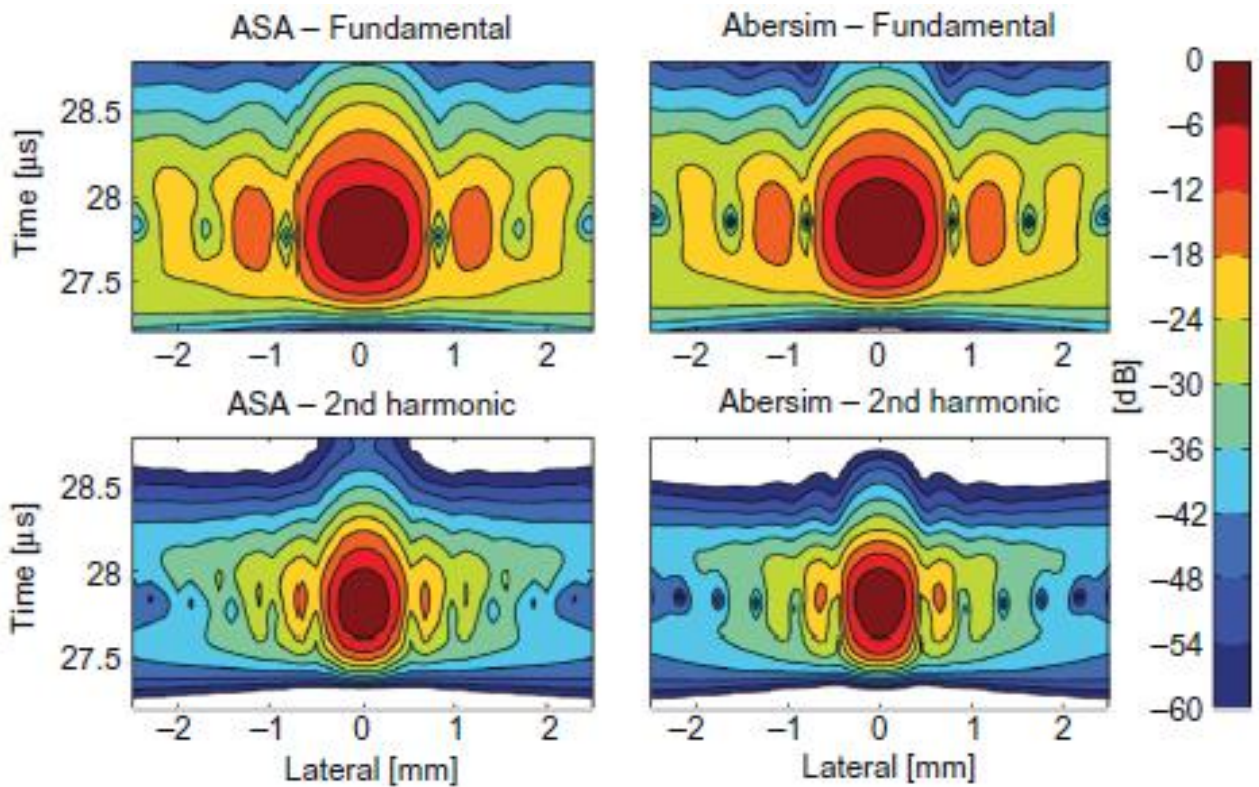Figure 12.32. Comparison of spatial shear wave displacement calculations to experimental data. (A) Experimental, (B) viscoelastic, and (C) purely elastic 3D plots of the spatial shear wave displacement pattern in the xz plane at a given sampling time. (D) Variation of those three fields along the x axis (at z50). The normalization is achieved first using the peak spatiotemporal displacement for each experiment. From Bercoff et al. (2004), IEEE. *T. L. Szabo, Diagnostic Ultrasound Imaging: Inside Out, © 2014 Elsevier Inc., All rights reserved.*

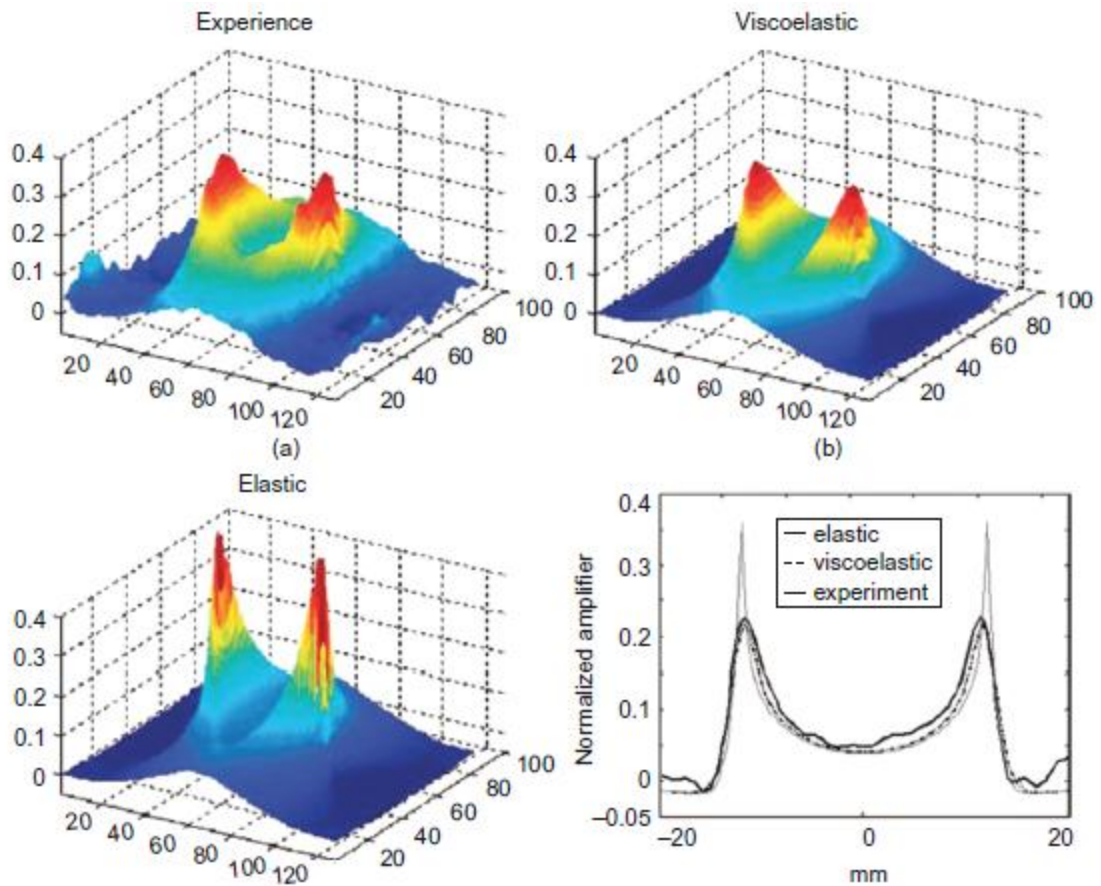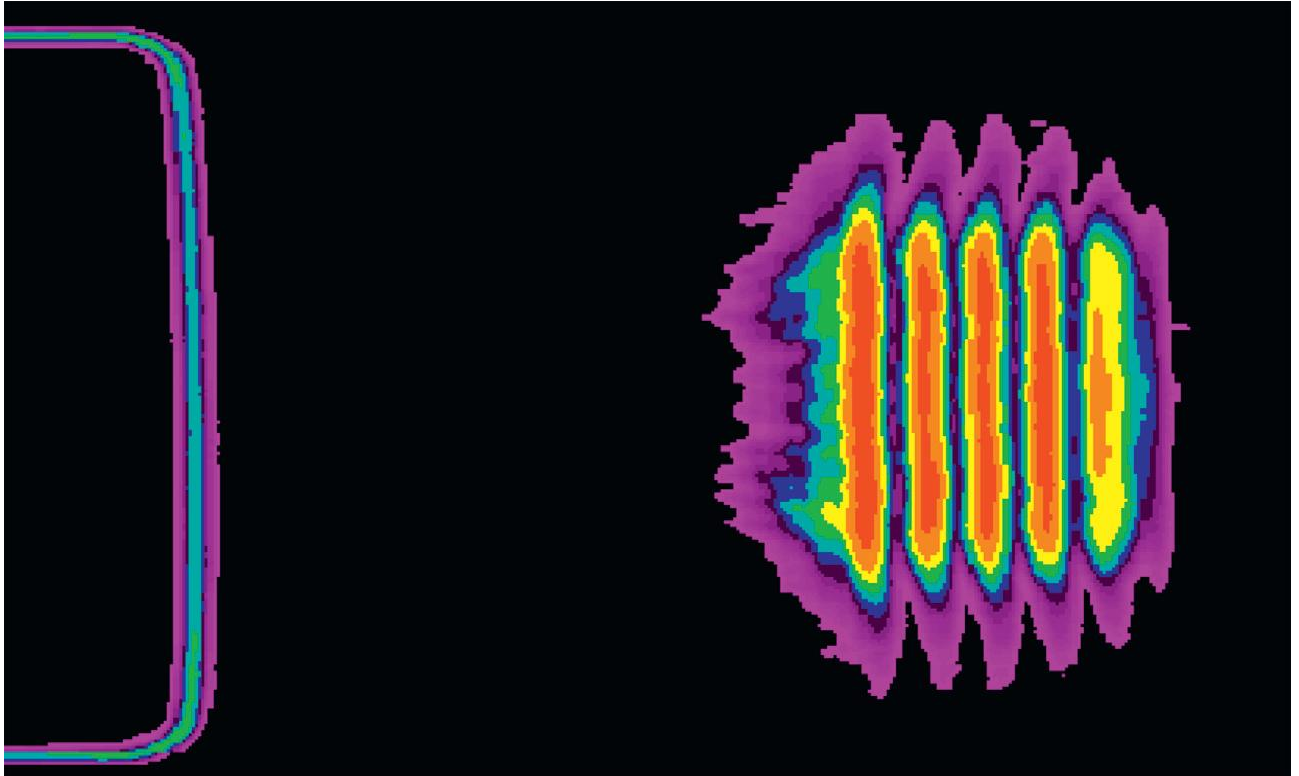Figure 13.10. Measurement of a pulsed wavefront of a focused beam by an Onda Schlieren System. Courtesy of C. I. Zanelli, Onda Corporation. *T. L. Szabo, Diagnostic Ultrasound Imaging: Inside Out, © 2014 Elsevier Inc., All rights reserved.*

Figure 13.23. Reconstructed Pressure Amplitude and Phase using Rayleigh Integral. (A) Photograph of transducer and amplitude and phase distribution of acoustic pressure reconstructed at the transducer aperture plane. From (A), the amplitude and phase distribution found at the aperture plane were used to calculate the acoustic field radiated by the source. (B) Projected acoustic pressures compared with measurements illustrate the accuracy of such a field projection along the transducer axis. Courtesy of O. Sapozhnikov. *T. L. Szabo, Diagnostic Ultrasound Imaging: Inside Out, © 2014 Elsevier Inc., All rights reserved.*

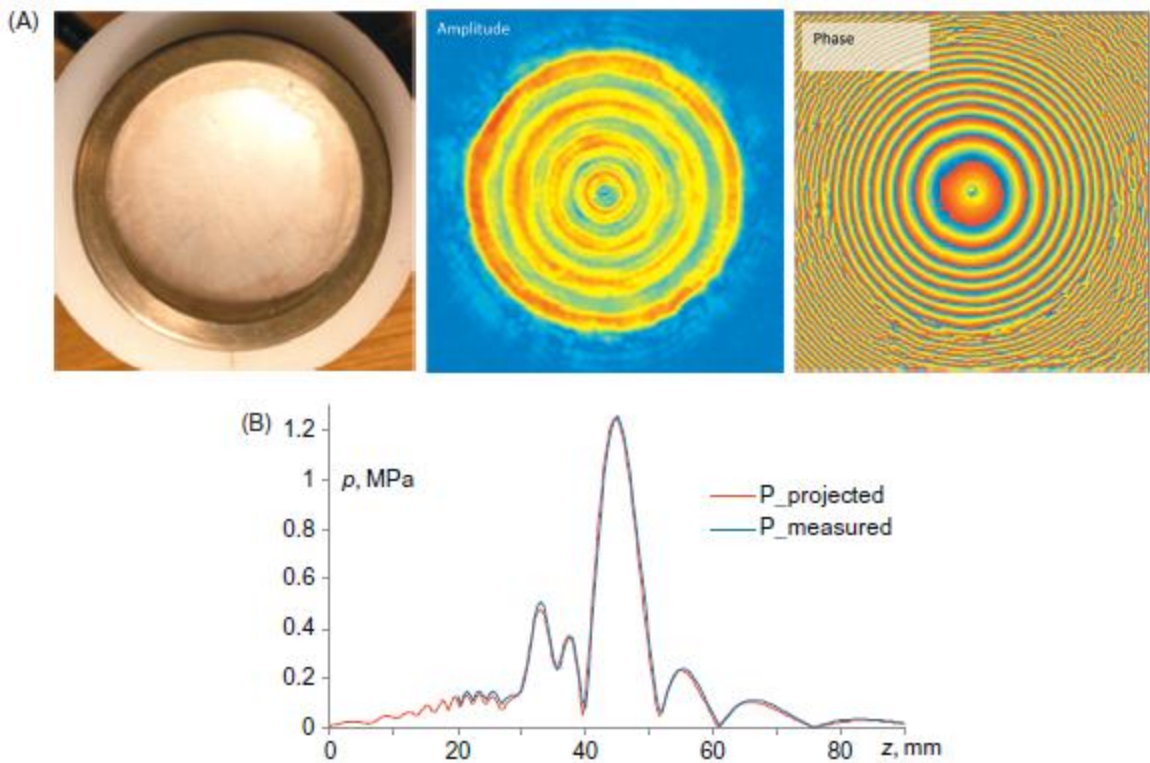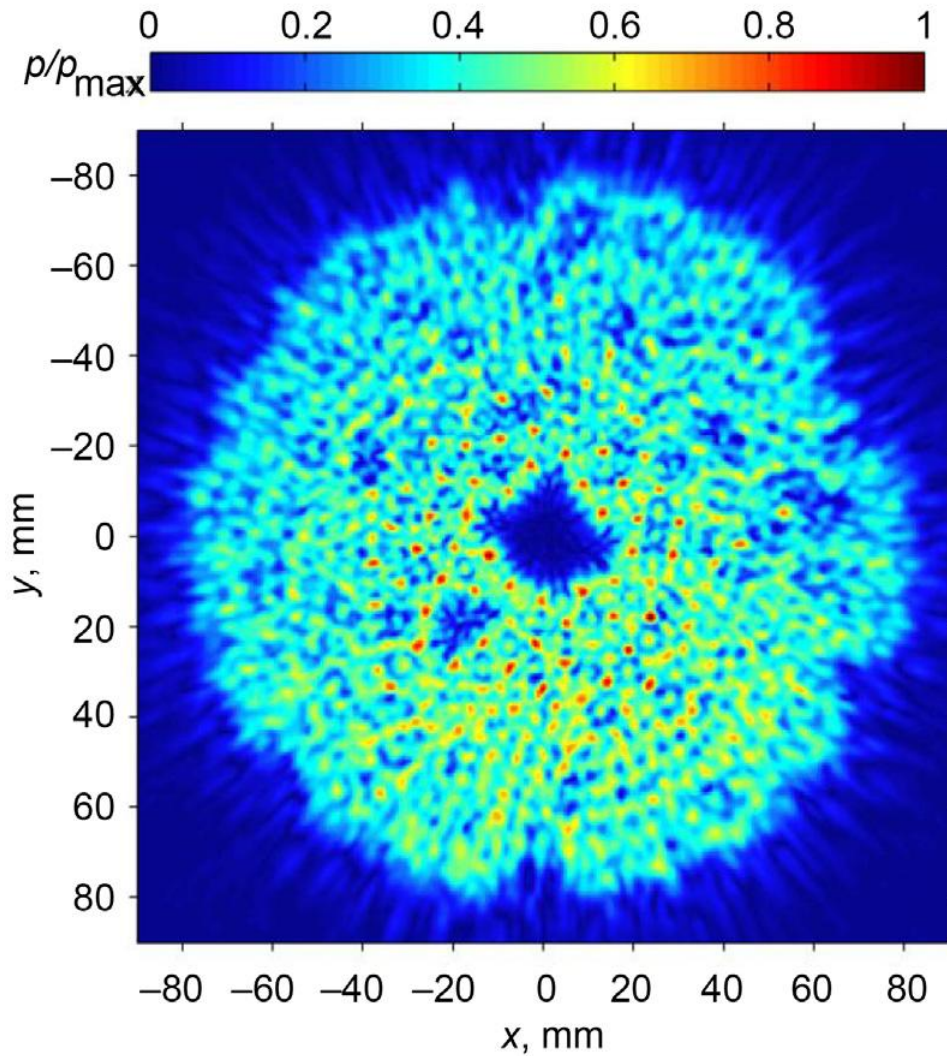Figure 13.24. Pressure magnitude at the Initial Plane of a Boundary
Condition Reconstructed from the Measured Hologram. From Yuldashev et
al. (2012), IEEE. *T. L. Szabo, Diagnostic Ultrasound Imaging: Inside Out,*
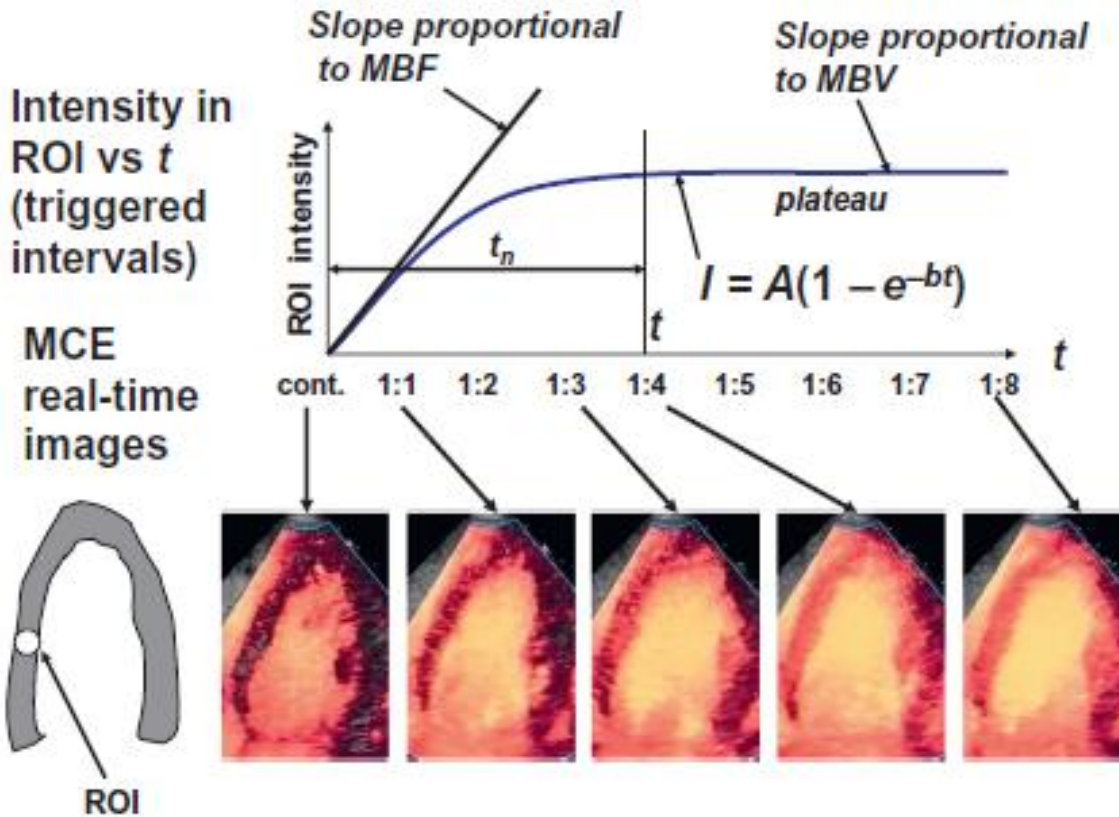*© 2014 Elsevier Inc., All rights reserved.*

Figure 14.19. Low-pressure (MI) real-time myocardial perfusion imaging method. (Top) graph of region of interest (ROI) intensity versus time perfusion filling curve, showing initial slope proportional to myocardial blood flow (MBF), a plateau region with a slope proportional to myocardial blood volume (MBV), and a time (tn) to reach the plateau. Time is in triggered-interval ratios such as 1:8, meaning an interval eight times the basic unit with reference to initial administration of contrast, depicted as "cont." (Bottom left) insert highlights ROI for intensity measurement. (Bottom right) time sequence series of left ventricle views depicting perfusion of the myocardium and beginning with contrast agent entering the left ventricle. Courtesy of P. G. Rafter, Philips Healthcare. *T. L. Szabo, Diagnostic Ultrasound Imaging: Inside Out, © 2014 Elsevier Inc., All rights reserved.*
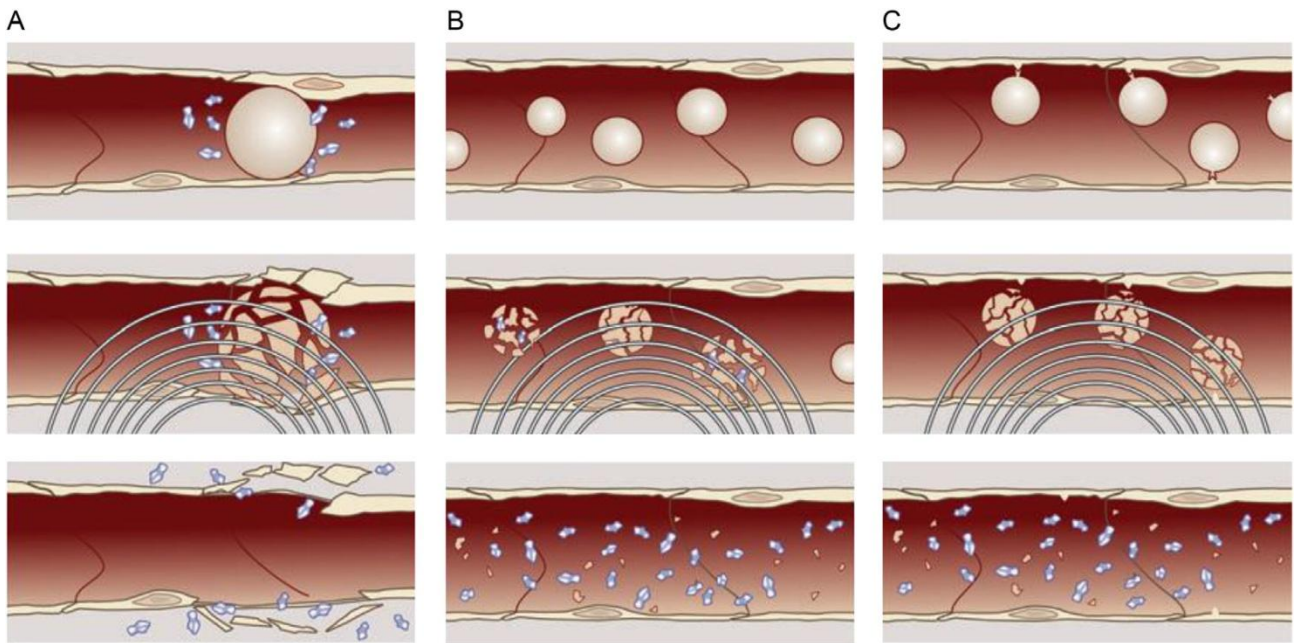
Figure 14.24. Deliberate local bubble destruction of contrast agents at intended sites. (A) Ultrasound contrast agents are freely circulating in small vessels along with drug particles (blue/light gray irregularly shaped particles surrounding microbubble at top of (A)). Once a sufficiently strong ultrasound pulse is applied to the area, the contrast agent expands, rupturing the endothelial lining. Drug is then able to extravasate. (B) Drug-laden ultrasound contrast agents are freely circulating throughout the vasculature. A pulse of ultrasound is applied and ruptures the contrast agent, thereby liberating the drug payload. Because ultrasound is only applied in the region of interest, drug is preferentially delivered locally. (C) Drug-laden ultrasound contrast agents bearing surface ligands targeted to specific endothelial receptors are freely circulating. The ligand preferentially binds the ultrasound contrast agent in the target region, increasing local agent accumulation. An ultrasound pulse is then applied, liberating the drug payload. From Ferrara, Pollard, and Borrden (2007), Annual Review Biomedical Engineering. *T. L. Szabo, Diagnostic Ultrasound Imaging: Inside Out, © 2014 Elsevier Inc., All rights reserved.*
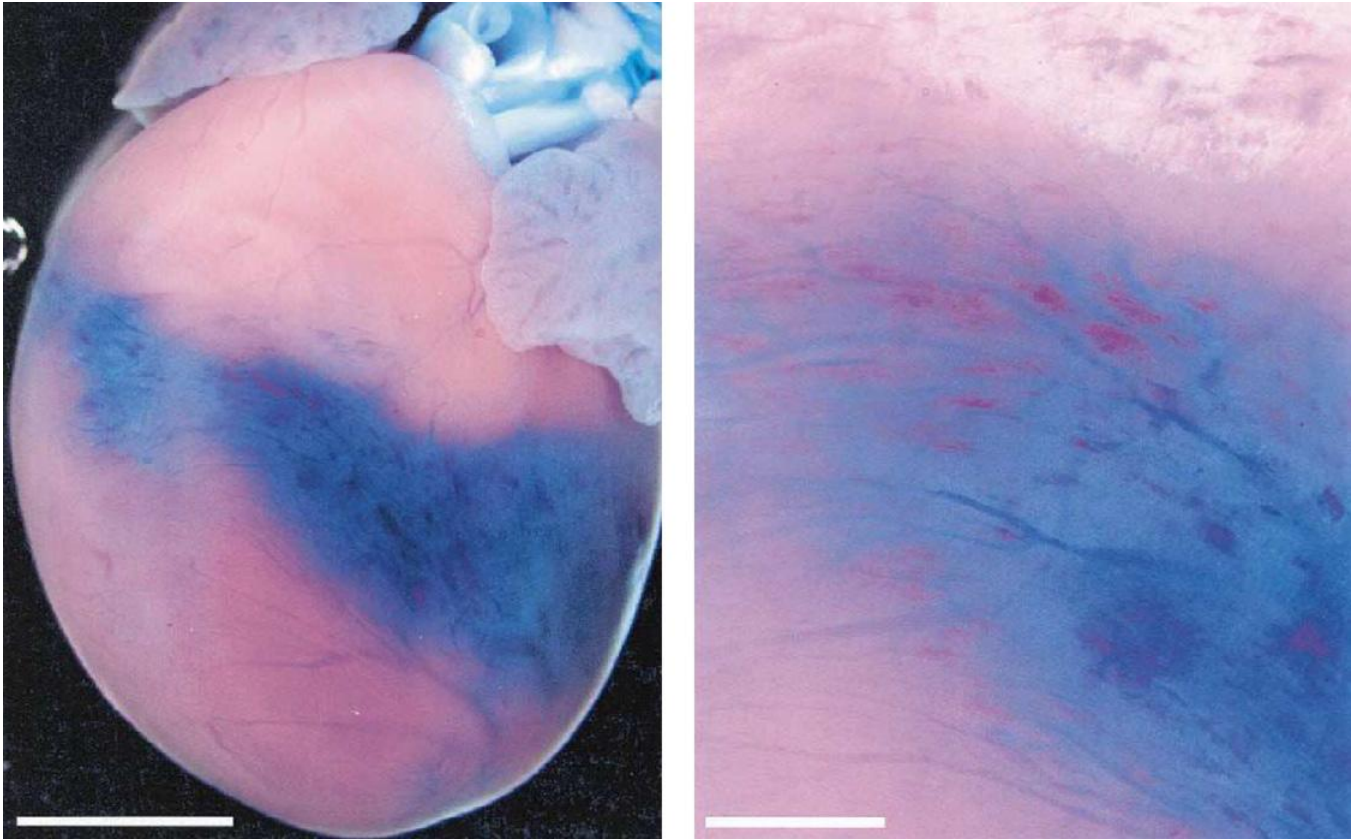
Figure 14.25. Localized extravasation in a rat heart. Photographs of an excised rat heart exposed at 1.9 MPa, 1:4 end-systole triggering, and 100 µl/kg of contrast agent. The petechia and Evans-blue leakage are evident in a band across the myocardium (bottom, scale bar 5 mm). The erythrocyte extravasation (petechiae) and diffuse leakage of the dye are shown in a close-up view of the same heart (top, scale bar 1 mm). From Li et al. (2003), with permission from the World Federation of Ultrasound in Medicine and Biology. *T. L. Szabo, Diagnostic Ultrasound Imaging: Inside Out, © 2014 Elsevier Inc., All rights reserved.*
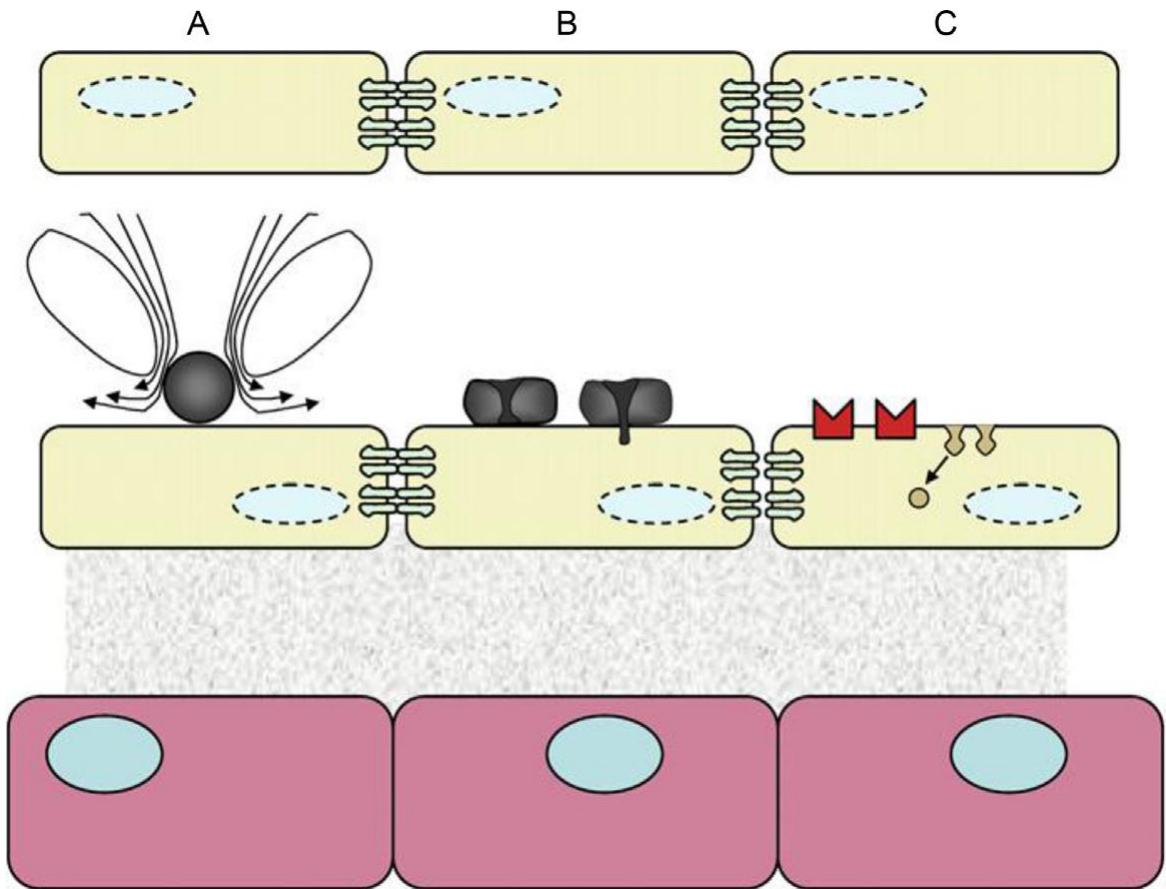
Figure 14.27. Hypothesized Mechanisms of Drug Transport Across Endothelium. (A) Local shear stress created on cell during microbubble oscillation; (B) fluid jet formation; (C) intracellular transport, hypothesized to result from the stresses induced by microbubble activity, including generation of gaps at tight junctions, expression of cell adhesion molecules due to inflammatory process, and the creation of vesicles for transcellular transport. From Qin, Caskey and Ferrara (2009), Physics in Medicine and Biology,r IOP Publishing. Reproduced by permission of IOP Publishing. All rights reserved. *T. L. Szabo, Diagnostic Ultrasound Imaging: Inside Out, © 2014 Elsevier Inc., All rights reserved.*

Figure 14.31. Cavitation Images of a Vessel Phantom Through a Water Path at Different MIs. Showing dominant moderate oscillations (left), dominant stable cavitation (center), and dominant inertial cavitation (right). The corresponding MIs are indicated, and the average spectrum over the region of interest outlined with a blue trapezoid is displayed in logarithmic scale. From Vignon, Shi, et al. (2013), IEEE. *T. L. Szabo, Diagnostic Ultrasound Imaging: Inside Out, © 2014 Elsevier Inc., All rights reserved.*

Figure 15.6. Interrelated Acoustic and Biophysical Events Involved in Ultrasound-induced Bioeffects. *T. L. Szabo, Diagnostic Ultrasound Imaging: Inside Out, © 2014 Elsevier Inc., All rights reserved.*
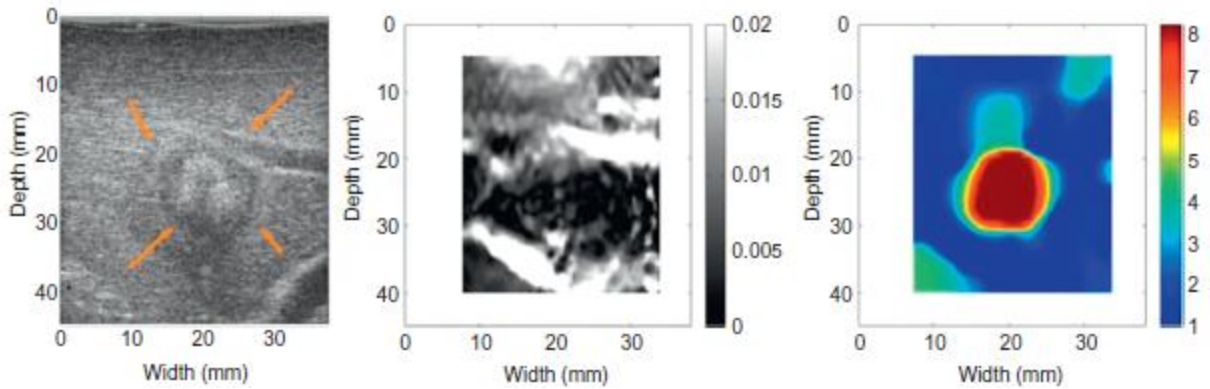
Figure 16.11. (A) Sonogram; (B) Strain elastogram; and (C) Modulus elastogram of RF Ex vivo ablated bovine liver. Courtesy of Drs T. J. Hall, T. Varghese, and J. Jiang (University of Wisconsin, Madison); from Doyley (2012) Physics in Medicine and Biology, © IOP Publishing. Reproduced by permission of IOP Publishing. All rights reserved. *T. L. Szabo, Diagnostic Ultrasound Imaging: Inside Out, © 2014 Elsevier Inc., All rights reserved.*
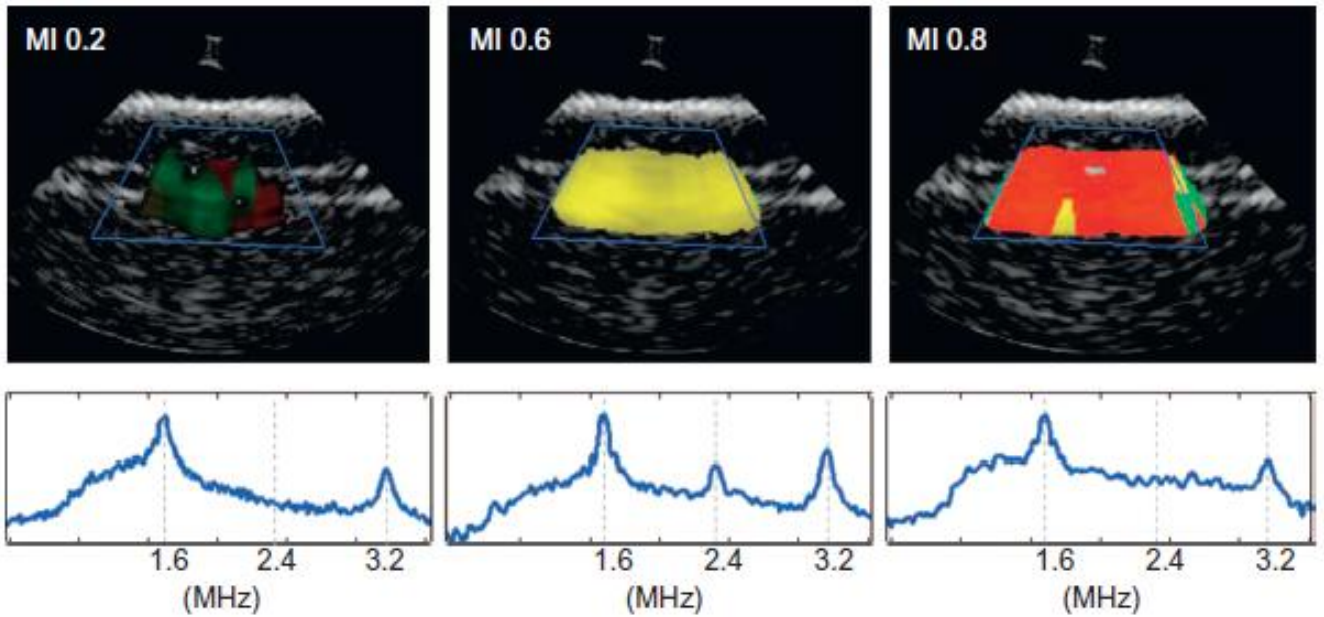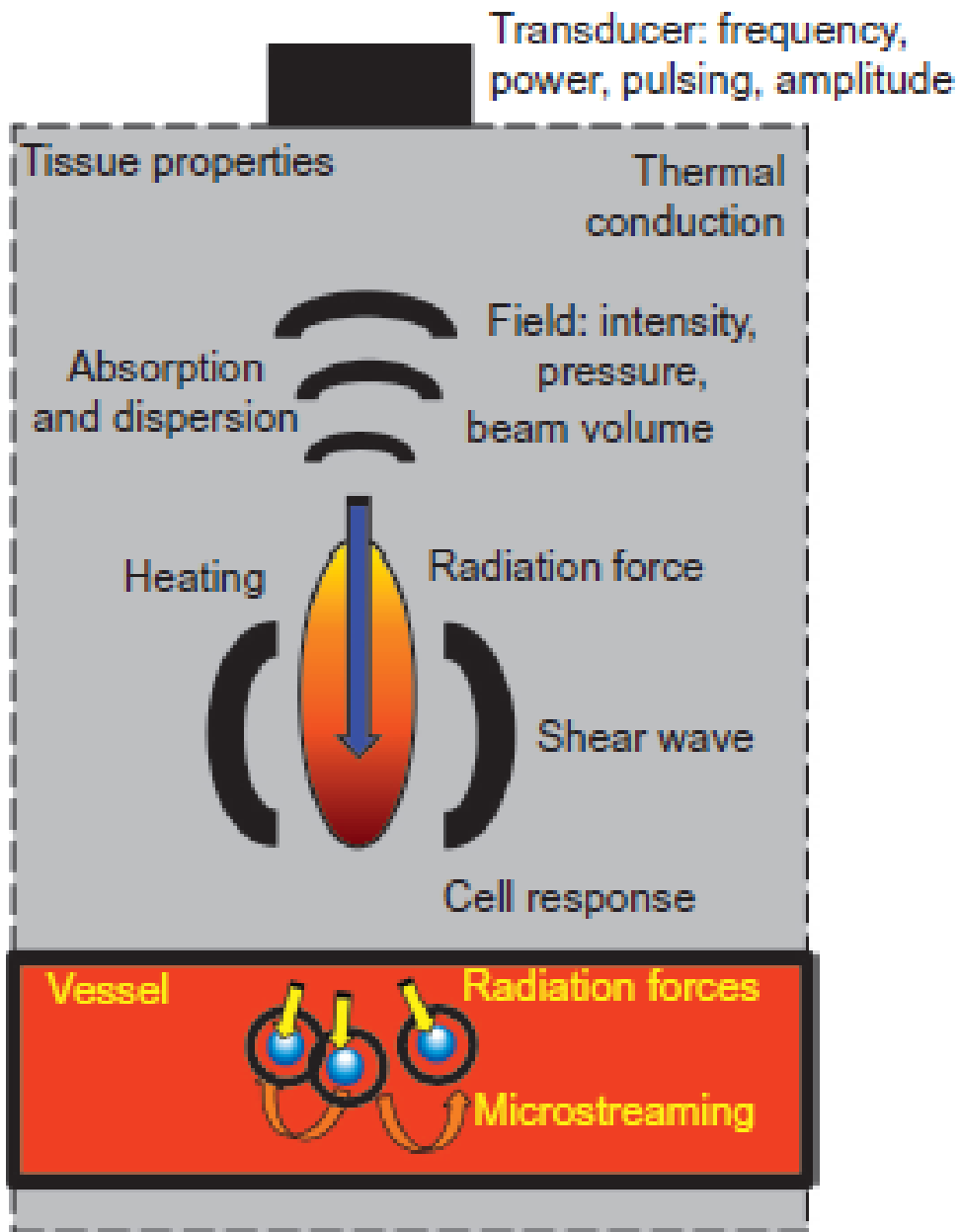
Figure 16.14. Pelvic sonogram and elastogram. Courtesy of Philips Healthcare. *T. L. Szabo, Diagnostic Ultrasound Imaging: Inside Out, © 2014 Elsevier Inc., All rights reserved.*

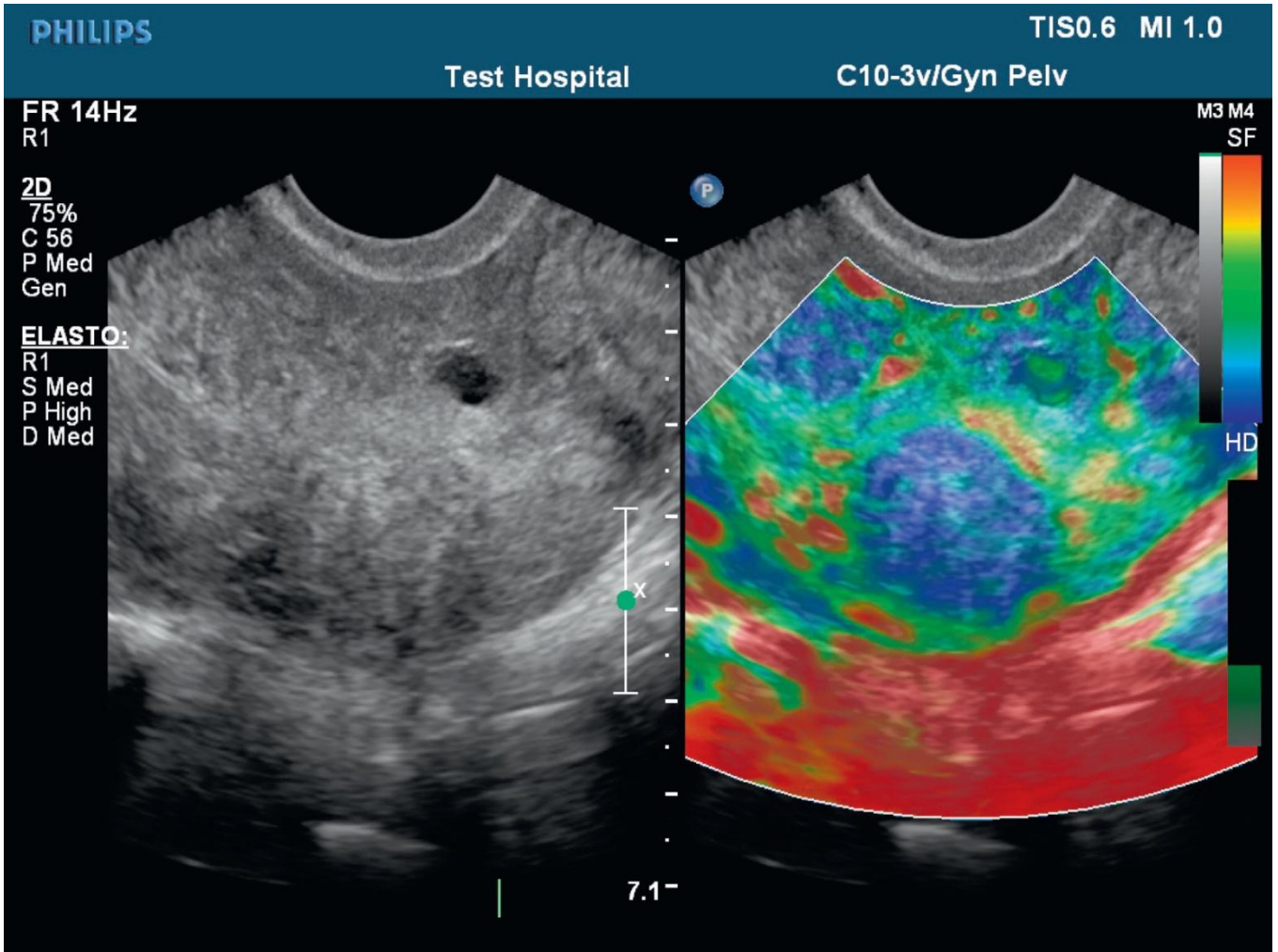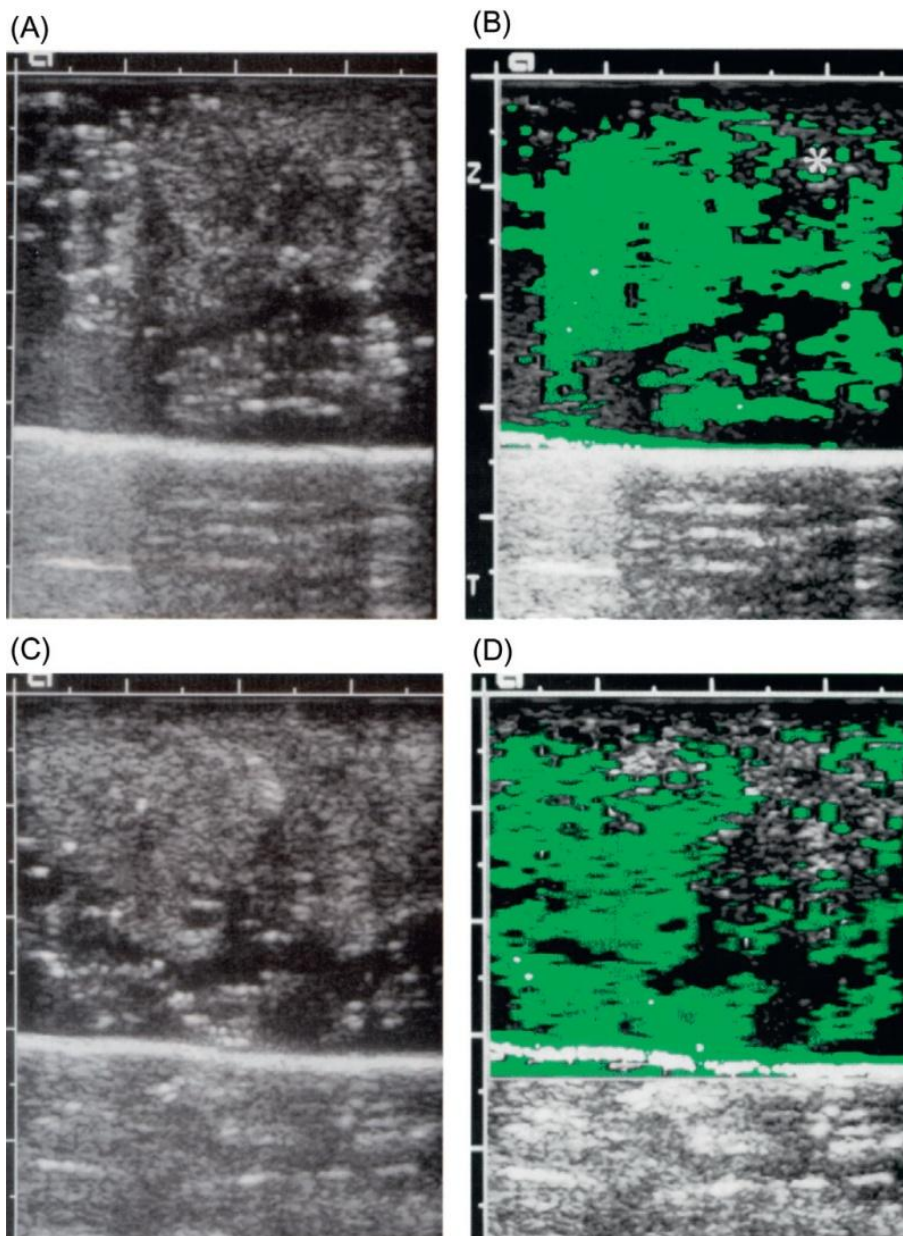Figure 16.15. Diffuse carcinoma demonstrated at multiple frequencies in a 69-year-old man with no palpable abnormality and a serum PSA level of 6.7 ng/ml. (A) Standard prone transverse ultrasound image obtained at the base of the prostate demonstrates somewhat heterogeneous echo texture; (B) corresponding sonoelasticity image obtained at 50 Hz shows poor vibration diffusely, most pronounced posteriorly on the right (); (C) a second section of the base, obtained slightly caudal to (A), shows a heterogeneous gray-scale pattern; (D) corresponding sonoelasticity image obtained at 150 Hz documents absent bilateral posterior and right anterior vibration. From Rubens et al. (1995); reprinted with permission from RSNA. *T. L. Szabo, Diagnostic Ultrasound Imaging: Inside Out, © 2014 Elsevier Inc., All rights reserved.*
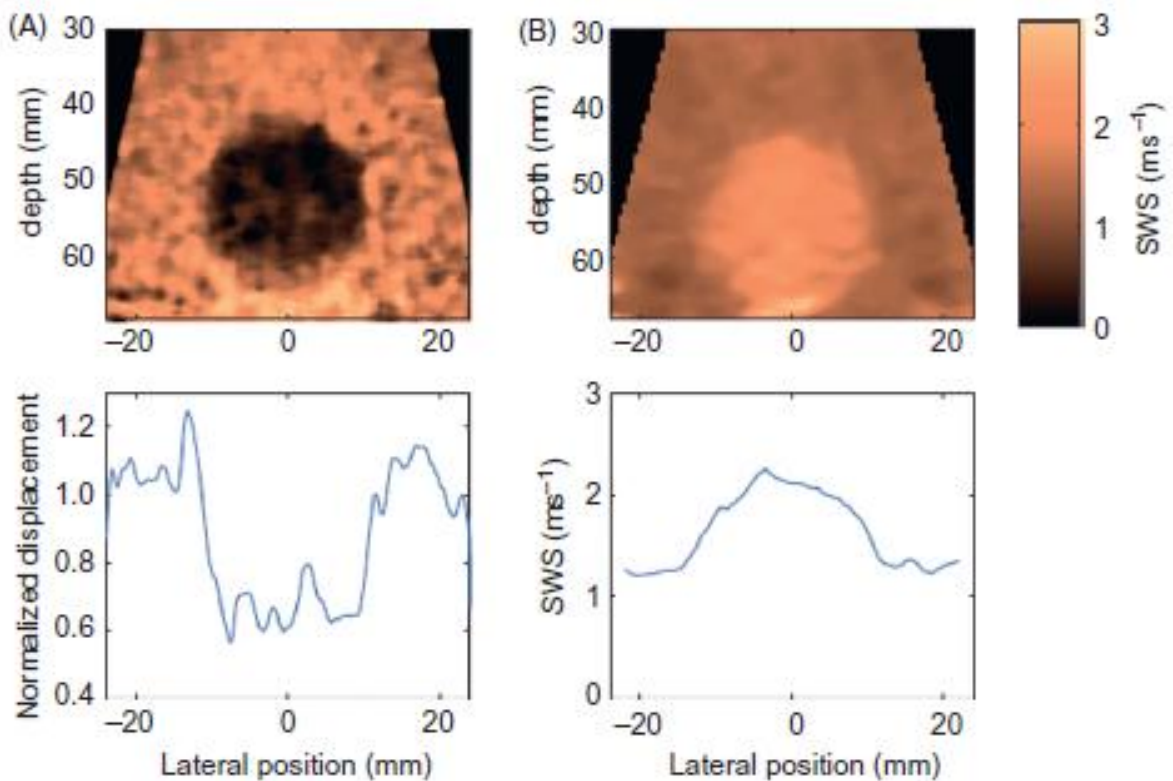
Figure 16.16. Matched (A) ARFI and (B) SWEI images of a calibrated elasticity phantom with a 20-mm-diameter stiff spherical inclusion. The images were generated from the same dataset, which was obtained with a 4-MHz abdominal imaging array, using parallel receiving beamforming techniques to monitor the tissue response to each excitation throughout the entire field of view. A total of 88 excitation pulses were located at two focal depths (50 and 60 mm), with a beam spacing of 1 mm. The ARFI image portrays normalized displacement at 0.7 ms after each excitation, whereas the SWEI image portrays reconstructed shear wave speed. The lesion contrast is 0.37 and 0.71 for the ARFI and SWEI images, respectively, and the edge resolution (2080%) is 1.2 mm (ARFI) and 5.0 mm (SWEI) in the plots from a depth of 50 mm, shown in the bottom row. From Palmeri and Nightingale (2011) Interface Focus,© IOP Publishing. Reproduced by permission of IOP Publishing. All rights reserved. *T. L. Szabo, Diagnostic Ultrasound Imaging: Inside Out, © 2014 Elsevier Inc., All rights reserved.*
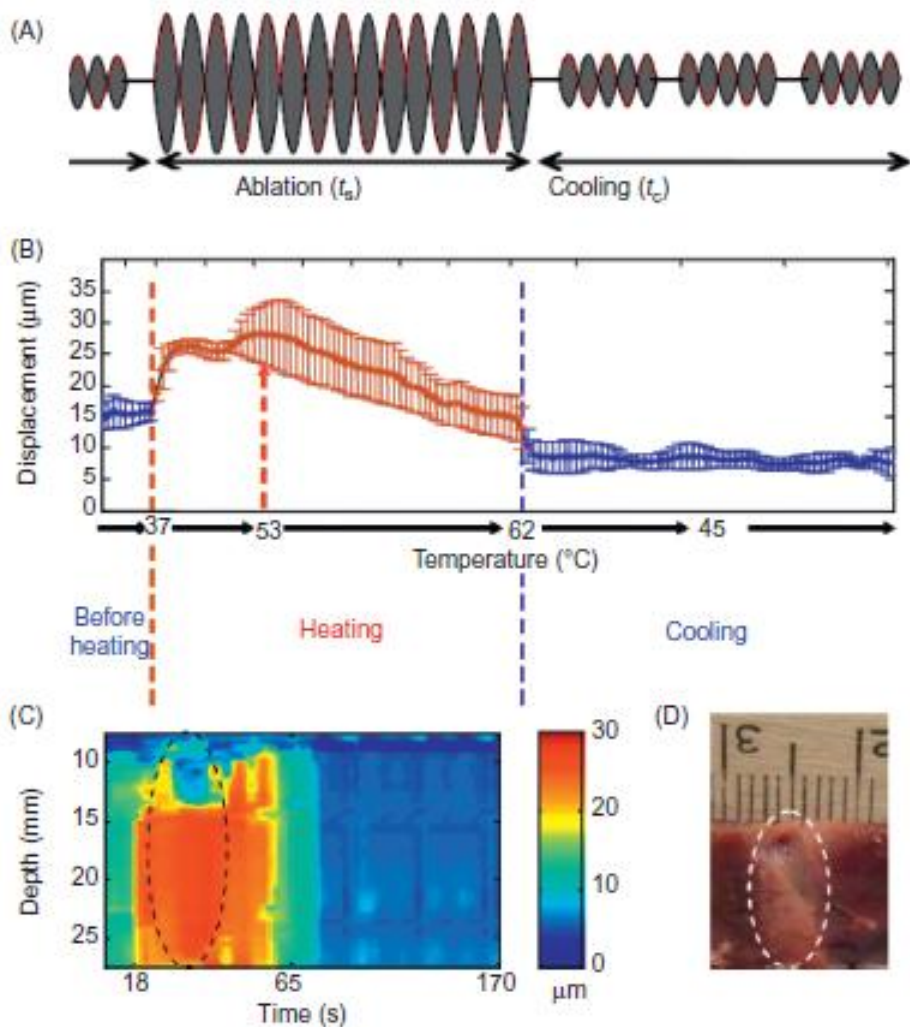
Figure 16.19. M-mode HMI, Real-time HMFU Monitoring. (A) The HMIFU sequence used before, during, and after HIFU treatment; (B) HMI displacement variation with temperature before (blue), during (orange), and after (blue) HIFU ablation, averaged over five different liver specimens and 3 locations in each liver, i.e. 15 locations total; (C) example of an M-mode HMI displacement image obtained in real time during ablation (as in (A) and (B); heating started at t518 s and ended at t565 s); (D) photograph of the liver lesion (denoted by the dashed contour). A liver vessel running through the lesion was used as a registration reference between the images in (C) and (D). Note that in (B) at 53 C, coagulation occurs and the HMI displacement changes from a positive to a negative rate, indicating lesion formation. From Konofagou et al. (2012) courtesy of Current Medical Imaging Reviews. *T. L. Szabo, Diagnostic Ultrasound Imaging: Inside Out, © 2014 Elsevier Inc., All rights reserved.*
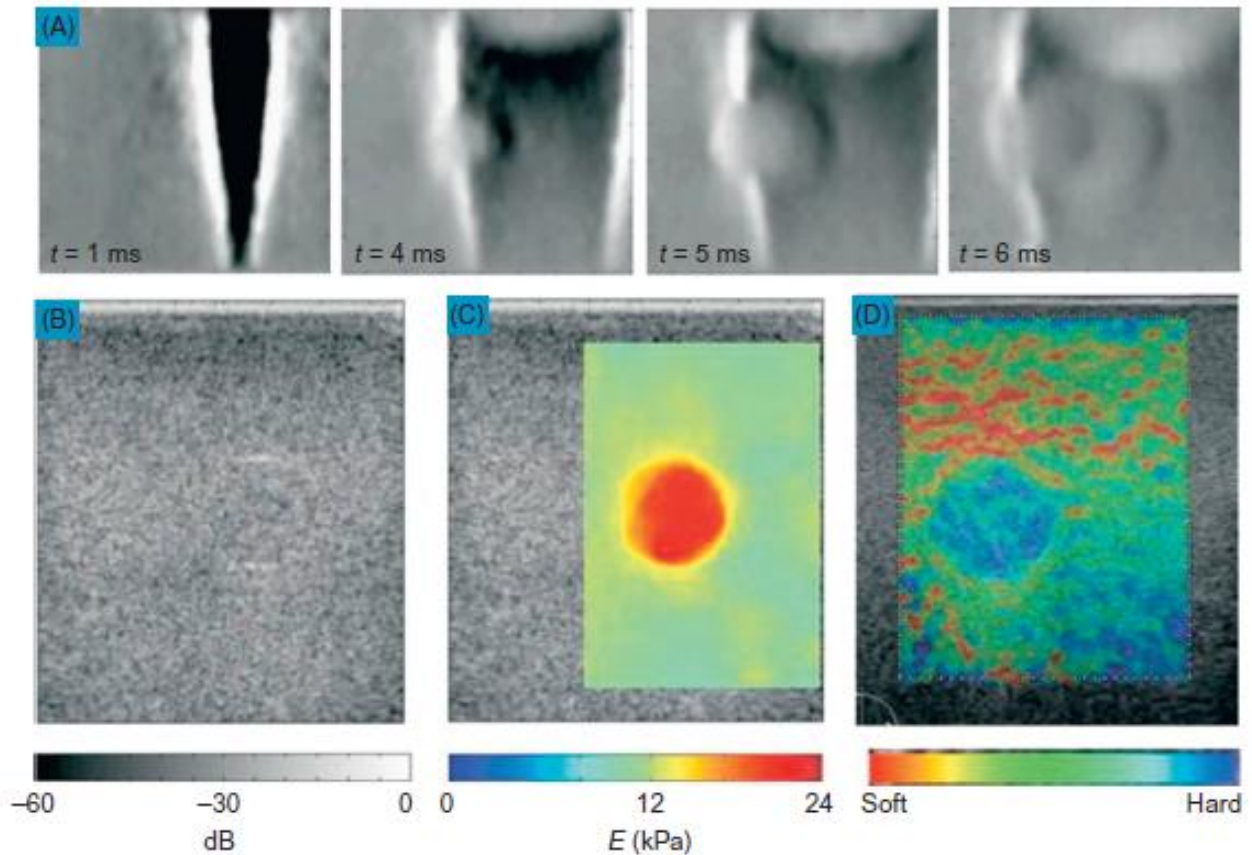
Figure 16.22. Supersonic shear wave imaging. (A) Four frames from an ultrasound movie of local displacements in a tissue-mimicking phantom at specified times after the supersonic generation of a shear wave. The gray scale indicates displacements from 210 to 110 μm. Clearly, the shear wave is sensing the stiffness contrast as it is distorted while passing through a 10-mm-diameter stiff inclusion. (B) A conventional ultrasonic image of the medium barely reveals the inclusion; (C) from the movie sampled in (A), one can obtain a quantitative image of Young's modulus, E; (D) an image of the same phantom as in (C), obtained with a commercially available ultrasound scanner using quasi-static elastography. From Fink and Tanter (2010), American Institute of Physics. *T. L. Szabo, Diagnostic Ultrasound Imaging: Inside Out, © 2014 Elsevier Inc., All rights reserved.*
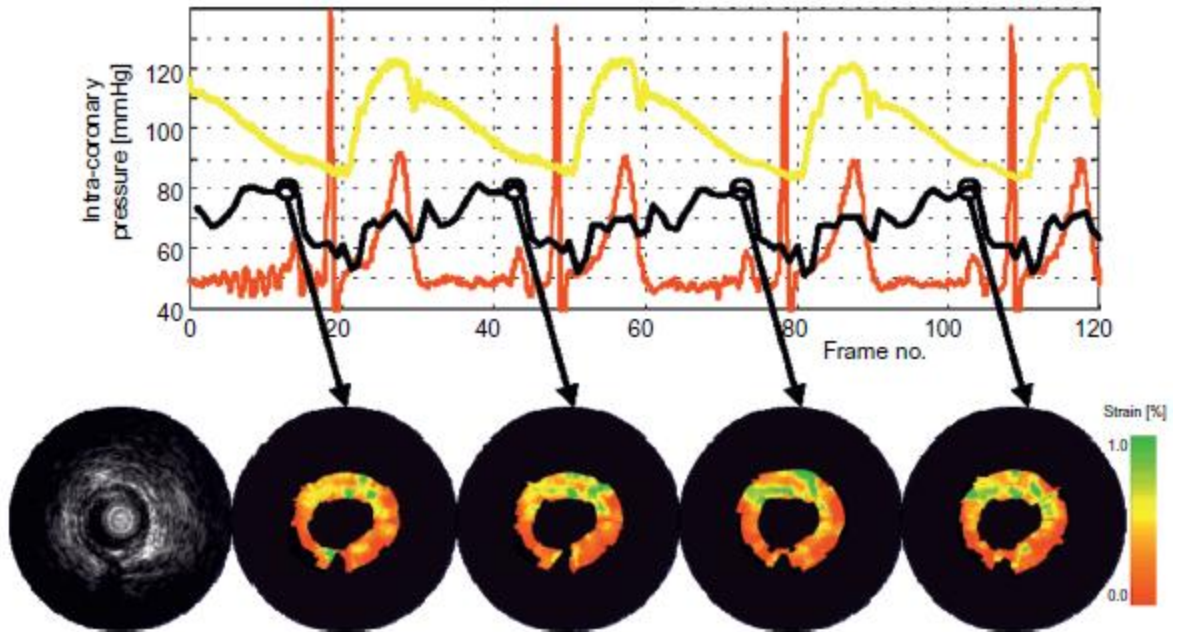
Figure 16.24. Reproducibility of IVUS elastography with elastic stimuli. The upper panel shows the physiologic signals. Echo frames acquired near end-diastole were used to determine the elastograms. The elastograms indicate that the plaque between 9 and 3 o'clock has high strain values, indicating soft material. The remaining part has low strain values, indicating hard material. At 6 o'clock, a calcified spot is visible in the echogram, corroborating the low strain values. From de Korte et al. (2000), IEEE. *T. L. Szabo, Diagnostic Ultrasound Imaging: Inside Out, © 2014 Elsevier Inc., All rights reserved.*
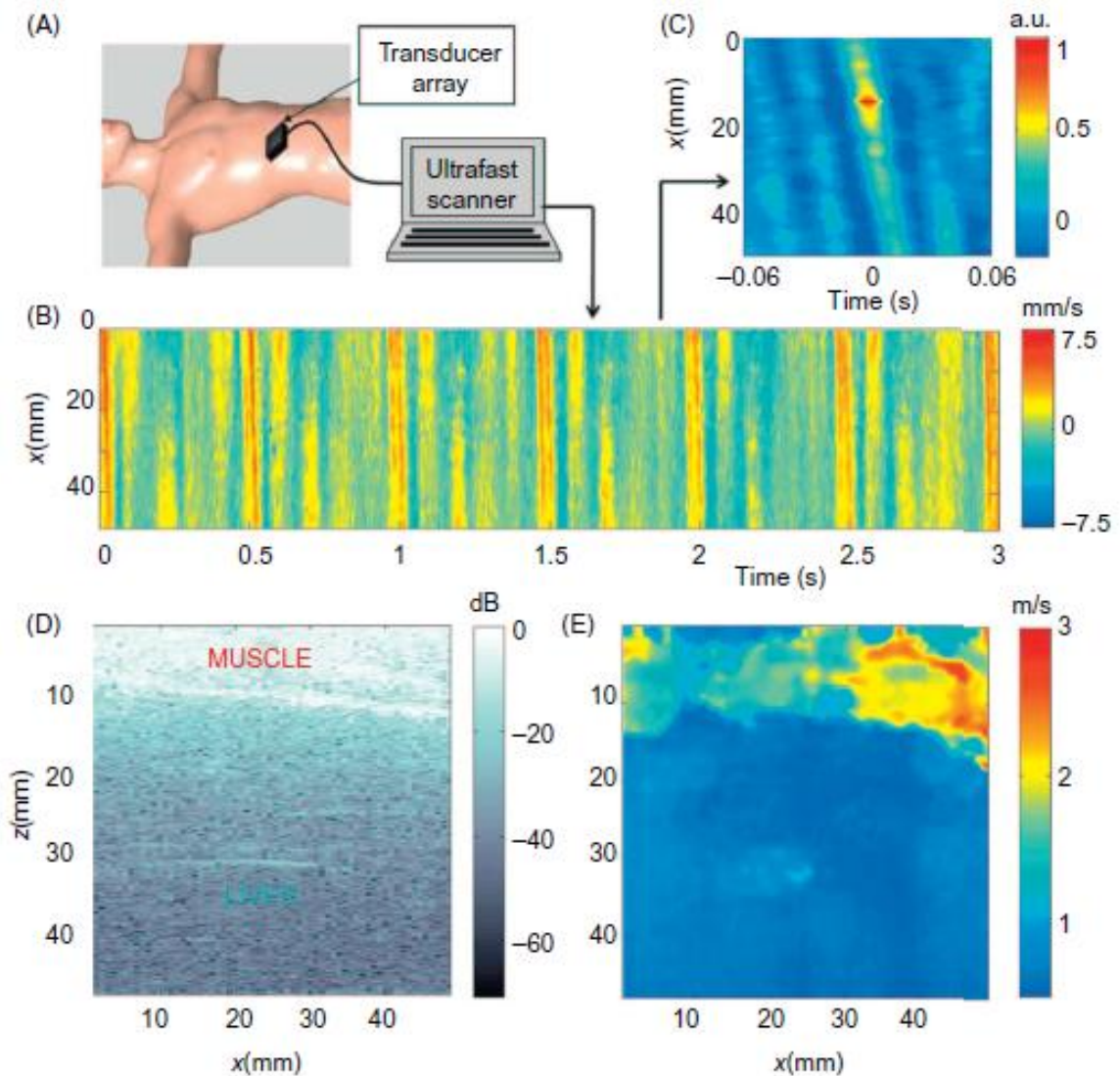
Figure 16.25. Physiological sources of movement provide sources of tissue deformation for organic elastography (A) Experimental setup for the in vivo correlation-based tomography: an ultrafast scanner was used to measure the natural displacement field in the liver region. (B) The particle velocity along an acquisition line at 4 cm, and parallel to the array, shows the physiological elastic field. (C) in the correlation map $C(x_0,x;t)$ with $x = 514$ mm, only one direction of propagation emerged from the refocusing field. (D) Sonogram of the liver region. The interface between the abdominal muscles and the liver is visible around $z = 12$ mm. (E) The passive shear-wave-speed tomography from the correlation width clearly shows the two regions. The averaged shear-speed estimations are in agreement with values in the literature. From Gallot et al. (2011), IEEE. *T. L. Szabo, Diagnostic Ultrasound Imaging: Inside Out, © 2014 Elsevier Inc., All rights reserved.*
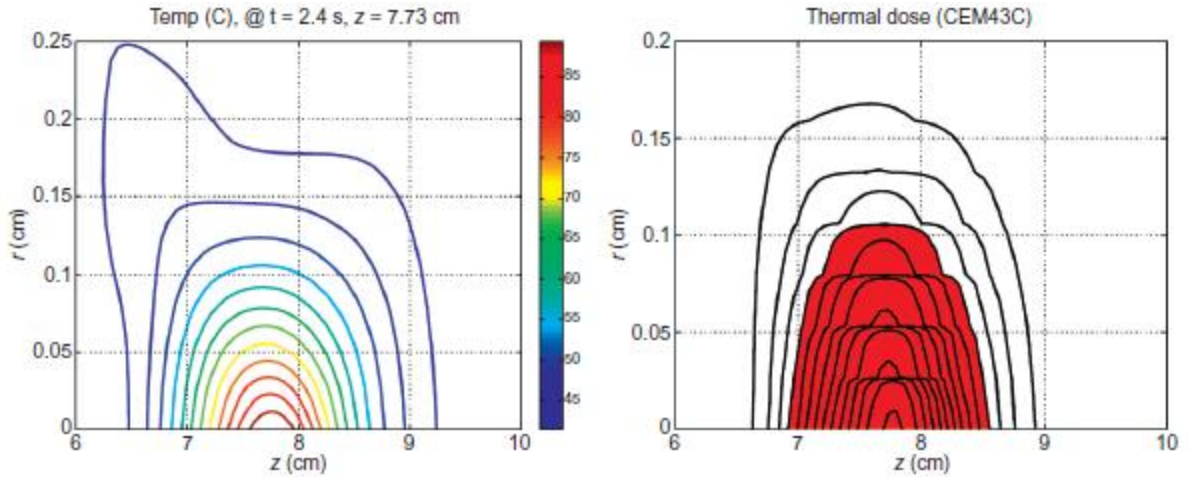
Figure 17.3. (Top) Temperature contours at the time and axial location at which the peak temperature is achieved; (Bottom) thermal dose calculation at the end of the simulation. The contours represent 0.24CEM43C, 2.4CEM43C, 24CEM43C, etc. The red (gray) area corresponds to the region in which 240CEM43C has been achieved. From Sonenson (2009), courtesy of J. Sonenson, ISTU Proceedings, AIP Publishing LLC. *T. L. Szabo, Diagnostic Ultrasound Imaging: Inside Out, © 2014 Elsevier Inc., All rights reserved.*
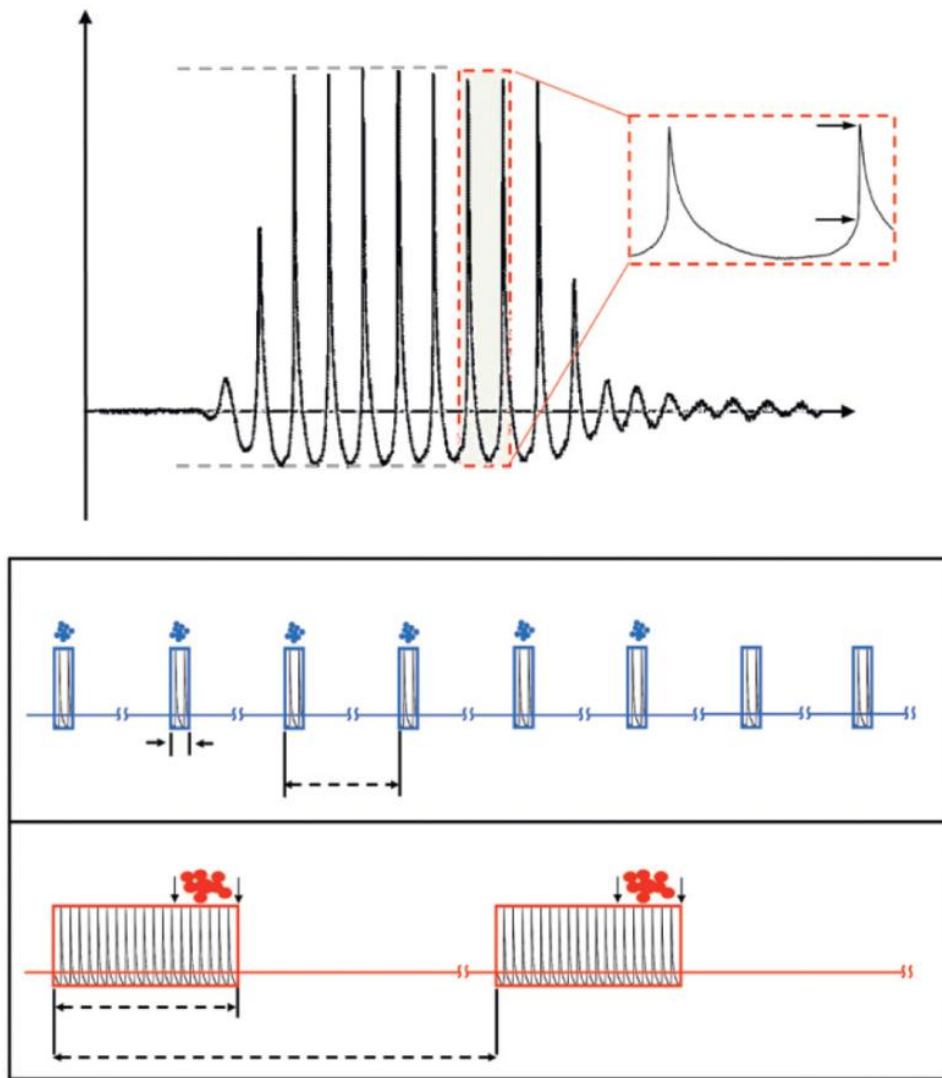
Figure 17.4. Pressure waveform and pulse-periodic timing schemes for histotripsy and boiling. (Top) Representative focal pressure waveform used for histotripsy. The pulse is initially a sinusoidal tone burst, but at the focus it is distorted by the combined nonlinear propagation and diffraction effects to produce the asymmetric waveform with higher peak positive pressure (p1), lower-amplitude peak negative pressure (p2), and high-amplitude shocks formed between negative and following positive phase as shown in the inset frame. (Bottom) Pulse-periodic timing schemes for two forms of histotripsy. The blue (upper) sequence shows the cavitation-cloud histotripsy scheme with microsecond-long pulses applied at 1001000 Hz. The red (lower) sequence shows the boiling histotripsy scheme, employing millisecond long pulses at a rate of 0.51 Hz. From Maxwell et al. (2012), Acoustical Society of America. *T. L. Szabo, Diagnostic Ultrasound Imaging: Inside Out, © 2014 Elsevier Inc., All rights reserved.*
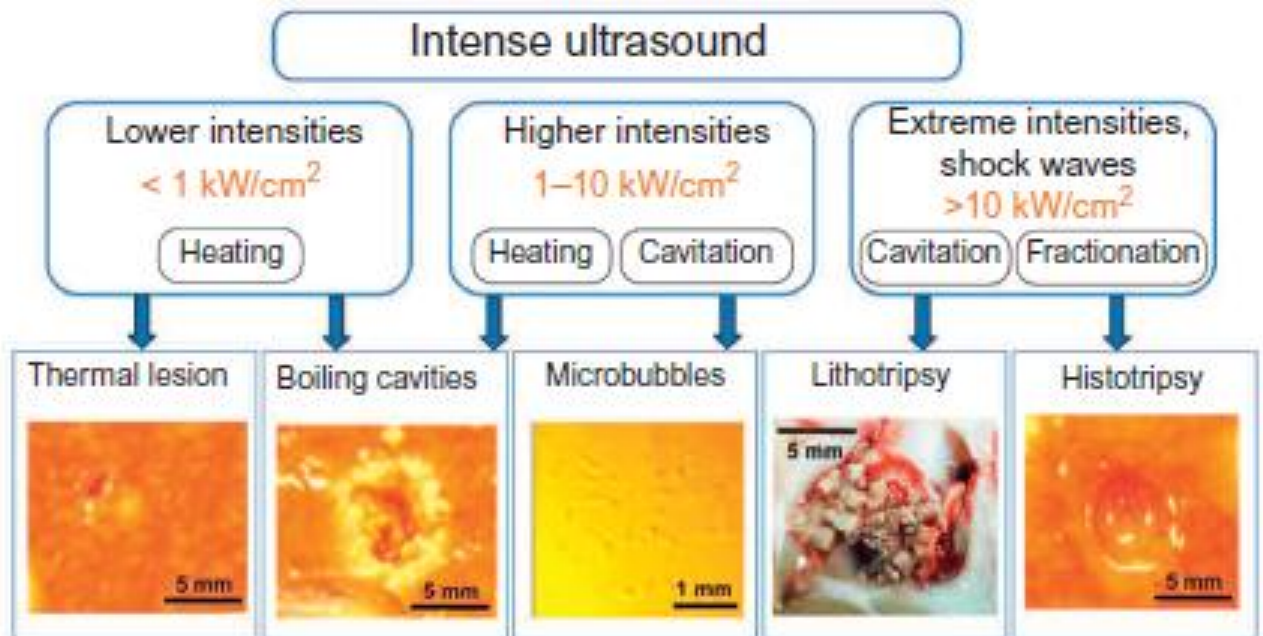
Figure 17.7. Bioeffects of focused ultrasound at different focal intensity levels. At lower intensities, heating through acoustic absorption is the dominant mechanism, denaturing proteins within the tissue, leaving a blanched appearance. Boiling cavities form in the lesion when the temperature reaches 100C. At higher intensities, heating combined with microbubble cavitation can cause mechanical trauma to the tissue structure. At very high intensities, shockwaves form at the focus and the wave itself can impart significant mechanical damage, such as comminution of kidney stones (lithotripsy) or fractionation of soft tissues (histotripsy). From Maxwell et al. (2012), Acoustical Society of America. *T. L. Szabo, Diagnostic Ultrasound Imaging: Inside Out, © 2014 Elsevier Inc., All rights reserved.*
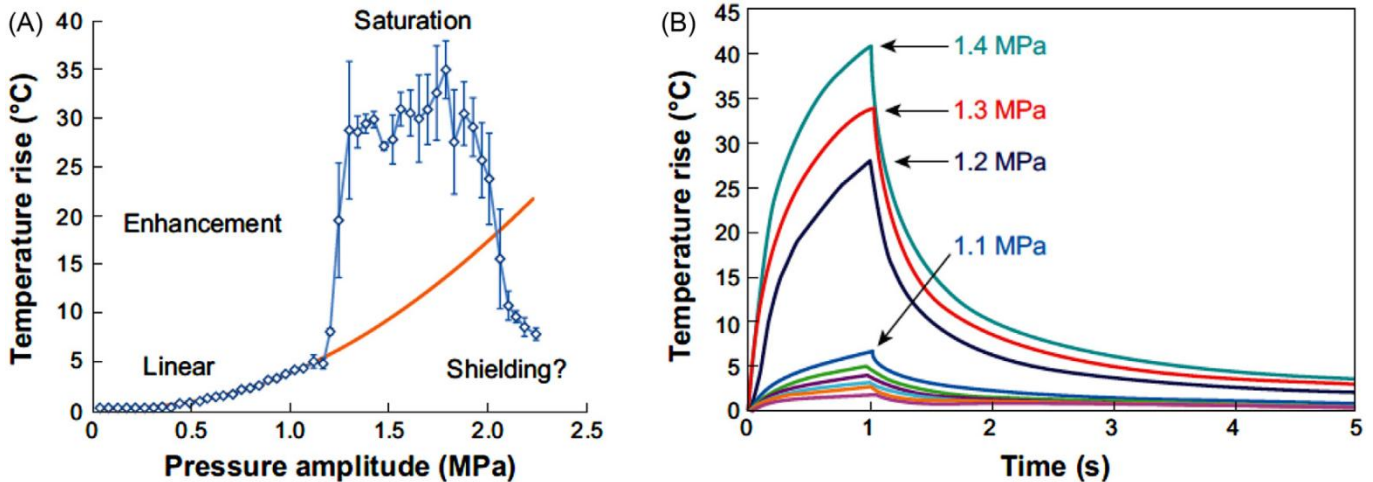
Figure 17.8. Temperature rise measured by a thermocouple embedded in an Agar-graphite tissue-mimicking material exposed to 1-MHz HIFU for 1s. The data have been smoothed to minimize noise, and a correction factor was applied that accounts for the so-called thermocouple artifact, which refers to enhanced heating in the viscous boundary layer surrounding the thermocouple. (A) Measured (blue/circles with error bars) and predicted (orange/line) peak temperature rise versus the acoustic peak-rarefaction pressure amplitude. The error bars depict the standard deviation of five measurements. (B) Measured temperature versus time for increasing peak-rarefaction pressure amplitudes; each curve corresponds to an increment of approximately 0.1 MPa. Figure adapted from Coussios et al. (2007) and Coussios and Roy (2010), Annual Review of Fluid Mechanics. *T. L. Szabo, Diagnostic Ultrasound Imaging: Inside Out, © 2014 Elsevier Inc., All rights reserved.*
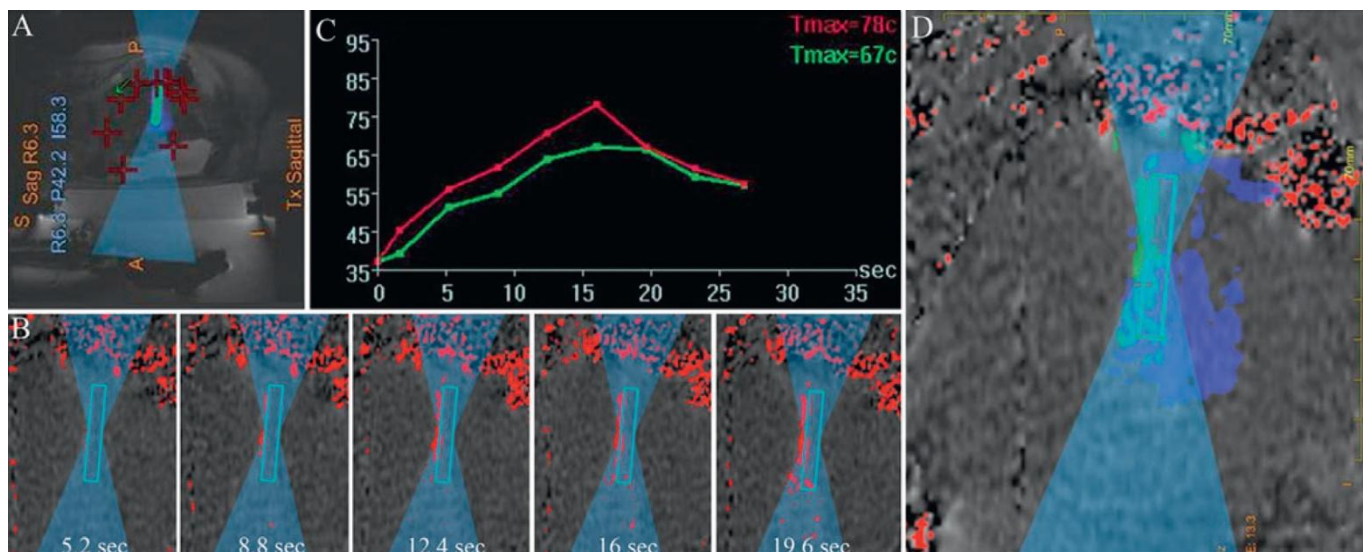
Figure 17.11. MRgFUS enables closed-loop treatment monitoring of each sonication. (A) Ablation is planned by using anatomic T2-weighted images acquired at the beginning of the treatment. Blue (pale gray in print version) overlay depicts outline of the projected FUS beam path. Beam focus is delineated by the rectangle. (B) During sonications, thermal images are acquired and displayed every 3.6s during the 20-s sonication. (C) Graphs indicating temperature history of the hottest voxel (red/dark gray) and average of nine voxels (green/light gray) are automatically displayed during sonication. (D) At the end of each sonication, dosimetry is performed and predicted tissue ablation is displayed (green) superimposed with anatomy (blue overlay represents tissue ablated in the previous sonications). Thermal feedback allows for in-treatment adjustment of sonication parameters. From Helsey (2013), Cardiovascular Interventional Radiology. *T. L. Szabo, Diagnostic Ultrasound Imaging: Inside Out, © 2014 Elsevier Inc., All rights reserved.*
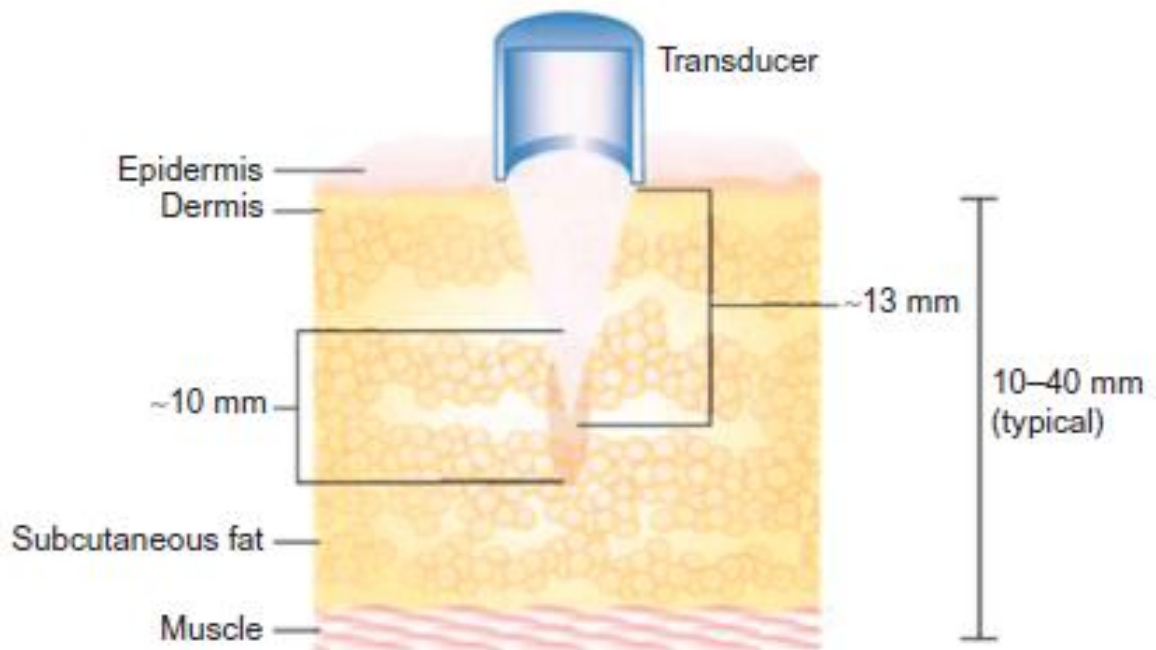
Figure 17.12. HIFU beam passing through the skin and superficial tissues without causing injury. The temperature at the focal point causes rapid cell death, but tissues immediately above and below the focal point are unharmed. From Jewell et al. (2011), Aesthetic Plastic Surgery. *T. L. Szabo, Diagnostic Ultrasound Imaging: Inside Out, © 2014 Elsevier Inc., All rights reserved.*
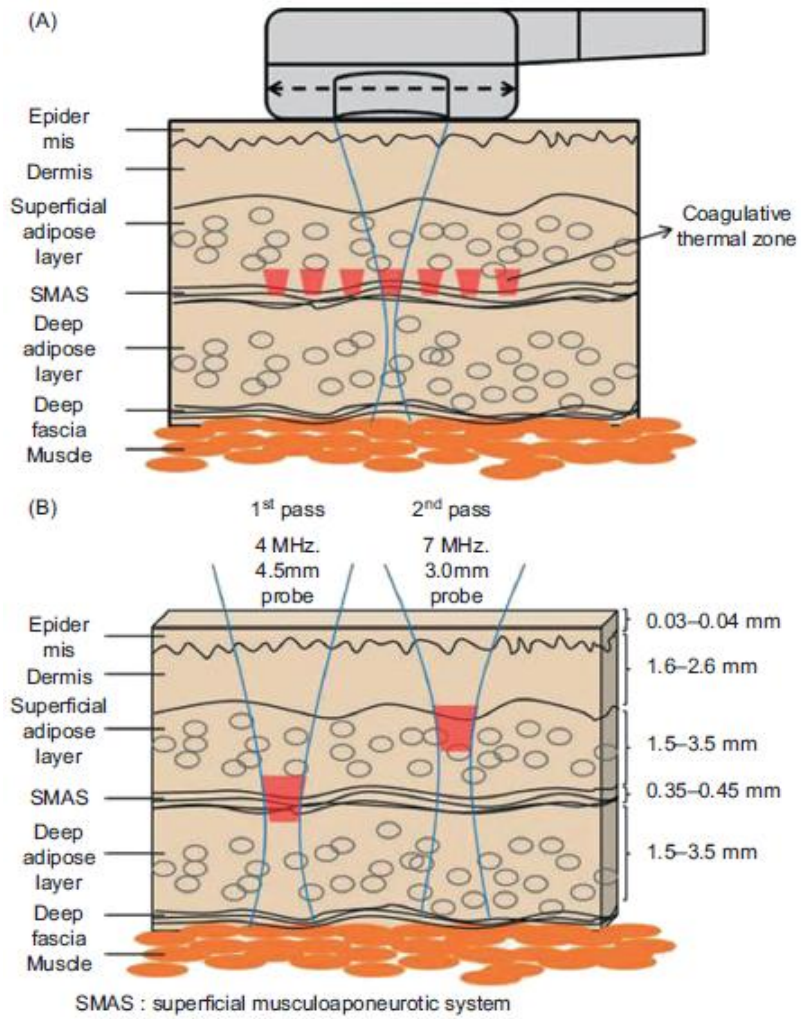
Figure 17.13. Schematic view of the ultrasound device being applied to the skin. (A) The probe emanates a series of wedge-shaped focused ultrasound beams along a 25-mm-long exposure line and makes thermal coagulative zones. (B) The thermal coagulation zone of the first pass (using the 4-MHz, 4.5-mm probe) extends from the superficial adipose layer through the SMAS to the deep adipose layer. The thermal coagulation zone of the second pass (using the 7-MHz, 3.0-mm probe) extends from the deep dermis to the superficial adipose layer. From Lee et al. (2011), Dermatologic Surgery. *T. L. Szabo, Diagnostic Ultrasound Imaging: Inside Out, © 2014 Elsevier Inc., All rights reserved.*

2.3 J **3.0 J** **3.8 J** **4.6 J** **6.1 J** **7.6 J**
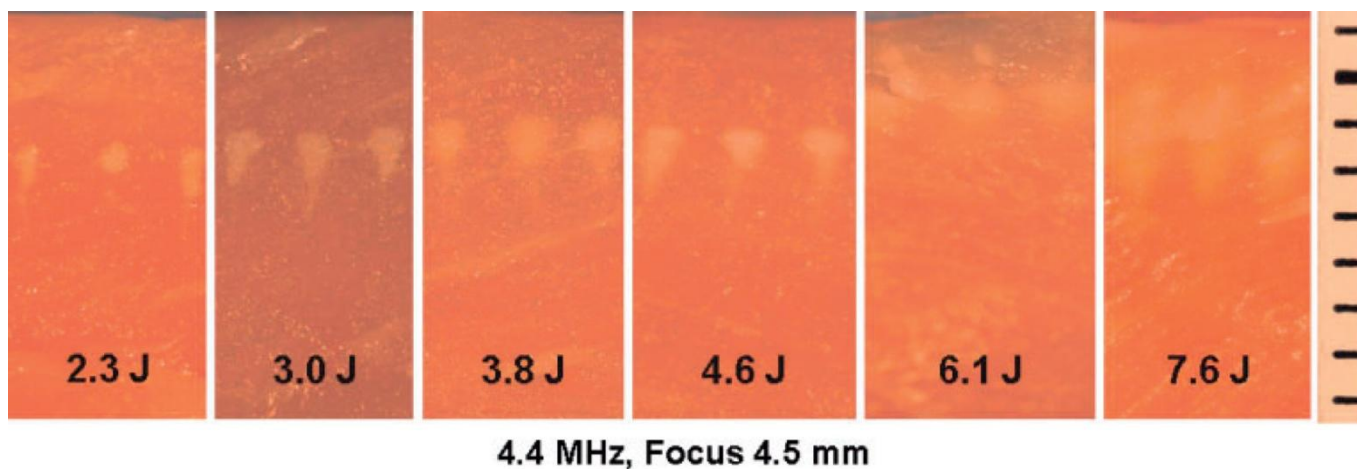
4.4 MHz, Focus 4.5 mm

Figure 17.14. Thermal Injury Zones (TIZs) as a Function of Dose in Muscle. Digital photographs of gross tissue sections (approximately 1 mm thick) of porcine muscle reveal profile of changes in geometry of TIZ as the source energy is increased from 2.3 to 7.6 J. Within the homogenous orange-colored muscle tissue, the white inverse-pyramidal regions of coagulated tissue are the TIZs resulting from the ultrasound exposure (4.4 MHz, 4.5-mm-focus handpiece). From White et al. (2008), Lasers in Surgery and Medicine. *T. L. Szabo, Diagnostic Ultrasound Imaging: Inside Out, © 2014 Elsevier Inc., All rights reserved.*
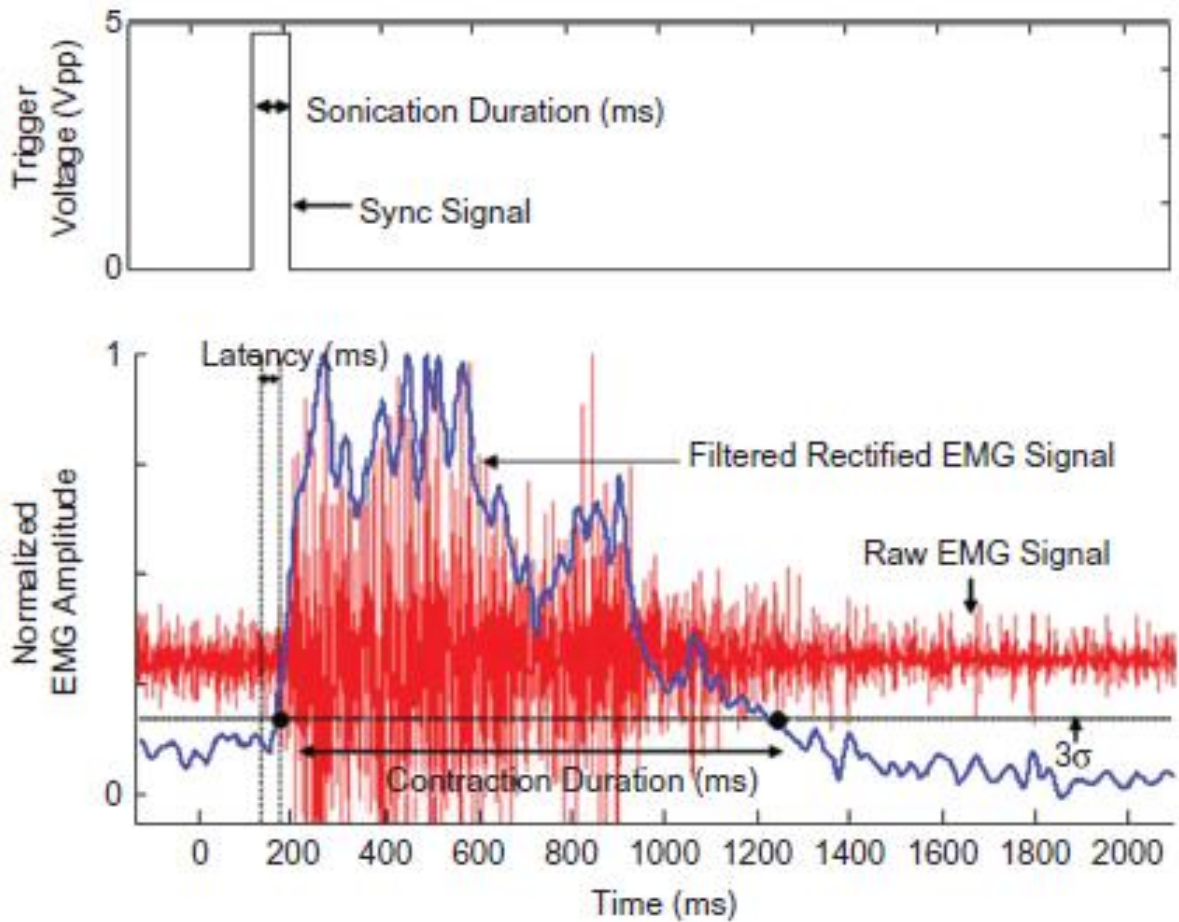
Figure 17.16. Transcranial ultrasound stimulation of mouse brain. (A) An example sync pulse, 80 ms in duration, that governed the duration of the sonication. (B) The red trace, resulting from a 16.8-W/cm2 sonication, is a sample EMG signal following amplification (gain 10,003, high-pass filter 300 Hz, low-pass filter 1 kHz). The blue trace is the rectified, smoothed EMG signal. A muscle contraction was defined as beginning when the filtered signal rose above the third standard deviation of the noise level, represented in the figure by the horizontal dashed line, for at least 100 ms. The time from the beginning of the ultrasound pulse to the beginning of the contraction was defined as the latency. King et al.(2013), with permission from the World Federation of Ultrasound in Medicine and Biology. *T. L. Szabo, Diagnostic Ultrasound Imaging: Inside Out, © 2014 Elsevier Inc., All rights reserved.*